UNIVERSIDADE FEDERAL DE SANTA CATARINA
CENTRO TECNOLÓGICO DE JOINVILLE
PROGRAMA DE PÓS-GRADUAÇÃO EM ENGENHARIA E CIÊNCIAS MECÂNICAS

Damylle Cristina Xavier Donati

Experimental and Numerical Study of the Modeling of the Fluid-Structure Phenomenon in Plate Heat Exchangers

Joinville - SC
2023

Damylle Cristina Xavier Donati

Experimental and Numerical Study of the Modeling of the Fluid-Structure Phenomenon in Plate Heat Exchangers

Dissertação submetida ao Programa de Pós-Graduação em Engenharia e Ciências Mecânicas da Universidade Federal de Santa Catarina como requisito parcial para a obtenção do título de Mestra em Fenômenos de Transporte.

Orientador(a): Profa, Dra. Talita Sauter Possamai.

Joinville - SC
2023

Donati, Damylle Cristina Xavier
Experimental and Numerical Study of the Modeling of the Fluid-Structure Phenomenon in Plate Heat Exchangers / Damylle Cristina Xavier Donati ; orientadora, Talita Sauter Possamai, 2023.
162 p.

Dissertação (mestrado) - Universidade Federal de Santa Catarina, Campus Joinville, Programa de Pós-Graduação em Engenharia e Ciências Mecânicas, Joinville, 2023.

Inclui referências.

1. Engenharia e Ciências Mecânicas. 2. Fluid-Structural Interaction (FSI). 3. Computational Fluid Dynamics (CFD). 4. Finite Element Analysis (FEA). 5. Gasketed Plates Heat Exchanger (GPHE). I. Possamai, Talita Sauter. II. Universidade Federal de Santa Catarina. Programa de Pós-Graduação em Engenharia e Ciências Mecânicas. III. Título.

Damylle Cristina Xavier Donati

Experimental and Numerical Study of the Modeling of the Fluid-Structure Phenomenon in Plate Heat Exchangers

O presente trabalho em nível de Mestrado foi avaliado e aprovado, em 29 de setembro de 2023, pela banca examinadora composta pelos seguintes membros:

Prof. Kleber Vieira de Paiva, Dr.
Universidade Federal de Santa Catarina (UFSC)

Prof. André Luís Condino Fujarra, Dr.
Universidade Federal de Santa Catarina (UFSC)

Prof. Roberto Wolf Francisco Júnior, Dr
Universidade do Estado de Santa Catarina (UDESC)

Certificamos que esta é a versão original e final do trabalho de conclusão que foi julgado adequado para obtenção do título de Mestra em Engenharia e Ciências Mecânicas

ICP-Edu
Documento assinado digitalmente
Wagner Mauricio Pachekoski
Data: 20/11/2023 15:15:32-0300
CPF: ***.494.569-**
Verifique as assinaturas em https://v.ufsc.br

Coordenação do Programa de Pós-Graduação

ICP-Edu
Documento assinado digitalmente
Talita Sauter Possamai
Data: 20/11/2023 14:20:25-0300
CPF: ***.039.319-**
Verifique as assinaturas em https://v.ufsc.br

Profa. Talita Sauter Possamai, Dra.
Orientadora

Joinville, 2023.

AGRADECIMENTOS

Agradeço primeiramente a meus pais, Nilfa e Osmar, pelo dom da vida e por estabelecer o padrão de ser humano que sigo até hoje. Sem a influência e o zelo de vocês não teria chego até onde cheguei sem ser quem eu sou. Agradeço à minha irmã, Danyelle, por ter sido minha base e inspiração, por ter ajudado em minha criação e por nunca ter deixado de me permitir ser vulnerável ao seu redor. Antes de qualquer título, sou filha e irmã mais nova.

Agradeço à minha metade, Rodrigo, por ter aparecido no momento certo e ter se tornado tudo que há de certeza no meu caminho. Não apenas por ter estado do meu lado quando precisei, mas também por ter aprendido junto a mim nessa aventura. Obrigada por ser meu parceiro, antes de qualquer coisa.

Agradeço aos amigos que colecionei durante este caminho tortuoso. Thais, Arethusa, Vanessa, Arthur, Bárbara, Ygor, Emmanuel, Flávia, Paola, Joyce, Vanessa, Caroline, Martin, Bianca, Igor e Jéssica. Vocês viram a criação, a ferro e fogo, da profissional e da pessoa que sou, uma liga que não se separa. Agradeço aos amigos que ainda serão parte do novo capítulo, Bruna, Rodrigo Cardozo, Ludmila, Lucas, Carlos, Vitória, Sara e Guilherme. Vocês são coautores da minha jornada e terão meu apoio sempre que precisarem nas suas.

Agradeço à professora Talita Possamai, por ter não apenas me orientado, mas me tutelado na busca de ser pesquisadora. Atribuo a essa parceria de uma década muitas de minhas conquistas e espero poder transmitir o possível para as novas gerações.

Aos professores Renato Oba, Kleber Paiva e Jorge Oliveira, por terem aberto as portas no grupo de pesquisa para mim e me auxiliado na escada desde a graduação, até aqui e além. Aos professores Antônio Dourado e Rafael Cuenca, por me ajudarem em todas as trilhas paralelas em que nos cruzamos. Ao Eng. Giovani Martins, por ter me auxiliado na aquisição e tratamento de dados para este trabalho. Ainda, agradeço à UFSC, à FEESC, à Petrobras e à ANP pelos recursos necessários para o desenvolvimento deste estudo.

I tripped the moment I was born
I've been running ever since.

RESUMO

Trocadores de calor de placas gaxetadas (GPHEs) são dispositivos versáteis amplamente utilizados em diversas aplicações devido ao seu design compacto, facilidade de manutenção e capacidade de comportar múltiplos fluidos de trabalho. As gaxetas são componentes críticos para GPHEs, pois previnem vazamento e separam os escoamentos dos ramais. Para garantir seu funcionamento, é essencial estudar comportamentos que afetam sua performance e sua vedação. Um fenômeno significativo é a deformação elástica das placas corrugadas, causada pela interação fluido-estrutural (FSI). Este trabalho estuda a separação das placas causada pela deformação elástica, focando em duas abordagens numéricas distintas: a análise hidrostática (com análises numéricas estrutural e hidrodinâmica independentes) e a análise de interação fluido-estrutural em via única (FSI one-way). O modelo investiga um pack de placas reduzidos, com 4 placas corrugadas de ângulo de chevron de 60º, feitas em aço 316L e com as gaxetas modeladas como suporte elástico, sendo validado com valores de pressão de fluido e deslocamento lateral das placas adquiridos experimentalmente. Tais metodologias são validadas por meio de comparação com resultados experimentais adquiridos em duas bancadas distintas cuja montagem e funcionamento são discutidos, bem como os dados de pressão e deslocamento levantados. Os resultados da análise experimental hidrodinâmica mostraram que há maior influência da deformação das placas no ramal externo do que no interno, pela sua proximidade aos tampos. Os resultados da análise CFD ajudaram a entender o comportamento hidrodinâmico do trocador de calor. Os campos de pressão e velocidade mostraram um perfil linear ao longo do comprimento dos ramais, em concordância com a literatura. O campo de velocidades identificou aceleração na galeria de entrada, zonas de estagnação e recirculação nos pontos de contato do canal de troca térmica, além de alta vorticidade na saída. Seções transversais revelaram a influência da geometria na deformação do perfil de velocidades. Comparados aos dados experimentais, os resultados de CFD para a geometria original tiveram boa concordância na curva de queda de pressão. A análise estrutural hidrostática destacou a influência crítica das galerias de distribuição e do canal da gaxeta. A montagem do GPHE também afetou o estado de tensão, com diferenças notáveis nas deformações direcionais. O perfil de afastamento da placa indicou comportamento de torção. A análise FSI mostrou novos modos de torção da placa devido à queda de pressão. As zonas de tensão crítica permaneceram as mesmas, com aumento da magnitude. Em relação ao desempenho das metodologias numéricas, a hidrostática ofereceu uma estimativa geral de comportamento com baixo custo, enquanto a FSI foi mais custosa, mas menos dependente de intervenção do usuário.

Palavras-chave: GPHE; FSI; CFD; FEM; Deformação Elástica.

RESUMO EXPANDIDO

Introdução

Trocadores de calor de placas gaxetadas (GPHE) são dispositivos térmicos utilizados em diversas aplicações por sua versatilidade em utilizar mais de um fluido de trabalho, ser classificado como compacto e facilmente ser acessado para manutenção ou modificação de geometria da área de troca térmica, por meio da escolha de acoplamentos de placas corrugadas distintas. Um dos fenômenos presentes neste tipo de dispositivo que podem levar à sua falha é a deformação elástica das placas corrugadas causada pela interação fluido-estrutural nas interfaces placa-fluido, que tem como entrada os estados de pressão e temperatura do escoamento de cada um dos ramais e saída os estados de tensão e deformação das placas. Tal deformação é composta por três direções distintas, chamadas separação, alargamento e alongamento.

A literatura indica que as tensões mais elevadas neste tipo de dispositivo são provenientes de carregamentos mecânicos, baseando a escolha do presente trabalho em isolar este tipo de carregamento na análise. A separação é a deformação direcional mais proeminente e, portanto, objeto de estudo deste trabalho. Diversas abordagens podem ser utilizadas para estudar e avaliar tais fenômenos, como análises experimentais em bancada e análises numéricas. O presente estudo apresente três abordagens, uma experimental e duas numéricas, para análise do problema.

Objetivos

Este estudo tem como objetivo avaliar metodologias de análise hidrostática e interação fluido-estrutural (FSI) de via única em relação ao acoplamento de escoamento e estrutura com feedback em um trocador GPHE simplificado. Como objetivos específicos, destacam-se o estudo do comportamento fluido-estrutural em trocadores de calor do tipo GPHE, a definição de uma metodologia com feedback para análise hidrostática utilizando variação de espaçamento uniforme, o entendimento das limitações e necessidades para a aplicação de metodologia de FSI de via única, a validação dos resultados hidrodinâmicos e estruturais com dados experimentais e a comparação das metodologias numéricas propostas com uso de métricas de desempenho.

Metodologia

O estudo apresenta a metodologia hidrostática, que faz uso de análises pelo método de elementos finitos (FEM) e por dinâmica de fluidos computacional (CFD) de forma desacoplada, para inferir valores máximos de pressão de fluido e deslocamento normal da placa, definindo casos críticos para modelar o fenômeno. Em segundo momento, o estudo apresenta a metodologia de interação fluido-estrutural em one-way (FSI One-Way), que aplica fielmente o campo de pressões no sólido e leva em consideração não apenas os valores máximos, mas também o perfil de queda de pressão na placa, agregando todos os modos de deformação existentes. O modelo investiga um pack de placas reduzidos, com 4 placas corrugadas de ângulo de chevron de 60º, feitas em aço 316L e com as gaxetas modeladas como suporte elástico, sendo validado com valores de pressão de fluido e deslocamento lateral das placas adquiridos experimentalmente. Tais metodologias são validadas por meio de comparação com resultados experimentais adquiridos em duas bancadas distintas cuja montagem e funcionamento são discutidos, bem como os dados de pressão e deslocamento levantados.

Resultados e Discussão

Os resultados da análise CFD auxiliaram no entendimento do comportamento hidrodinâmico do trocador de calor. Campos de pressão e velocidade foram adquiridos nos planos centrais dos passes de cada ramal e verificou-se um perfil de pressão linear ao longo do comprimento do ramal, concordando com resultados encontrados na literatura. Aceleração de fluido na galeria de distribuição de entrada, zonas de estagnação e recirculação nos pontos de contato do canal de troca térmica e alta vorticidade no bocal de saída são os principais comportamentos identificados pelo campo de velocidades no mesmo plano central.

Em relação a seções transversais tomadas em pontos de mudança brusca na geometria do volume fluido, o campo de velocidades concorda com a construção geométrica do ramal, deformando seu perfil na direção da entrada de fluido e apresentando recirculação no centro do canal por conta dos pontos de contato. Perfis tomados verticalmente ao longo da linha que conecta os bocais de entrada e saída corroboram o perfil linear de pressão, bem como o papel de aceleração de escoamento das galerias de distribuição de entrada e saída. Quando comparados com os dados experimentais, os resultados de CFD para a geometria original, sem deformação imposta no volume, mostraram boa concordância na curva de queda de pressão em relação à vazão de entrada para casos em que a diferença de pressão de entrada entre ramais é nula. Isso se dá pois a análise CFD individualmente não é capaz de contabilizar a influência da deformação elástica das placas corrugadas na geometria do volume fluido e, por consequência, a mudança das estruturas de escoamento decorrentes disso.

Da análise estrutural hidrostática, o estado de tensão e deformação das placas se mostraram altamente dependentes do carregamento interno do pack, acentuando como crítica as galerias de distribuição de fluido e o canal da gaxeta que as rodeiam, devido ao fato da zona dos ports de entrada e saída não se encontrarem na região em que há simetria de carga, caracterizando canais não-suportados de gaxeta. Os resultados também mostraram que a etapa de montagem do GPHE tem grande influência no estado de tensão do mesmo, as deformações direcionais de alargamento e alongamento são consideravelmente menos influentes na deformação total das placas do que o afastamento das mesmas, com diferenças de até 10 vezes entre os valores. Os perfis de afastamento da placa se mostraram não uniformes, principalmente para carregamentos assimétricos, e indicaram comportamento de torção das placas. Consideráveis zonas de plastificação foram encontradas na placa, correspondentes às zonas de tensão crítica.

Os valores máximos de deslocamento para os carregamentos simétricos foram usados como base para a geração de novos volumes fluidos, que adoram como altura de corrugação a altura original mais o valor máximo de afastamento das placas, para cada caso. Com as novas análises CFD percebeu-se considerável atenuamento das magnitudes de pressão e a construção de um caminho preferencial de fluido à medida que o afastamento subia. Os perfis de velocidade e pressão não se modificaram globalmente, apenas suas magnitudes. Da análise FSI, foi possível notar a influência da queda de pressão nos perfis de deformação da placa, indicando novos modos de torção da mesma. Ainda, os resultados hidrostáticos se mostraram relativamente menores do que os obtidos por FSI, indicando que a aplicação da primeira metodologia deve ser dirigida com cautela. As

zonas de tensão crítica se mantiveram as mesmas. Em relação ao desempenho das metodologias numéricas, foi possível perceber que a metodologia hidrostática se mostrou uma boa alternativa para a obtenção de estimativas e de entendimento geral do comportamento de GPHEs, com relativa fidelidade e baixo custo computacional, mas com relevante intervenção de usuário. Já a metodologia FSI se mostrou mais custosa, com aproximadamente 110 horas de simulação, porém menos dependente de intervenção de usuário.

Conclusão

Os resultados da análise experimental hidrodinâmica mostraram que há maior influência da deformação das placas no ramal externo do que no interno, pela sua proximidade aos tampos. Os resultados das análises CFD sem deformação do domínio fluido podem ser utilizadas para modelar carregamentos simétricos, tanto em contracorrente como em paralelo, enquanto o espaçamento uniforme das placas mostra boa concordância com valores de diferença de pressão de entrada entre ramais maiores e constantes, mas não com maiores variações. Para modelar as curvas de fator de atrito foram necessárias três correlações distintas, consequência da quantidade de modelagens e simplificações impostas pelo método numérico e seu impacto em cada ramal. Os valores de separação e tensão equivalente de von Mises indicam alta ocorrência de zonas de concentração de tensão, principalmente na galeria de distribuição de fluido e no canal da gaxeta que a envolve. A metodologia hidrostática mostrou menor custo computacional com resultados mais subdimensionados em relação à metodologia FSI.

Palavras-chave: GPHE; FSI; CFD; FEM; Deformação Elástica.

ABSTRACT

Gasketed plate heat exchangers (GPHEs) are versatile devices widely used in various applications due to their compact design, ease of maintenance, and ability to accommodate multiple working fluids. Gaskets are critical components for GPHEs because they prevent leaks and separate banch flows. To ensure their function, it is essential to study the behaviors that affect their performance and sealing. An important phenomenon is the elastic deformation of corrugated plates caused by fluid-structure interaction (FSI). This work studies the separation of plates caused by elastic deformation, focusing on two different numerical approaches: hydrostatic analysis (with independent structural and hydrodynamic numerical analyses) and one-way fluid-structural interaction analysis (one-way FSI). The model investigates a reduced plate pack with 4 corrugated plates with 60º chevron angle, made of 316L steel and with gaskets modeled as elastic support, which is validated with values of fluid pressure and lateral displacement of the plates obtained experimentally. Such methodologies are validated by comparison with experimental results obtained on two different benches, whose assembly and operation are discussed, as well as the pressure and displacement data collected. The results of the hydrodynamic experimental analysis showed that there is a greater influence of the deformation of the plates in the external branch than in the internal one, due to its proximity to the cover plates. The results of the CFD analysis helped to understand the hydrodynamic behavior of the heat exchanger. The pressure and velocity fields showed a linear profile along the length of the branches, in agreement with the literature. The velocity field identified acceleration in the inlet gallery, stagnation and recirculation zones at the contact points of the heat exchanger channel, in addition to high vorticity at the outlet. Cross-sections revealed the influence of geometry on the deformation of the velocity profile. Compared to the experimental data, the CFD results for the original geometry showed good agreement on the pressure drop curve. The hydrostatic structural analysis highlighted the critical influence of the distribution galleries and the gasket channel. The assembly of the GPHE also affected the stress state, and the most influential directional deformation mode was found to be separation, with displacements up to 10 times larger than the others. The plate separation profile indicated torsional behavior. FSI analysis showed new modes of plate twisting due to pressure drop. The critical stress zones remained the same, with increased magnitude. Regarding the performance of the numerical methods, hydrostatic analysis provided a general estimate of the behavior at low computational cost, while FSI was more expensive but less dependent on user intervention.

Keywords: GPHE; FSI; CFD; FEM; Elastic Deformation.

LIST OF FIGURES

LIST OF TABLES

LIST OF ABBREVIATIONS AND ACRONYMS

AR - Aspect Ratio
ASME - American Society of Mechanical Engineers
ASTM - American Society for Testing and Materials
BPHE - Brazed-Plate Heat Exchanger
CFD - Computational Fluid Dynamics
CST - Constant Strain Triangle
DNS - Direct Numerical Simulation
DOF - Degrees of Freedom
FEA - Finite Element Analysis
FEM - Finite Element Method
FSI - Fluid-Structural Interaction
FVM - Finite Volume Method
GPHE - Gasketed-Plates Heat Exchanger
HNBR - Hydrogenated Nitrile Rubber
LES - Large Eddy Simulation
LVDT - Linear Variable Differential Transformer
MOGA - Multi-Objective Genetic Algorithm
NACA - National Advisory Committee for Aeronautics
PHE - Plate Heat Exchanger
PFHE - Plate-Fin Heat Exchanger
PSHE - Plate-and-Shell Heat Exchanger
Q4 - Quadrilateral Bilinear Element
Q8 - Quadratic Quadrilateral Element
RAM - Random-Access Memory
RANS - Reynolds-Averaged Navier-Stokes
SHE - Shell-and-Tube Heat Exchanger
SST - Shear Stress Transport
T2F - Thermal Fluid Flow Group
UFSC - Federal University of Santa Catarina
VOF - Volume Fraction of Fluid

LIST OF SYMBOLS

β	Chevron angle	[º]
L	Length of the plate	[mm]
W	Width of the plate	[mm]
b	Corrugation height	[mm]
t	Plate thickness	[mm]
P_c	Period of corrugation	[mm]
d_P	Port diameter	[mm]
P_{fluid}	Fluid pressure	[Pa]
σ_{solid}	Stress in the plate	[Pa]
Δx	Variation in the dimension of the x-axis	[mm]
Δy	Variation in the dimension of the y-axis	[mm]
Δz	Variation in the dimension of the z-axis	[mm]
ΔP	Pressure drop	[Pa]
Re	Reynolds number	[-]
f	Friction factor	[-]
τ_s	Shear Stress	[Pa]
Re_{in}	Reynolds number in the inlet of the branch	[-]
G	Massic velocity	[kg*m/s]
$\dot{m}_{in}$	Massic inlet flow	[kg/s]
A_0	Total free-flow area of the branch	[m²]
D_h	Hydraulic diameter of the corrugation	[mm]
D_e	Effective diameter of the corrugation	[mm]
μ_f	Absolute fluid viscosity	[Pa*s]
L_w	Corrugated area width	[mm]
N_p	Number of branch passes	[-]
ϕ	Ratio of the developed surface area	[-]
X	Adimensional parameter of the corrugation	[-]
$\overline{Re}$	Average Reynolds number	[-]
$\bar{V}$	Average velocity in the branch	[m/s]
ρ_f	Massic density of the fluid	[kg/m³]
$\overline{P_{OUT}}$	Average pressure at the outlet	[Pa]

$\overline{P_{IN}}$	Average pressure at the inlet	[Pa]
G_p	Massic velocity at the inlet port	[kg*m/s]
g_c	Crossflow mass velocity	[kg*m/s]
g	Gravity acceleration	[m/s²]
L_V	Corrugated area length	[mm]
$\bar{\tau}$	Average shear stress	[Pa]
σ	von Mises equivalent stress	[Pa]
δ_z	Directional displacement in z-axis, separation	[mm]
δ_y	Directional displacement in y-axis, stretching	[mm]
δ_x	Directional displacement in x-axis, widening	[mm]
$\Delta\delta_z$	Uniform spacing	[mm]
ε_i	Normal strain	[-]
γ_{ij}	Shear strain	[-]
δ_i	Directional displacement	[mm]
ν	Poisson's coefficient	[-]
G_m	Shear modulus	[GPa]
E	Young's modulus, elastic modulus	[GPa]
ΔP_{in}	Pressure difference between the inlet of both branches	[Pa]
$P_{in,i}$	Inlet pressure in branch i	[Pa]
$\Delta P_{in,rod}$	Pressure difference between the inlet rod measurements	[Pa]
$\Delta P_{in,corrected}$	Pressure difference with zero's compensation	[Pa]
$P_{rod,i}$	Pressure of branch i measured at the rod	[Pa]
E_t	Transversal elastic modulus	[GPa]
K_g	Gasket stiffness	[N/m³]
K_{eq}	Equivalent stiffness	[N/m³]
F_o	System force	[N]
F_{eq}	Equivalent force	[N]
$P_{sealing}$	Sealing pressure	[Pa]
m	Experimental factor of the gasket	[-]
ΔP_{EXP}	Pressure drop measured experimentally	[Pa]
ΔP_{NUM}	Pressure drop measured numerically	[Pa]

SUMMARY

1 INTRODUCTION

Heat exchangers are vital to the chemical, process, power, heating, air conditioning and refrigeration industries. As a result, many companies are engaged in the development of various numbers and types of heat exchangers. (KAKAÇ; LIU; PRAMUANJAROENKIJ, 2020). The significance of heat exchangers has increased tremendously over the past three decades with regard to energy conservation and the adoption of new sources of energy. (SHAH; SEKULIC, 2003).

A popular type of heat exchanger is the gasketed plate heat exchanger. It separates the working fluids using corrugated plates and determines the flow path with sealing gaskets. These heat exchangers are commonly used in the cryogenic, food, and chemical industries because they are versatile in handling more than two fluid branches. (ADOLFSSON; RASHID, 2016).

In the oil industry, heat exchangers are commonly applied in the extraction and processsing in site. Oil from the wells is typically pumped to these devices where it is divided between branches. Simultaneously, hot water flows in a secondary branch, heating the oil. Subsequently, oil is returned to the wells. This continuous process helps facilitate the extraction of the oil's complete volume by gradually increasing the heat transfer in it. The heat exchangers that utilize water as their working fluid in two thermal exchange branches are mainly employed to heat the water bed. The heated water will then heat the fluid used in the process mentioned above. The thermal exchange efficiency between water and oil is reduced by poor fluid allocation, layers of incrustation, and the age of the heat exchanger (ADOLFSSON; RASHID, 2016).

Gasketed plate heat exchangers (GPHEs) are subject to multiple operational factors that may result in failures and decreased performance. These factors comprise pressure and temperature cycles, which may cause structural fatigue, incrustations that can lead to corrosion, and mechanical deformations and thermal expansions within the plates that may cause the seals to loosen and create leakage.

This complexity results in a multitude of issues that can be studied and optimized using various methodologies consistent with each stage of analysis. Thus, a considerable number of studies on gasketed plate heat exchangers can be found in the literature, which focuses on numerical, experimental, and analytical methods to individually analyze the structural, thermal, and hydrodynamic aspects of the devices.

The area of interface between phenomena in GPHEs is limited and is only used in simplified studies of thermo-structural optimization. In contrast, shell-and-tube exchangers exhibit more extensively examined harmonic phenomena in the literature. This research intends to address this scarcity of work developed on multiphysics coupling.

One reason for insufficient data on this type of problem concerns evaluating fluid-structural interaction (FSI), a coupling phenomenon that is hard to assess. Other names or terms that refer to this phenomenon include elastic deformation of corrugated panels, breathing effect, and separation effect. The analytical approach provides useful insights into geometry and basic phenomena, restricted by the mathematical complexity linked to solving complex equation systems that include each physical aspect of the relevant phenomena. Experiments into the heat exchanger are confined to the peripheral behavior of plates due to the risk of interfering with the flow by inserting pressure, temperature, and velocity sensors at specific branch points. The tightness of the plates also complicates installing strain gauges in the exchanger pack. However, while providing detailed predictions of the device behavior above and beyond the previous analyses, the numerical approach is subject to limitations on computational power with the increased complexity of the problem under study.

This study aims to assess two numerical methodologies for analyzing fluid-structural couplings in GPHEs. The aim is to gain insights about the limitations of geometric and mathematical solution simplifications and evaluate the precision of the results obtained by each methodology.

1.1 GENERAL OBJECTIVE

This study aims to assess hydrostatic analysis and one-way fluid-structural interaction (FSI) methodologies for computational cost and precision regarding the flow and structure coupling with feedback in a simplified GPHE exchanger.

1.2 SPECIFIC OBJECTIVES

- Study the fluid-structure interaction behavior in GPHE heat exchangers;

- Define a methodology with feedback for hydrostatic analysis using uniform spacing variation;
- Understand the limits and needs for the application of the one-way FSI methodology;
- Validate the hydrodynamic and structural results with experimental data;
- Compare the proposed methodologies and evaluate them using computational cost and precision as metric variables.

1.3 JUSTIFICATIVE

The study of elastic deformation in the corrugated plates of gasketed-plates heat exchangers (GPHEs) is of paramount importance in the field of heat transfer and fluid dynamics. These complex heat exchangers are widely used in various industrial applications due to their high efficiency and compact design. Understanding the elastic behavior of the corrugated plates is essential to optimize their performance and ensure their structural integrity. Elastic deformation can significantly affect the thermal and mechanical performance of GPHEs, leading to potential efficiency improvements or structural failure if not comprehensively analyzed. Therefore, studying the elastic deformation of these corrugated plates is not just an academic exercise, but a practical necessity for engineers and researchers in the field.

In order to conduct a thorough investigation of the elastic deformation in GPHEs, the use of optimal numerical analysis methods is imperative. Traditional analytical approaches may prove insufficient to accurately capture the complex geometries and boundary conditions of corrugated plates. Numerical simulations, such as finite element analysis (FEA) or computational fluid dynamics (CFD), provide the means to model the complex interactions between fluid flow and structural deformation in these heat exchangers. The use of optimal numerical analysis methods allows researchers to explore a wide range of design variables, evaluate the effects of various operating conditions, and predict the performance of GPHEs under different scenarios. Consequently, the application of advanced numerical techniques not only improves the accuracy of predictions, but also facilitates the development of innovative design strategies for more efficient and reliable GPHEs, making it an essential component of research in this field.

1.4 WORK ORGANIZATION

The text here presented is divided into three chapters: Bibliographic Review, Methodology, and Results and Discussions. The second chapter, Bibliographic Review, discusses important aspects of the object of study and the problem raised from a Theoretical Fundamentals perspective. This chapter concludes with a bibliometric study of GPHE heat exchangers and their state-of-the-art in the Literature Review, divided in three main subjects: termal-hydrodynamic performance, structural performance and fluid-structural interaction.

The third chapter, Part I - Experimental Analysis, details the assembly and operation of the experimental data acquisition benches used to validate the numerical results obtained by the proposed methodologies. One of the benches uses a four-plate GPHE (similar to the numerical setup) and evaluates it hydrodynamically, without heat exchange. The second is a hydrostatic bench, which uniformly pressurizes a GPHE with a greater number of plates and collects data that defines the deformation state of such a device. Furthermore, Part I ends with a discussion of the pressure and deformation data acquired by the benches.

The fourth chapter, Part II - Numerical Analysis encompasses the presentation of the two approaches evaluated in this study: hydrostatic numerical analysis and one-way FSI numerical analysis. This chapter indicates the numerical methods used (CFD and FEM), the geometries, the boundary conditions, the physical and mechanical properties of the materials used, the simplifying assumptions and relevant modeling, the solution meshes, the hardware used, the convergence criteria and the definition of the cases evaluated in each one of the approaches. The chapter, finally, presents the results obtained in each stage of each approach, compares these results with those obtained experimentally as a form of validation and shows the evaluation of the approaches in relation to the computational cost required by each one. Chapter 5 is dedicated to the work's conclusion.

2 BIBLIOGRAPHIC REVIEW

2.1 THEORETICAL FUNDAMENTALS

Gasketed Plate Heat Exchanger (GPHE) devices are thermal devices used in industry to regulate processes that require precise control of fluid temperature and pressure, for instance, milk pasteurization and oil extraction processes.

GPHEs operate by assembling and sealing corrugated plates together. After being initially tightened, the corrugated plates form channels for fluid flow in each section. A sealing gasket separates each section from the other. Considering a single plate, hot fluid passes on one side and cold fluid passes on the other side, enabling heat transfer through the metal.

Figure 1 presents the cross arrangement of gaskets and channels. The Chevron angle (or herringbone) is the angle formed between the corrugations of both plates measured from the vertical axis.

Figure 1 – Plates showing gaskets around the ports

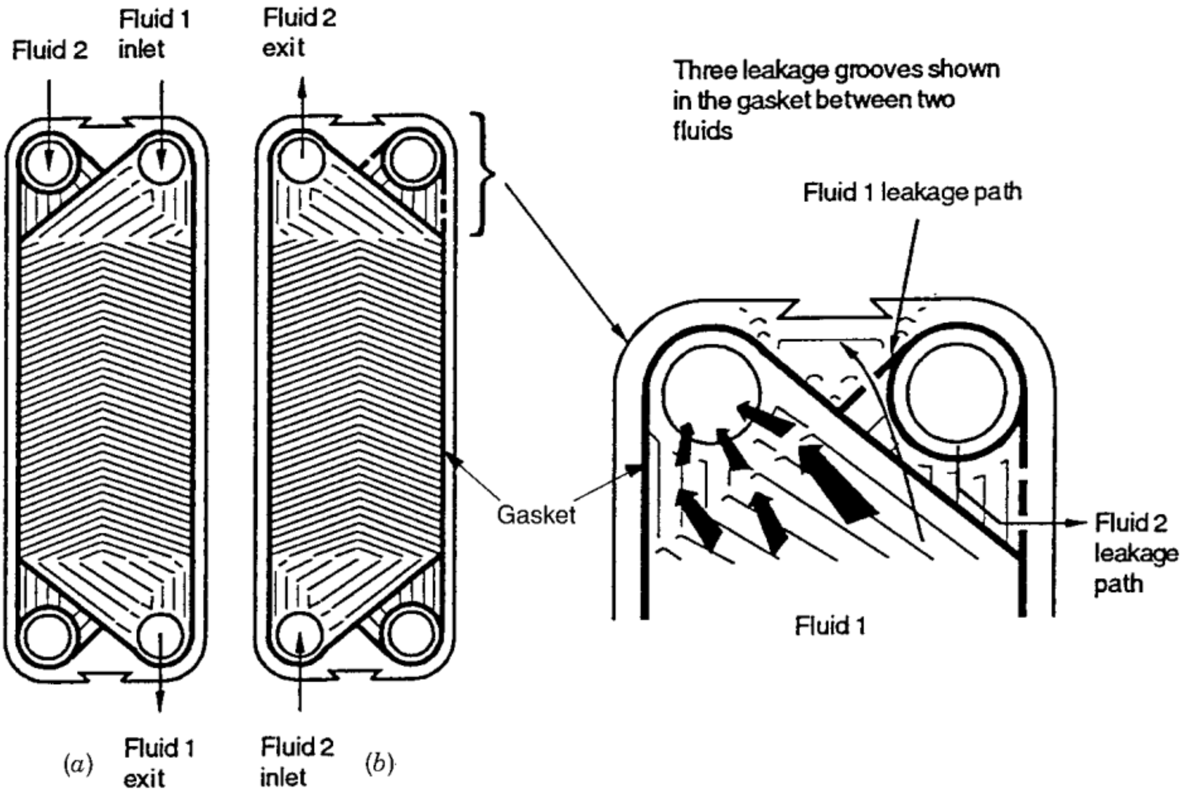

Source: Shah and Focke (1988) apud Shah and Sekulic (2003). a) Arrangement of gaskets; b) Arrangement of fluid volumes; c) Detail of the Chevron angle formed by the crossing of the channels.

The main elements in a GPHE are:

1. Corrugated plates: arranged in different configurations to achieve the expected temperature and pressure values. A set of these plates is called a pack;
2. Hangers/Racks: lower and upper support beams to which the plates are attached to run on the structure, helping to align the pack;
3. Cover plates: plates added at the beginning and end of the pack to homogenize its tightness;
4. Gaskets: strips made of elastomer that promote the sealing of the plates, preventing the fluid branches from mixing;
5. Tie rods: threaded bars that cross the pack around the perimeter of the tops, promoting its tightness;
6. Nozzles/Ports: where fluids from both branches enter and leave the device.

Figure 2 shows the location of each item listed above. Gaskets are located inside the pack, between each pair of plates.

Figure 2 – GPHEs nomenclatures

Source: Adapted from Alfa Laval (2022). Indication of the main components of a GPHE: 1 – Pack of plates, 2 – Hanger, 3 – Worktops, 5 – Tie rods, 6 - Nozzles.

Figure 3 displays a typical GPHE plate presenting the nomenclature of all the relevant regions and dimensions analyzed in this work:

- Inlet port: Fluid admission region in the pass;
- Inlet's distribution gallery: fluid distribution region to ensure the best possible uniformity upon entry into the heat exchange region;
- Thermal change/Heat Exchange channel: region where the lattice gallery is located, formed by the chevron angle of the plates, and in which there is effective thermal exchange;
- Outlet's distribution gallery: fluid collection region to redirect flow in the direction of the pass exit;
- Outlet port: fluid exit region of the pass;
- Port diameter (d_p): main dimension of fluid inlet and outlet;
- Chevron angle (β): angle formed between the corrugations of the two plates of the pair, measured from the vertical axis;

- Fluid length (L): vertical dimension of the fluid volume, measured within the perimeter of the gasket;
- Fluid width (W): horizontal dimension of the fluid volume, measured within the perimeter of the gasket.

Figure 3 - Main regions and dimensions of the plates used in GPHEs

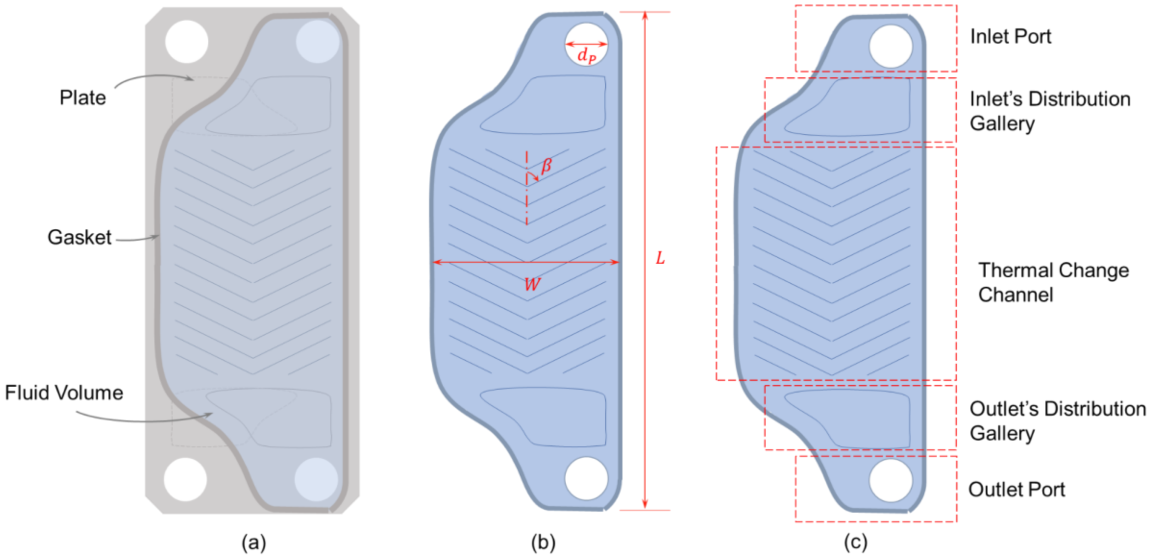

Source: Author (2023). a) Location of gasket and fluid volume on the plate; b) Main measures: ports diameter (dp), Chevron angle (beta), length (L), width (W); c) Analysis regions.

Figure 4 outlines two flow configurations of GPHE type heat exchangers: the first, in parallel, assumes that the hot and cold fluids are injected into each channel in the same direction. In the countercurrent configuration, the fluids are injected crosswise. Countercurrent flow configurations generally have higher heat transfer rates.

Figure 4 - Operation of gasketed plate heat exchangers for countercurrent and parallel arrangements.

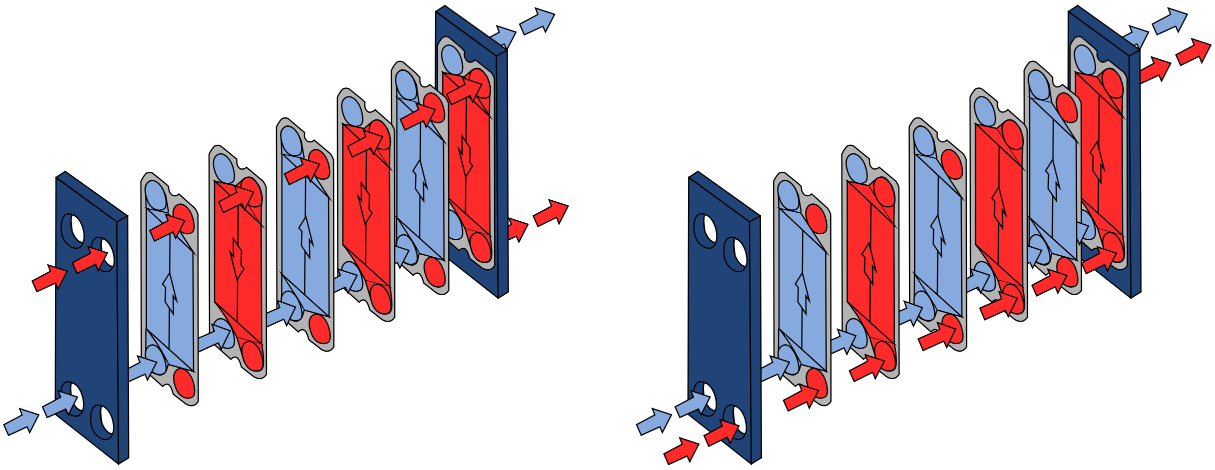

Source: Author (2023). Left: Countercurrent arrangement; Right: Upward parallel flow arrangement.

Detailed information about configurations, classification, arrangements, types and functioning can be found in the literature (KAKAÇ; LIU; PRAMUANJAROENKIJ, 2020; INCROPERA et al., 2007; SHAH; SEKULIC, 2003). Other types of heat exchangers that work with plates are Plate-Fin Heat Exchangers (PFHE), Brazed Plates Heat Exchangers (BPHE) and Plate-and-Shell Heat Exchangers (PSHEs)

Figure 5 shows a set of corrugated plates and the corresponding loads acting on them (Figure 5-a and Figure 5-b). There are two primary loads that apply within this context: the hydrodynamic pressure of the flow and the tension generated by the metal. This stress comes from pressure on the external flow, crossing the reference face and is transmitted in the opposite direction to the fluid volume under pressure P_{fluid}. These loads do not necessarily balance each other.

Figure 5-c shows how the pack cross-section behaves as a pressure vessel, causing the metal to inflate while its ends are fixed. Figure 5-d demonstrates how the cross-section behaves when isolated from solid stress or external flow pressure. In such a case, the outflow channel is constricted. These phenomena are known as the separation/expansion and constriction of the plates, respectively.

Figure 5 - Fluid-structural behavior of GPHE plates

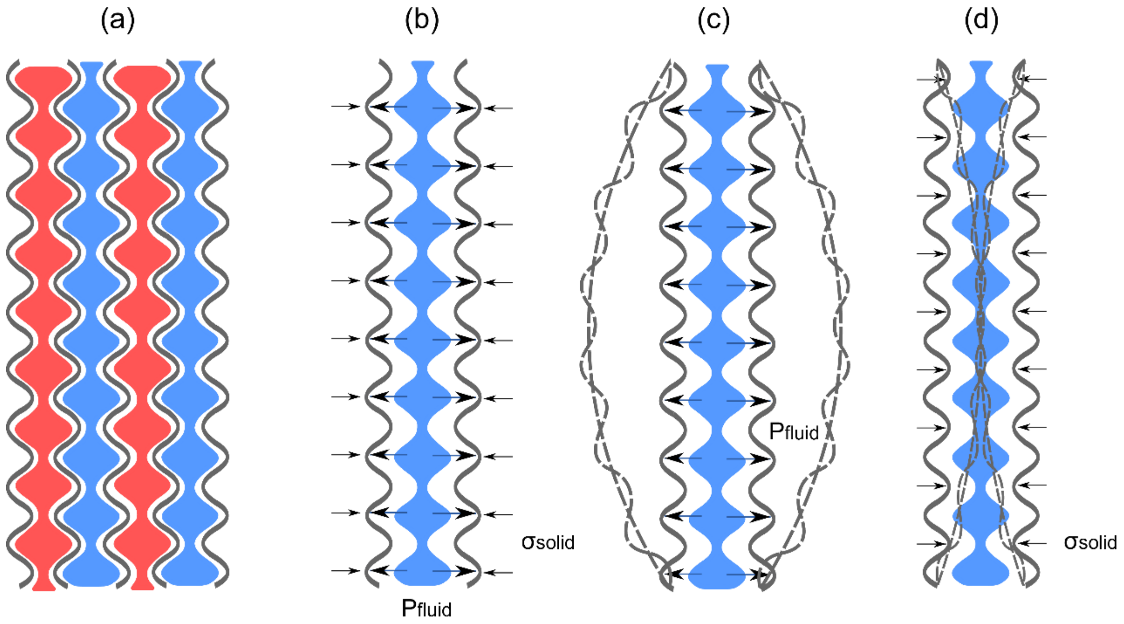

Source: Author (2023). a) Cross section of a pack of 5 plates; b) Forces acting on a pair of plates; b) Behavior of the plates under internal flow pressure; d) Behavior of the plates under the action of the tension generated by the action of the external flow.

In reality, both loads act simultaneously resulting in feedback in the system, wherein the flow deforms the solid and the movement of the solid disrupts the fluid. To gain a better comprehension of the fluid-structural interaction phenomenon, please consult the literature (BUNGARTZ; MEHL; SCHÄFER, 2010; HAASE; WINDZELL; SELMIN, 2002; MOUBACHIR; ZOLÉSIO, 2006; PAÏDOUSSIS, 1998).

Apart from the change in spacing, which results in a change in the geometry perpendicular to the central plane of the plates, the plates also experience two more forms of deformation concerning their perimeter, namely elongation and widening, as demonstrated in Figure 6.

Figure 6 - Widening (width variation) and stretching (length variation) behavior of a GPHE plate.

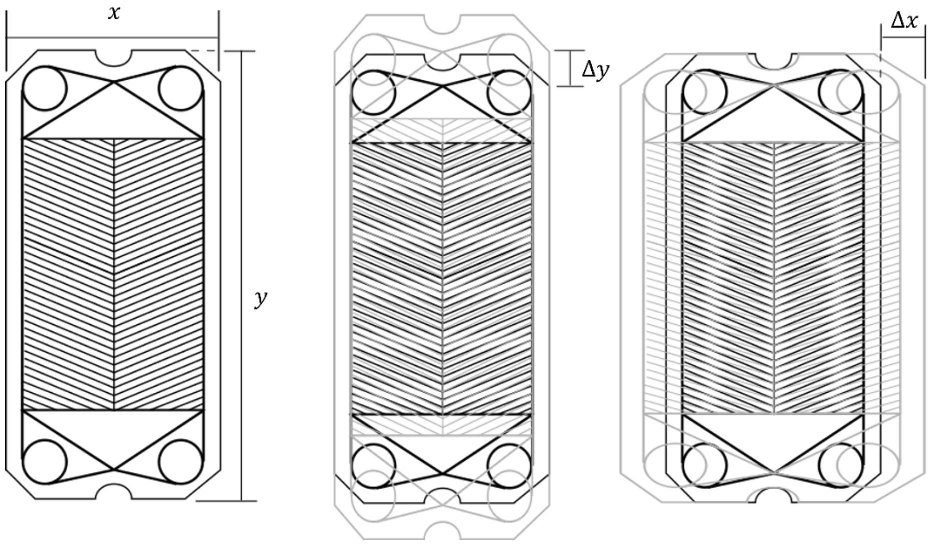

Source: Author (2023). Left: Original dimensions; Center: Length variation (stretching); Right: Width variation (widening).

The study of the behavior of such devices is significant to evaluate their performance and identify and estimate failures, whether structural or functional.

Different evaluation methods can be found in the literature, such as experimental tests, empirical and analytical correlations, and numerical simulations used for study or optimization. A bibliographical study has been developed to determine the state-of-the-art in this field and can be reviewed in the following sections.

2.1.1 Performance parameters

Several variables can be used to characterize the operation of GPHEs, whether they are hydrodynamic, thermal or termo-hydrodynamic parameters. Three of them stand out for use in this work: the Reynolds number (Re), which defines the flow regime of the fluid domain; and the pressure drop (ΔP), which defines the pressure difference between the inlet and outlet of the domain.

The initial Reynolds number Re_{in}, which is the Reynolds number calculated at the entrance of the fluid branch, is given by equation (8) (SHAH; SEKULIC, 2003). The Re_{in} is used to determine the range of input speeds used in the operation of the device and is one of the input parameters for numerical analysis. It is a dimensionless number and each fluid branch has its own Re_{in}, since the fluids do not mix and have different numbers of passes.

$$Re_{IN} = \frac{G \cdot D_h}{\mu_f} \tag{1}$$

$$G = \frac{\dot{m}_{in}}{A_0} \tag{2}$$

$$A_0 = b \cdot L_w \cdot N_p \tag{3}$$

$$D_h = \frac{D_e}{\phi} \tag{4}$$

$$D_e = 2b \tag{5}$$

$$\phi \approx \frac{1}{6}\left(1 + \sqrt{1 + X^2} + 4\sqrt{1 + \frac{X^2}{2}}\right) \tag{6}$$

$$X = \frac{\pi b}{P_c} \tag{7}$$

$$Re_{IN} = \frac{\left(\frac{\dot{m}_{in}}{b \cdot L_w \cdot N_p}\right) \cdot \left(\frac{2b}{\phi}\right)}{\mu_f} \tag{8}$$

In the equations above:

- G is the massic velocity;
- D_h is the hydraulic diameter of the corrugation;
- D_e is the effective diameter of the corrugation;
- μ_f is the fluid absolute viscosity;
- $\dot{m}_{in}$ is the mass flow at the branch inlet;
- A_0 is the total free-flow area of one of the branches;
- L_w is the width of the plates;
- b is the height of the corrugation;
- N_p is the number of branch passes;
- ϕ is the ratio of the developed (actual) surface area. Normally, 1.15 > ϕ >1.25 (SHAH; SEKULIC, 2003, p.597);
- X is the adimensional parameter of the corrugation;
- P_c is the corrugation period.

The average Reynolds number in the branch, ($\overline{Re}$), is defined by Equation (9). In it, $\bar{V}$ is the average velocity in the branch and ρ_f is the density of the fluid.

$$\overline{Re} = \frac{\bar{V} \cdot \rho_f \cdot D_e}{\mu_f} = \frac{\bar{V} \cdot \rho_f \cdot 2b}{\mu_f} \tag{9}$$

The $\overline{Re}$, as calculated at all points in the branch after obtaining the steady state, is defined as the output parameter of numerical analysis and can be related to the analysis of turbulent flow patterns within corrugated channels.

The pressure drop ΔP is defined by Equation (10), in wich $\overline{P_{OUT}}$ is the average pressure calculated or measured at the outlet port region and $\overline{P_{IN}}$ is the average pressure calculated or measured at the inlet port region.

$$\Delta P = \overline{P_{OUT}} - \overline{P_{IN}} \tag{10}$$

Pressure drop is an output parameter of the numerical analysis.

2.1.2 Structural parameters

To characterize the structural behavior, the following parameters are defined: von Mises equivalent stress (σ), which is the multidirectional equivalent stress for a three-dimensional domain; the directional displacement in X (δ_x), which quantifies the widening of the domain; the directional displacement in Y (δ_y), which quantifies the stretching of the domain; and the directional displacement in Z (δ_z), which quantifies the separation of the domain. The axes will be referenced graphically in the following sections (Figure 17).

The normal strain ε_i and the shear strain γ_{ij} are also defined, which quantify the variation of the directional displacement δ_i in relation to the initial condition (undeformed), where $i = (X, Y, Z)$. Equations (11) and (12) indicate, respectively, the definition for normal and transversal (shear) deformations.

$$\varepsilon_i = \frac{\sigma_i}{E} - \frac{\nu}{E}\left(\sigma_j + \sigma_k\right) = \frac{1}{E}\left[\sigma_i - \nu\left(\sigma_j + \sigma_k\right)\right] \tag{11}$$

$$\gamma_{ij} = \frac{\tau_{s,ij}}{G_m}; \gamma_{jk} = \frac{\tau_{s,jk}}{G_m}; \gamma_{ik} = \frac{\tau_{s,ik}}{G_m} \tag{12}$$

Where: E is the modulus of elasticity of the structure material; ν is its Poisson coefficient; ε_i is the strain in the i direction; σ_i is the normal stress in the i direction; σ_j and σ_k are the stresses in the directions orthogonal to the i direction; γ_{jk} is the transverse strain in the plane orthogonal to the i direction; $\tau_{s,jk}$ is the shear stress of the structure in the plane orthogonal to the i direction and G_m is the shear modulus of the structure material.

The following equations define the von Mises equivalent stress used to predict the yielding of a material when multi-axial loads are applied to the body.

$$\begin{bmatrix} \sigma_{xx} & \sigma_{xy} & \sigma_{xz} \\ \sigma_{yx} & \sigma_{yy} & \sigma_{yz} \\ \sigma_{zx} & \sigma_{zy} & \sigma_{zz} \end{bmatrix} \tag{13}$$

$$\sigma_{vm} = \sqrt{\frac{\left(\sigma_{xx}-\sigma_{yy}\right)^2+\left(\sigma_{yy}-\sigma_{zz}\right)^2+(\sigma_{zz}-\sigma_{xx})^2+6\left(\sigma_{xy}^2+\sigma_{yz}^2+\sigma_{zx}^2\right)}{2}} \tag{14}$$

2.2 LITERATURE REVIEW

For the development of this study, the following key terms were defined in the search for related works that could be used as a theoretical or methodological basis: heat exchanger, plates, fluid-structure and separation. These terms are related to the device analyzed, the classification of the device, the phenomenon analyzed and the problem studied.

Based on previous experience with this type of search (DONATI et al., 2021; TASCHECK et al., 2022), key terms related to the analysis method were discarded so that the search was not drastically limited at the first pass.

At first glance, it is possible to see the tendency of the term "fluid-structure" to appear related to dynamic analysis - mainly vibration - and optimization, which are the most used analysis problems and tools for this type of phenomenon, but, since this study focuses on static analyses and does not propose modifications to the heat exchanger itself, works focusing on these types of analysis are primarily discarded.

Based on a search of the Scopus platform, about 360 papers in the last 30 years (1993-2023) present results (in title, keywords or abstract) of analyses of heat exchangers with a focus on fluid-structure interactions. Of these, only 19 respond to the addition of the term "plates" in the search and are not related to vibrational or optimization analysis. The others focus on other heat exchanger configurations with simpler geometries, such as shell-and-tube, printed circuit plate, and plate fin.

As for the analysis of plate separation in GPHE type heat exchangers, without reference to vibration and optimization, 242 results are found. Finally, when the values of fluid-structural analysis and plate separation are crossed, only two works are found.

Figure 7 - Diagram for the bibliometric study

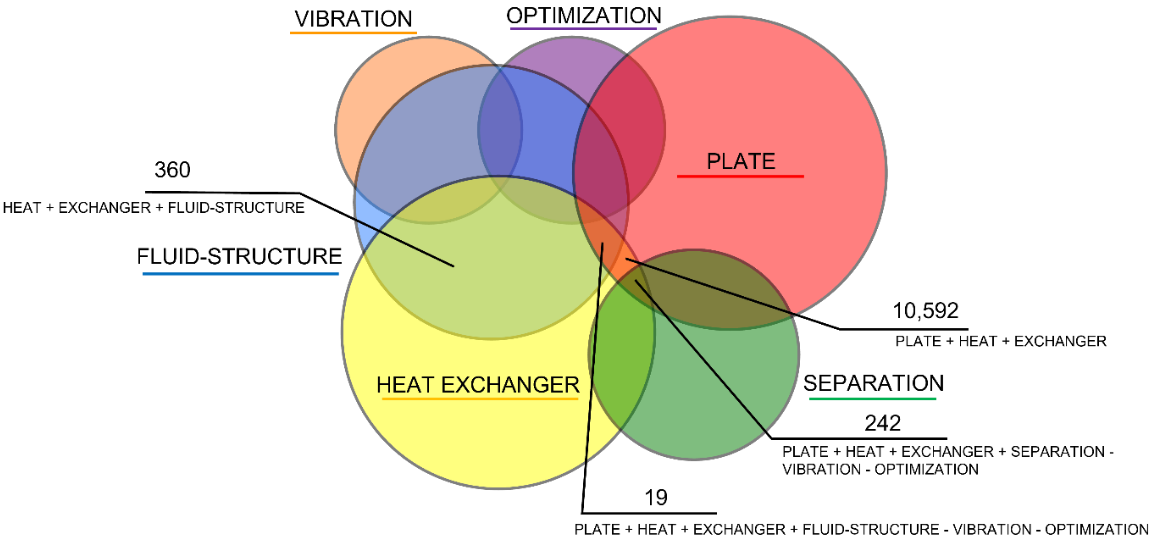

Source: Author (2023).

However, upon further analysis, none of the 242 search-related results with the term "separation" (including the two cited above) use the term in the context of GPHE plaque separation, but rather in the context of fluid treatment processes or mathematical analysis. Figure 7 illustrates the data intersection described above as the basis for the bibliometric analysis.

At the end of this analysis, it is possible to perceive the difficulty that surrounds the definition of works that can serve as a single basis for all the terms primarily defined. Therefore, the strategy followed from this point on was to find a series of relevant works in their own "bubbles" in order to connect them individually in the steps defined in this study.

The following papers illustrate the state of the art in the experimental and numerical analysis of plate heat exchangers (PSHE, PFHE, BPHE, and GPHE) for thermal, fluid dynamic, and structural characterization.

2.2.1 Thermo-hydraulic performance

The works found in the literature that deal with the thermo-hydraulic performance of GPHEs mostly focus on experimental analyses, mostly limited to the periphery of the exchanger, with data acquisition points at the inlet and outlet and global performance estimation.

The results of numerical analyses are aimed at investigating the flow structures (streamlines), velocity and pressure values, as well as friction factor and Nusselt number results, all for the flow inside the plates, in order to study the local behavior. Decoupled from the structural behavior, numerical analysis typically uses coarser meshes when analyzing extensive plate packs, leading to a reduction in the number of plates to apply optimized meshes and consequently more robust turbulence models.

Tascheck et al. (2022) numerically analyzed 3 configurations of plate geometries of PSHE type heat exchangers to evaluate the fluid dynamic behavior of the plates with the change of Reynolds number and chevron angle. The author also evaluated two different turbulence models: $k-\varepsilon$ and $k-\omega$ SST. Meshes of 4, 11 and 52 million elements were compared. The authors compared the numerical results with several correlations for friction factor and Nusselt number for each of the geometry configurations, identifying extremely restricted application ranges, both in relation to the chevron angle of the plate and in relation to the application range of Reynolds number, concluding with the choice of two distinct correlations.

Nguyen et al. (2022) numerically studied a corrugated heat exchanger plate with an airfoil cross section and compared the results with commercial models, usually with a sinusoidal cross section. Geometric parameters such as corrugation angle and inclination, double mirror configuration, and several airfoil profiles were considered in the comparison between the evaluated model and the commercial model through thermo-hydraulic properties such as the average turbulent kinetic energy, the general heat transfer coefficient, the pressure drop, the Nusselt number, and the friction factor. The authors found that the pressure drop in the airfoil channel was approximately 17% lower than in the sinusoidal channel, with virtually no change in the magnitude of heat transfer. Variations in chevron angle resulted in decreases in heat transfer of up to 10% (from 60º to 30º and from 60º to 90º). The largest variations in heat transfer coefficient were observed when the NACA profile was varied: changing from NACA 0025 to NACA 0020 resulted in an increase of 8.9%; changing from NACA 0025 to NACA 0030 resulted in a decrease of 12.2%. This variation is related to the proportionality between the airfoil slope and the heat transfer area of the duct.

Khail and Erisen (2022) numerically investigate the thermal and performance characteristics of a novel plate heat exchanger, focusing on the effect caused by changing the shape of the hyperbolic tangent function that forms the corrugated channel. The simulation domain consists of a 10 mm wide corrugated strip representing two units, with hot water on one side and cold water on the other. The turbulence model chosen was the $k-\omega$ SST, and the mesh was made up of approximately 11 million elements. The results show that increasing the concavity of the hyperbolic tangent function increases the transverse perturbations of the flow, which in turn increases the heat transfer. Compared to the standard novel plate heat exchanger, the heat transfer and performance showed an increase of 13% and 8%, respectively, when using the function $y=\tanh(x)$, while they would be increased on average by 52% and 36%, respectively, for the corrugation depth of 2.5 mm. When compared to other geometries, performance increased by 37%.

Mudhafar (2022) shows the numerical study of the two-phase flow in a model K050 plate heat exchanger, comparing pack configurations with and without a flow distributor at the inlet of the branches. The pack analyzed consists of 10 plates with dimensions of 306mmx106mmx0.4mm, a chevron angle of 65º, and a channel depth of 2mm. The method used to solve the two-phase problem was VOF (Volume Fraction of Fluid) using FLUENT software. Reynolds number values of 500, 1500 and 300 were used for evaluation. The main boundary conditions are constant inlet velocity, zero relative outlet pressure and a non-slip wall. The turbulence model used is the $k-\varepsilon$ realizable one. For the case without the distributor, the results show that the heat exchanger must operate at high Reynolds numbers to achieve better fluid distribution, since for operating conditions with $Re<1500$ the liquid-vapor distribution is non-uniform. When the distributor is added to the inlet, this distribution is significantly improved at low Re and is not affected at high Re.

Restrictions on geometry and computational capacity are major obstacles in the numerical prediction of the real behavior of GPHEs, especially when such predictions do not take into account the interfaces between branches and other factors external to the flow. An option to overcome such restrictions is decoupled structural analysis, which helps in understanding the critical points of the structure (plates) that can influence the behavior and performance of GPHEs.

2.2.2 Structural performance

The main monitoring variables for the structural performance of GPHEs are the stress state and the deformation state of the plates. The first indicates the points of probable failure, the residual stress between the assembly and loading stages and, through fatigue life analysis, the number of cycles that the thermal device can operate under the given conditions. The second indicates the deformation modes and, consequently, the geometry variation, highlighting the points of probable leakage, failure and interference with the fluid.

Nascimento (2013) conducted a study on gasketed Plate Heat Exchangers (PHEs) of SB-2g5 Gr.1 Titanium alloy plates and hydrogenated nitrile rubber (HNBR) gaskets. The study employed analytical models and numerical simulations to investigate gasket failure. The first analytical model utilized linear stiffness assumptions and plate behaviors, identifying that increasing initial clamping force elevated the required pressure for leakage. A subsequent two-dimensional analysis used Fourier series expansion to estimate displacement considering contact forces. This model, developed using MATLAB, closely aligned with finite element simulations. A three-dimensional model was also developed, focusing on a single sector of the corrugated plate with shell elements and subsequent replication. The study assessed residual stress, showing minimal impact from plate pressurization on elastic bases due to initial compression.The research compared analytical models to ANSYS Mechanical APDL numerical simulations. ANSYS models represented portions of the plate geometry, applying simple supports and pressures to emulate real conditions. The friction coefficient between plates was treated as unknown, leading to a rough contact model. External plates were subjected to average displacement, compressing central plates to mimic initial compression. Lastly, a model analyzed stress distribution on the plate, showing heightened stress at contact points in the central region, surpassing material yield limits.

Pelliccione et al. (2019) investigated the failure of Plate Heat Exchangers (PHEs) utilizing ANSYS Mechanical APDL software, and examined a PHE that had been removed from operational use due to malfunction. The exchanger, designed with 0.6 mm thick plates of ASTM B265 Grade 1 titanium alloy, experienced failure after 126,000 hours of operation under varying pressures and temperatures. The PHE used seawater and clean water as working fluids, with differing inlet temperatures and pressure ranges for each channel.

Macroscopic cracks were visually detected in specific regions of the plates, primarily within the sealing area. Analysis of the cracked region revealed the presence of a brittle titanium hydride phase, which contributed to crack propagation in the titanium alloy. The researchers employed a 3D laser scan to capture the exchanger plate's geometry for modeling purposes. In their numerical model, the contact surfaces exposed to seawater and clean water were subjected to prescribed pressure loads, while the gasket region received a sealing pressure of 2 MPa. Notably, residual stresses arising from plate manufacturing processes were not factored into the model. The plate's vertical edges were supported in different directions, and the numerical model highlighted higher stress concentrations in areas corresponding to the crack-prone regions.

Santiago (2021) evaluated the structural performance of PSHE heat exchanger plates in terms of static loading and fatigue life. The test involved applying a uniformly distributed load first to the inner plates of the 4-plate pack modeled for evaluation. Load tests were also developed on the outer branch and both branches. The author found that the maximum stress points of the plates were at the contact points and the average stress of the plates was estimated to be between 10 MPa and 30 MPa for compression load values of 0.8 MPa and 1.6 MPa, respectively Nevertheless, the author confirmed results form the literature, which indicated that the failure of these exchangers occurred in the external soldering of the plates. From the contact area of the analyzed plates it was possible to identify a contact zone larger than the points of maximum stress, in addition to the decentralization of these points with respect to the crest of the corrugations. Three failure criteria were evaluated in the study to estimate the fatigue life of the exchanger under the described loading values, in single (only one pressurized branch) and double (both pressurized branch) loading situations.

Martins et al. (2022) experimentally and numerically evaluated two gasketed plate heat exchangers (GPHE) using a pressurization test rig to investigate the structural behavior of the exchanger plates. The tests included pressurization of a single flow branch (single test) and later pressurization of both branches (double test). The numerical model started from the simplification of the plate pack to a set of 4 plates sectioned just below the fluid distribution region - the region of interest for the study - and added the operating conditions indicated by the experimental tests.

The results of the study showed agreement between the two approaches, with the seal channel with the free span of the fluid distribution area being the one with the highest stress concentration. The single tests showed higher stresses than the double tests, indicating that loading of both branches is essential for the functioning of the exchanger. Finally, high stress values were found in the exchanger assembly process, indicating that this part of the device's operation is critical.

The trend found in the studies above, as well as in the literature, is the simplification of loads and decoupling of phenomena. Studies found that work with variable loads coming from the flow study exclusively thermal loads, which, in comparison, do not stress the device as much as mechanical loads.

2.2.3 Fluid-structural coupling

The analysis of elastic deformation of GPHEs plates is a recent advent, as demonstrated in the bibliometric analysis previously presented. Few studies study the influence of non-uniform mechanical loads on the structure of heat exchangers and, for the most part, they present purely experimental approaches. In devices with simpler geometries, such as PFHE, more studies and numerical tests can be found regarding this problem.

Lychakov et al. (2017) experimentally studied the effect of breathing (the authors' name for the effect of elastic deformation/separation of plates) in GPHEs using different pack configurations (9, 15, 21, 31, and 65 plates). Symmetric and asymmetric loads were analyzed. The results indicate that the friction factor depends not only on the Reynolds number value, but also on the pressure difference between the branches (or between the sides of the plate) and the initial tightness of the pack. For packs with larger surface area, the friction factor in the lower pressure branch was 3 to 3.5 times higher than in the higher pressure branch. For packs with a smaller surface area, the difference does not exceed 1.5 times. In addition, the study indicates that flat gasket geometries tend to reduce the breathing effect.

The authors then suggest the use of two expressions to approximate the friction factor for two different ranges of pressure difference between the branches. In terms of design, the authors point to changes in the geometry of the plates, such as the application of movement stop sections on their surface, which increase their stiffness but create recirculation zones that can generate greater deposition of solid particles.

Li et al. (2020) analyze the influence and optimization of geometric parameters on the flow, heat transfer, and stress state of serrated fin cryogenic heat exchangers (PFHEs) using the fluid-structural interaction method. The results show that the thermal stress is significantly lower than the mechanical stress, and that the regions of maximum stress are located in the corners that have not undergone smoothing, mainly at the junction of two fins. As for the variation of the geometric parameters, the length of the fins proved to be the most influential on the heat transfer, in addition to having the greatest interaction between the parameters when compared to the spacing between the fins. As for the pressure drop, the greatest influence is outside the thickness of the fins and the greatest interaction is outside between thickness and spacing. After implementing the Multi-Objective Genetic Algorithm (MOGA), the JF factor - which quantifies heat transfer and pressure drop - was reduced by up to 9.6% and the stress was reduced by up to 42.3%.

Wang et al. (2017) developed an analysis similar to that of Li et al (2020), however, their objective was the optimization of shell and tube heat exchangers (STHE) with helical cover plates. The critical shear stress points on cover plates were found at the junctions between cover plates and tubes. The maximum values are equivalent to less than half of the allowable stress. The results of the MOGA method were compared with numerical data and errors of +/- 10% were found.

Wen et al. (2018) investigated a fluid-structural interaction analysis of a finned exchanger. The fins, referred to as sine-wavy or sinusoidal, possess undulations along their length. The stress results reveal peak values at the inlet and outlet of the vane region, while the local maxima from the analysis paths converge at the crests of the sinusoid. Also, the highest stress was directly proportional to the wavelength of the sinusoid and the spacing between the vanes, and indirectly proportional to the thickness of the vanes and the amplitude of the sinusoid.The results of parameter variation show that the j-factor (which quantifies heat transfer) increases with increasing fin height and fin spacing, but decreases with increasing fin thickness, sinusoid wavelength, and flow inlet velocity. The j-factor increases with the amplitude of the sinusoid, but decreases after a certain point. The f parameter (which quantifies pressure drop) increases with sinusoid amplitude, fin spacing, and fin height, and decreases with fin thickness, sinusoid wavelength, and flow inlet velocity.

Donati et al. (2021) developed numerical work to compare two approaches for characterizing PSHE heat exchanger plates in terms of stress state and plate separation. Hydrostatic and hydrodynamic pressure loads were evaluated to verify the need to apply FSI analysis. A 4-plate pack was modeled with the two end plates acting as restraints and the plates inside the pack receiving the compressive load. It was verified that at low Reynolds numbers ($Re < 8000$) the FSI analysis is necessary to characterize the stress state of the plates, but not for their separation. The study also verified that there is no need for feedback in the FSI system for the evaluated Reynolds range, since the magnitudes of normal displacement do not exceed 5% of the thickness of the plates.

The most common application of fluid-structure interaction analysis in the literature is the optimization of geometries. Specifically for heat exchangers, numerical analyses generate data for the validation of optimization algorithms for fins, cover plates and plates, with the intention of finding the relationship between geometric and fluid-thermodynamic parameters, with consequences on the stress state of the devices.

Based on the presented review, the need for more in-depth studies on the phenomenon of separation (elastic deformation, breathing) of GPHE heat exchanger plates is remarkable, both for the characterization of the behavior resulting in the structure and flow, and for the definition of effective methodologies for this characterization.

3 METHODOLOGY

3.1 EXPERIMENTAL METHODOLOGY

3.1.1 Hydrodynamic tests

In order to validate the results obtained in simulations of GPHE packs with elastic deformation effects caused by fluid-structure interaction and to study potential effects found in heat exchangers, an experiment was conducted on a hydrodynamic bench. An heat exchanger was assembled with four 60-degree Chevron angle plates, identical to those employed in the numerical method. Parallel and countercurrent flow conditions were applied in a set of 12 cases addressing symmetrical and asymmetrical inlet pressure conditions, flow rate variations, and pressure drop variations between the branches. The plates, made of 316L steel, had a corrugation height of 2.5 mm, a thickness of 0.57 mm and were spaced approximately 2.005 mm apart.

Since the number of plates is even, the number of branch passes is odd. The internal branch has one pass and the external branch has two passes, which results in three fluid passes. In the parallel configuration, both branches have downward flows. However, in the countercurrent configuration, the internal branch ascends and the external branch descends. Figure 8 displays the actual workbench, showing the main elements alongside the GPHE and the flow configurations employed in the tests. In this figure, the internal Branch is identified as a red fluid and the external brandi s identified as a blue fluid.

Figure 9 and Figure 10 display the bench operation flowchart for the countercurrent flow configuration and the parallel flow configuration, respectively. The tests described here do not consider heat exchange, only the hydrodynamic performance of the heat exchanger.

Table 1 lists the instruments and equipment installed on the bench. The bench is composed of:

- 1.0 m³ cold fluid reservoir equipped with resistive sensors for thermal control;

- Pumps with flow controlled by frequency inverters;
- Coriolis flow sensor for mass flow measurement;
- Absolute and differential pressure transducers for measuring inlet pressures and pressure drop.

Figure 8 - Hydrodynamic bench setup configurations

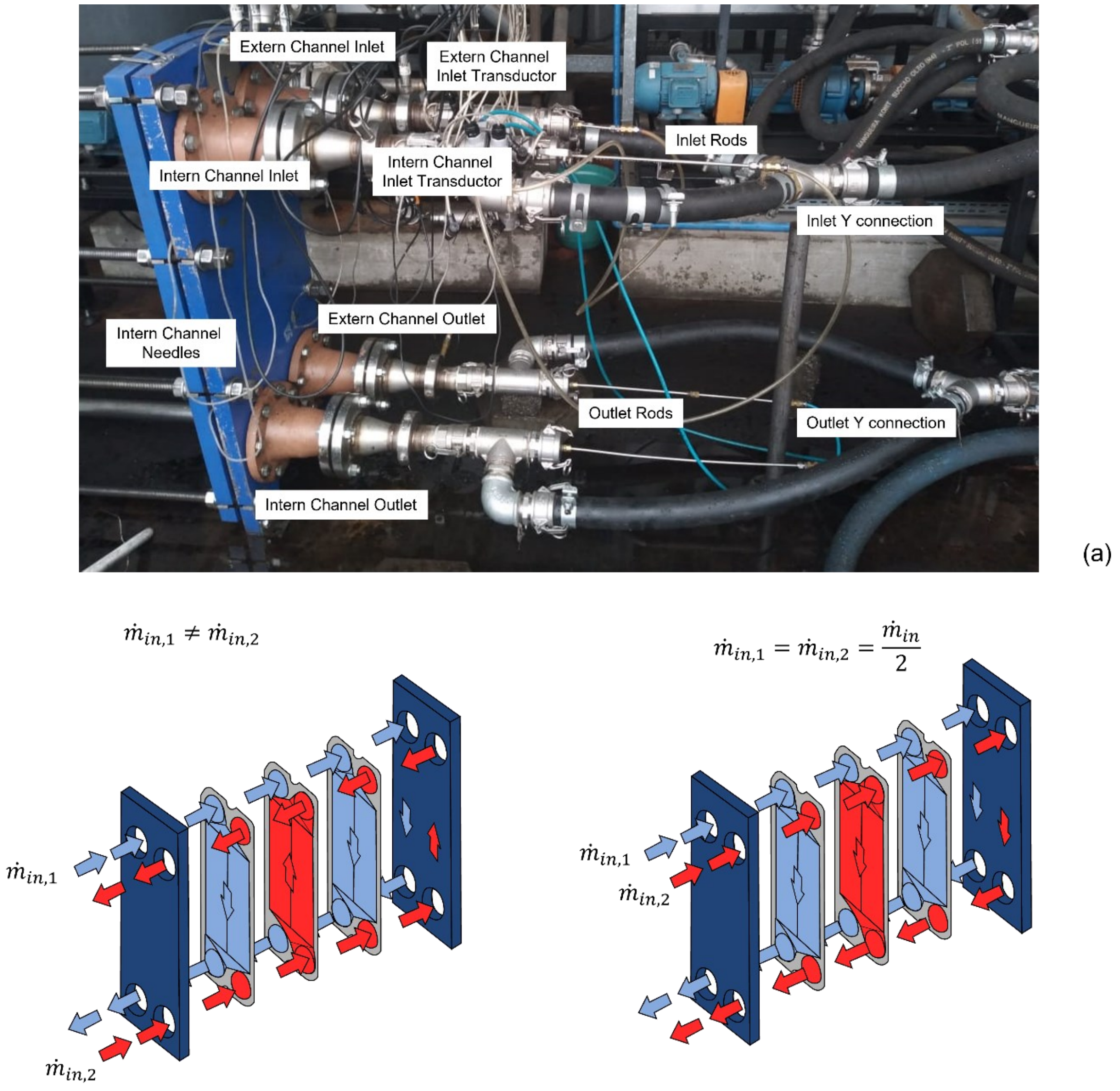

(a)

(b)

(c)

Source: Author (2023). a) Photograph of the GPHE connections and indications of the main points; b) Indication of flow in countercurrent configuration; c) Indication of the flow in the parallel configuration.

Figure 9 - Bench operation flowchart in countercurrent configuration

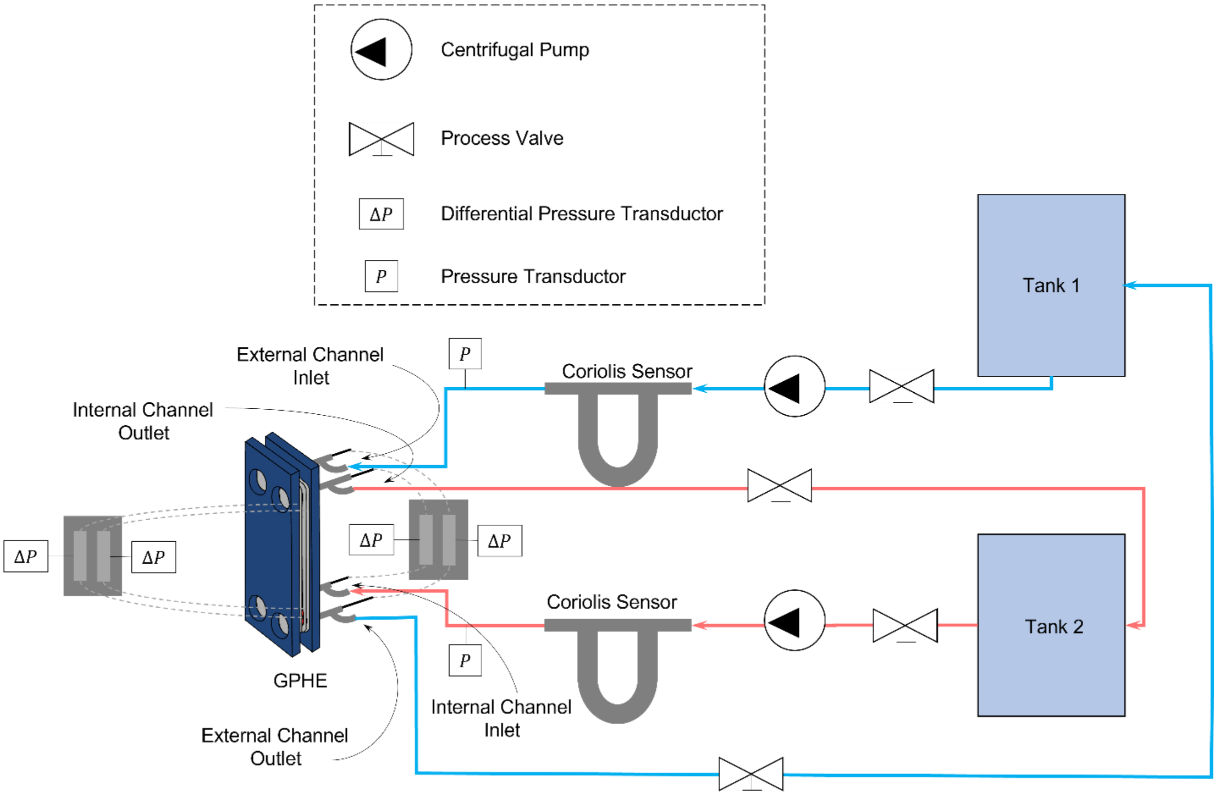

Source: Author (2023).

Figure 10 - Bench operation flowchart in parallel configuration

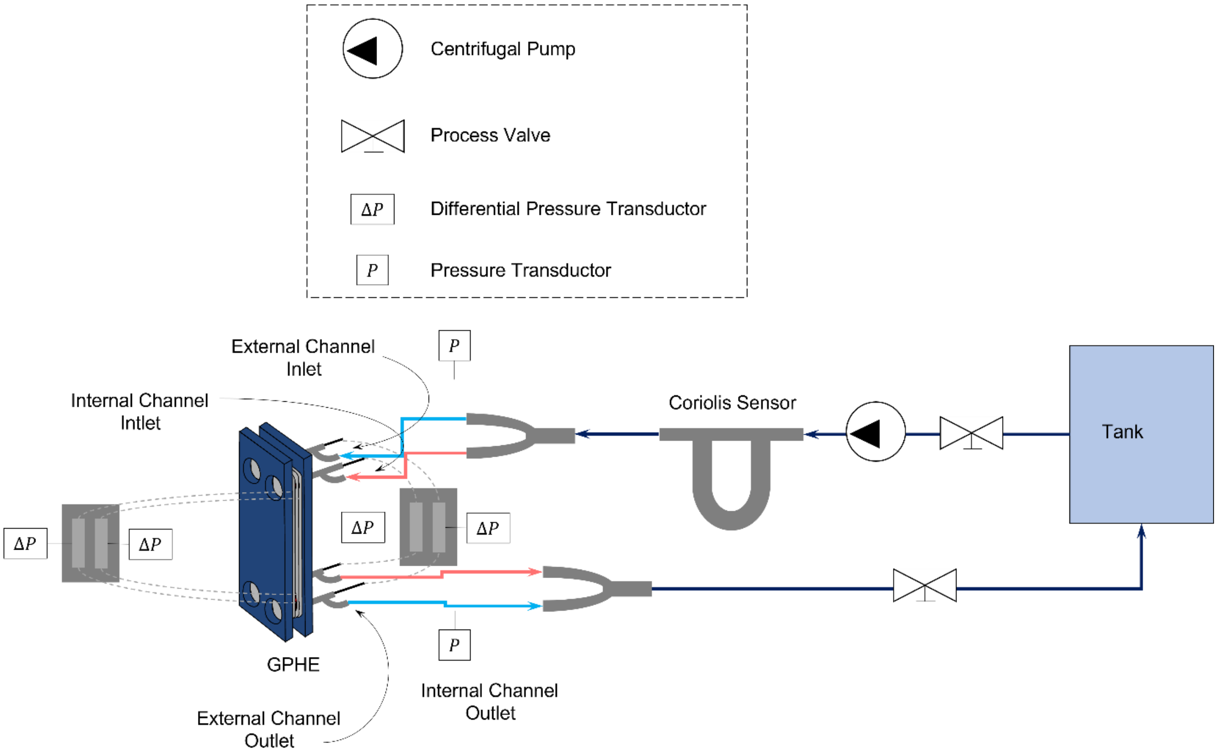

Source: Author (2023).

Table 1 - Instruments used in the hydrodynamic bench

Equipment	Model	Quantity
Frequency inversor	Siemens Sinamics V20	1
Coriolis sensor	Coriolis Emerson CMF200M	1
Absolute transducer	PX409-250GI-EH	2
Differential pressure transducer	PX409-050DWUI	2

Source: Author (2023).

For the countercurrent configuration (Figure 9), the valves are opened. Once the water in the tank is at a temperature between 25℃ and 27℃, the pumps are turned on. The Coriolis sensor registers the mass flow and the fluid is directed to the GPHE. The internal fluid flows upward through the device plates and returns to the water reservoir via piping. Meanwhile, an external branch fluid flows downward through an independent tank and piping, passes through the GPHE and returns to its respective tank.

In the parallel setup (Figure 10), the fluid is separated by a "Y" junction prior to its initial entry into the GPHE to uniformly allocate the flow in each branch. The flows then descend through the plates of the devices and finally pass through another "Y" connection at the end, reuniting the fluid that goes into the tank.

Also, differential pressure transducers register pressure information utilizing two methods: the first collects pressure drop data between nozzles by using rods situated in the center of each nozzle in each branch, amounting to four rods; the second method utilizes thin tubes, diameter of approximately 8 mm, connecting new transducers to needles installed at the inlet and outlet of the thermal exchange channel of the first plates of each branch. Such needles pass through the gasket and their tips collect the fluid located on the periphery of the transition zone between distribution and thermal exchange. The placement of each extension can be seen in Figure 11. It is important to note that the measurements for the external branch refer to the first pair of plates of this branch.

Figure 11 - Location of sensors

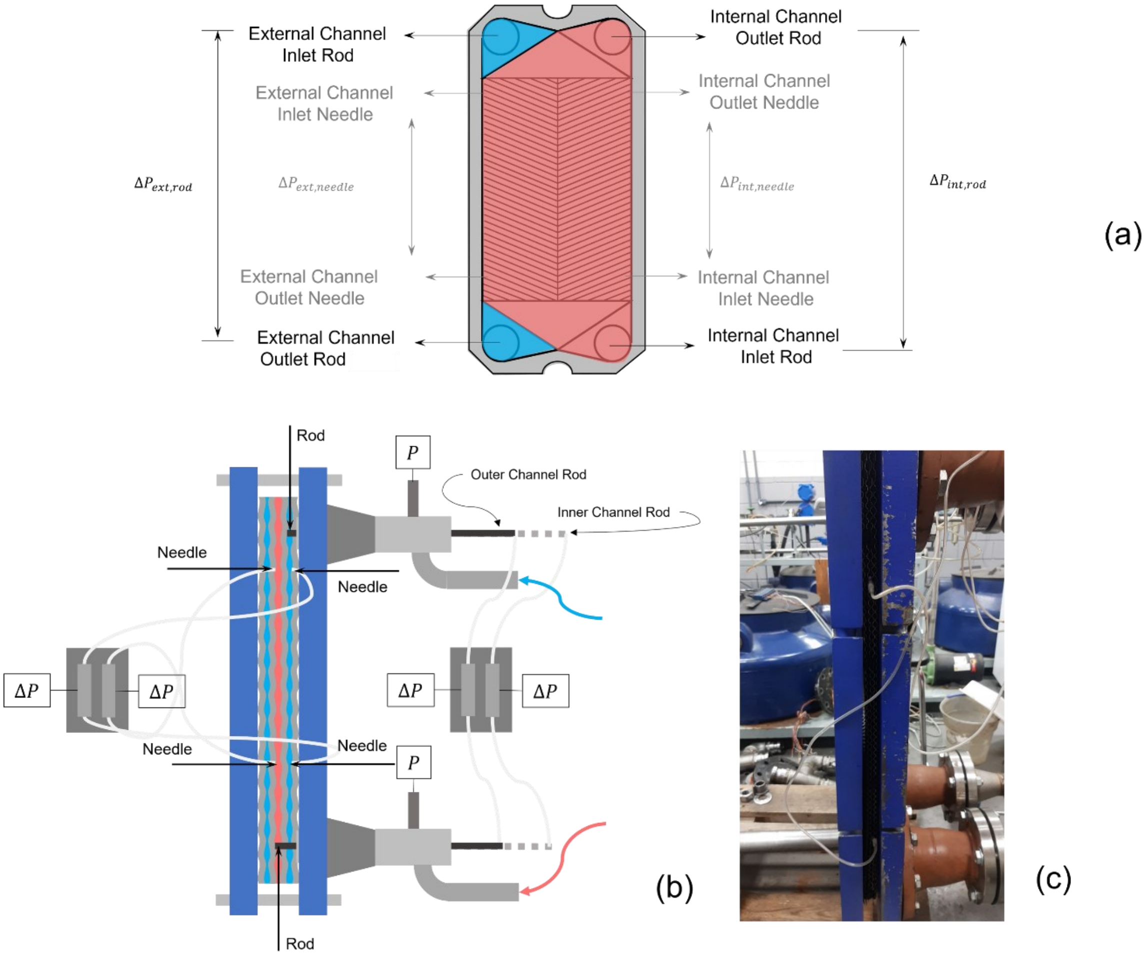

Source: Author (2023). a) Indication of sensor positioning and pressure drop measurements; b) Scheme with side view; c) Real image of the pack assembly.

The Reynolds number at the entrance of each branch is determined using Equation (8). Np is equal to 1 and 2 for the internal and external branches, respectively and ϕ = 1.2.

Table 2 provides the definitions of each studied case in the bench experiment. Water at room temperature was used as the working fluid to evaluate all cases. The input Reynolds range was determined by the operating range of each branch feeding pump, varying from approximately 11 Hz to 59 Hz. To ensure test repeatability, three tests were conducted for all cases.

Table 2 – Hydrodynamic experimental analysis cases

Case #	Configuration	$\dot{m}_{in,intern}$ [kg/s]	$\dot{m}_{in,extern}$ [kg/s]	ΔP_{in} [bar]
1	Parallel	0.45 a 2.85	0.45 a 2.85	$\Delta P_{in} = 0$
2	Countercurrent	0.26 a 1.77	3.44 a 2.40	$\Delta P_{in} \neq cte$
3	Countercurrent	3.94 a 4.05	0.51 a 2.39	$\Delta P_{in} \neq cte$
4	Countercurrent	0.46 a 1.75	0.83 a 2.40	$\Delta P_{in} = 0$
5	Countercurrent	0.86 a 1.87	0.77 a 2.17	$\Delta P_{in} = 0.5$
6	Countercurrent	1.13 a 2.00	0.76 a 1.95	$\Delta P_{in} = 1.0$
7	Countercurrent	1.24 a 2.07	0.52 a 1.76	$\Delta P_{in} = 1.5$
8	Countercurrent	1.46 a 2.14	0.51 a 1.59	$\Delta P_{in} = 2.0$
9	Countercurrent	0.20 a 1.67	1.31 a 2.69	$\Delta P_{in} = 0.5$
10	Countercurrent	0.21 a 1.39	1.76 a 2.80	$\Delta P_{in} = 1.0$
11	Countercurrent	0.345 a 1.18	2.27 a 3.00	$\Delta P_{in} = 1.5$
12	Countercurrent	0.346 a 1.00	2.62 a 3.19	$\Delta P_{in} = 2.0$

Source: Author (2023).

To help understand the results and input parameters, Figure 12 illustrates the constriction and expansion behaviors of the heat transfer channel region of the four-plate pack. It also defines the ΔP_{in} parameter. Figure 12-a shows the fluid inlet and outlet for each branch in the countercurrent configuration. In it, $P_{in,1}$ is the inlet pressure of the internal branch - shown in red in the figure - and $P_{in,2}$ is the inlet pressure of the external branch, shown in blue. ΔP_{in} is the difference between these inlet pressures and defines whether a loading condition is symmetrical ($\Delta P_{in} = 0$) or asymmetrical ($\Delta P_{in} \neq 0$). In the symmetric condition, both branches are pressurized with the same inlet pressure (it is understood that the internal pressure may vary from branch to branch depending on the number of passes of each branch) and there is no visible deformation in the heat exchange channel (Figure 12-b). In the asymmetric condition, one of the branches has a higher inlet pressure than the other, where the branch with the lower pressure is under constriction (Figure 12-c) and the branch with the higher pressure is under expansion (Figure 12-d).

The figure specifically shows the heat exchange channel, as this is the only region of the plate that receives loads (fluid pressure) on both sides over its entire area. The fluid inlet and outlet ports are unsupported (not in contact with fluid on both sides) due to the asymmetric geometry of the fluid volume, resulting in deformation behavior different from the approximately parabolic profile expected for the heat exchange channel. The same occurs in the fluid distribution galleries (both inlet and outlet) which, despite being in contact with the fluid on both sides of the plate, are affected by the sharp profile of the ports. From this information, it is possible to identify that cases 1 and 4 are considered symmetric, while cases 5 to 12 are asymmetric.

Figure 12 - Graphic indication of the expansion and constriction behaviors of the heat exchange channel of the pack

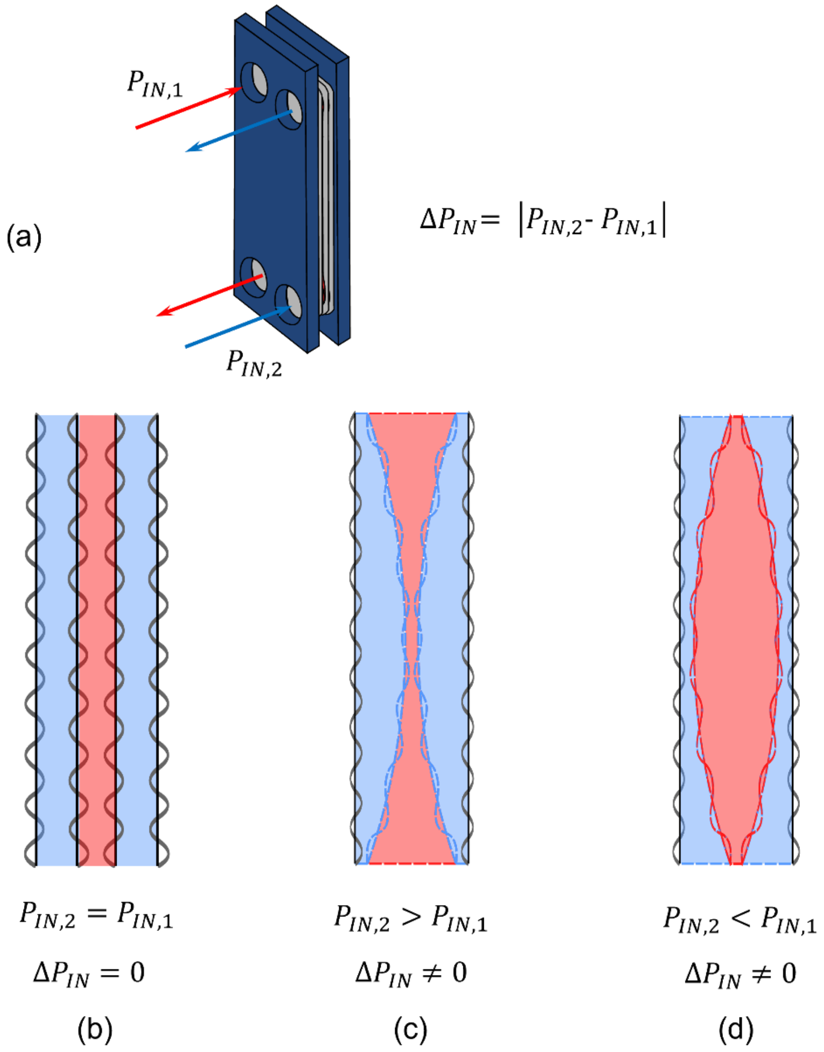

Source: Author (2023).

The first case involves the parallel setup, where the fluid in each branch originates from a single source and is divided using a Y connection to achieve equal inlet flows. This also results in equal inlet pressures. Cases 2 and 3 involve tests with varying ΔP_{in}. The test is conducted by constructing internal and external flow curves in parallel, beginning at the pump's maximum frequency and selecting one branch to remain constant. Following this measurement, the non-constant branch undergoes a frequency reduction of 5 Hz per data point collected, reaching the minimum limit of 11 Hz or as close to it as possible. Case 2 demonstrates the maximum frequency in the external branch pump and a variation in the internal branch frequency. In contrast, Case 3 shows the setting of the maximum frequency in the pump in the internal branch and a variation in the external branch. Table 2 highlights that the maximum pump flows differ between channels because of the variation in $\Delta P_{in} \neq 0$, which lowers the operating pressure limit established by pressure transducers in the external branch (and causes one curve having less points than the other, given the same frequency variation step). Since each point on the curve has an inlet pressure difference, ΔP_{in}, different from the others, cases 2 and 3 are defined as $\Delta P_{in} \neq cte$. It is important to highlight that in both cases only the branch frequency is kept constant, since the mass flow varies naturally in the heat exchanger due to the change in flow rate of the adjacent branch, that is, as the adjacent branch varies its flow rate. flow, the branch pressure varies, causing the plate to yield to the load of the branch that is most pressurized at the time. In this way, the adjacent branch is compressed when the "constant" branch is expanded, and vice versa, causing the flow to vary its speed until it reaches steady state and a new frequency input is inserted.

Case 4 simulates symmetric loads, with $\Delta P_{in} = 0$, in a countercurrent configuration. To achieve this condition, both branches receive frequency variation in the inlet pump, contrary to what happened in cases 2 and 3, which kept one of the pumps fixed. Both pumps are then set to their maximum frequency (59 Hz for the inner channel and 46.5 Hz for the outer channel) and are varied together to their minimum, always maintaining inlet pressure symmetry.

Cases 5 to 12 examine the response of the pack under the condition of a non-zero but constant ΔP_{in}. These cases comprise tests 5 to 8 wherein the pump of the internal branch receives a steady frequency reduction of 5 Hz, while the pump of the external branch varies to match the inlet pressure and attain the ΔP_{in} values of 0.5, 1.0, 1.5 and 2.0 bar. On the other hand, cases 9 through 12 indicate the opposite scenario, in which the external branch pump frequency is constantly varied and the internal branch pump frequency adjusts accordingly. Cases 5 through 8 describe the expansion of the internal branch, while cases 9 through 12 describe its constriction.

3.1.2 Structural tests

Tests to gather stress and strain data for GPHE were conducted on a hydrostatic bench, as explained in Martins et al (2022) and illustrated in Figure 13. The bench can generate loads of up to 20 MPa.

Figure 13 - Hydrostatic experimental bench setup: (a) rig and test section schematics, (b) setup photograph.

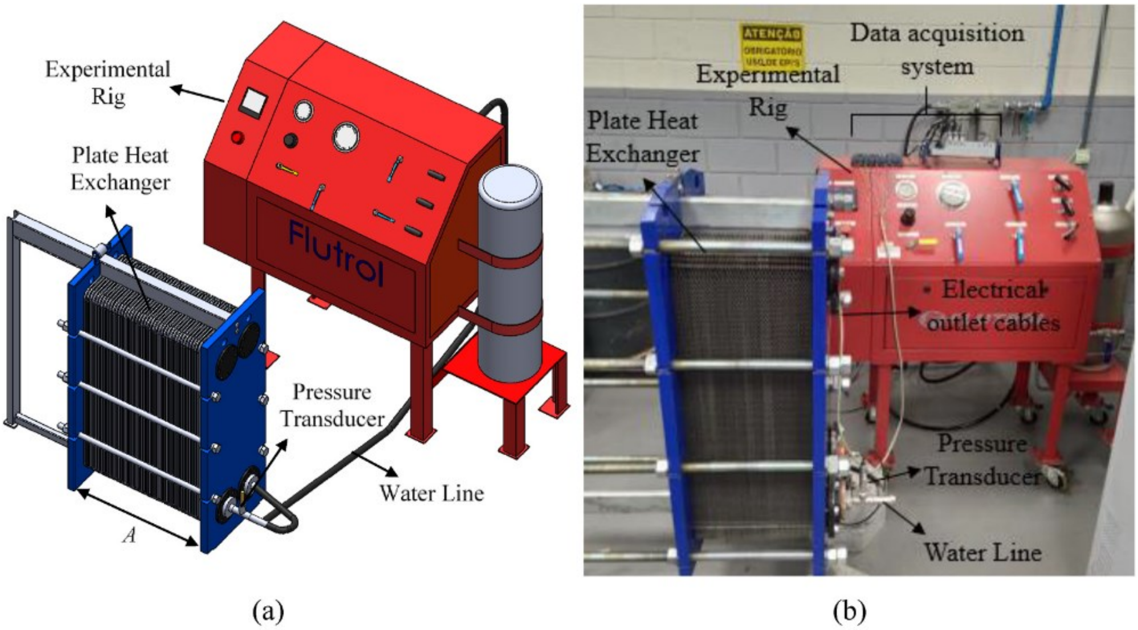

Source: Martins et al (2022).

Table 3 lists the instrumentation installed on the bench. Technical definitions and further details are available in the reference. The bench includes:

- A hydro-pneumatic pump is supplied by an air line at 7 bar, which pressurizes the water line to the desired operating pressure of the user;
- An absolute pressure transducer monitors the pressure supplied to the heat exchanger with a range of 0-5MPa and an uncertainty of approximately 0.5%.
- Globe and relief valves for fine adjustment of static pressure in the hydropneumatic pump;

- LVDT sensors (Linear Variable Differential Transformer) for measuring the deformation of the perimeter of the plates, namely widening and stretching.

Table 3 - Equipment used in the hydrostatic bench

Equipament	Model	Quantity
Hydro-pneumatic pump	Haskel ASF-35	1
Absolute pressure transducer	PX401 Series	1
LVTD sensor	Omega LD500-5	2

Source: Author (2023).

The bench works by filling the branch of interest with working fluid (a single one for the single loading condition, both for the double loading condition) and pressurizing this branch in order to achieve a uniform and homogeneous pressure profile, allowing the collection of stress and strain data (through LVTD sensors and strain gauges) in critical load situations. The bench also allows pressure cycling to analyze fatigue in the devices.

Data was acquired from an 88-plate pack, which had LVTD sensors mounted at six points on their perimeter to measure lateral deformation (WdX) and four points for longitudinal deformation (StX), as depicted in Figure 14. Each plate was individually measured with sensors placed at opposite ends to capture total displacement. Measuring points Wd1, Wd3, Wd5, St1 and St3 are symmetrical to measuring points Wd2, Wd4, Wd6, St2 and St4 respectively. Eleven pressurization cycles were examined with three sets of measurements taken for each.

Figure 14 - Strain measurement points in the experimental hydrostatic test

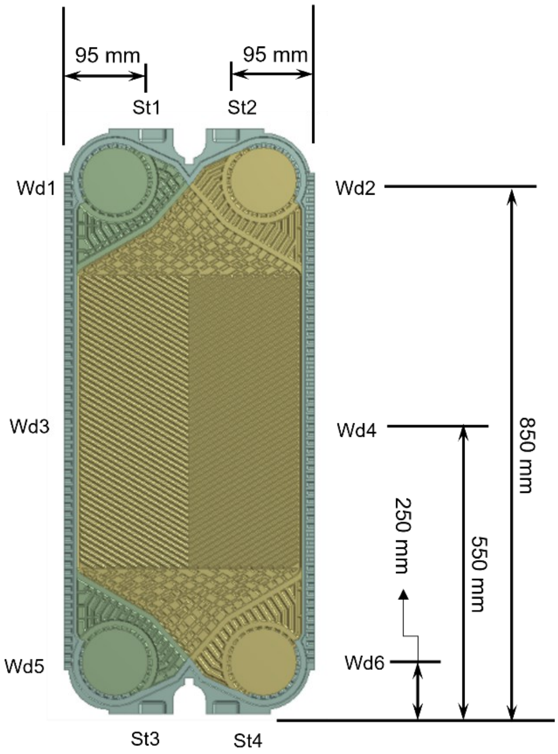

Source: Author (2023).

The analyzed GPHE solely comprised M10-type plates with a central “V” pattern and a Chevron angle of 60º to guarantee easy replicability in the numerical model. The testing included both the double symmetric loading condition, wich is the condition with identical loading applied on both sides of the plate, and the single loading condition, wich is the loading in only one of the sides of the plates. For further comparisons with the numerical results, only the double condition will be used.

The stages of testing, acquiring and processing data were carried out by partner researchers from the Thermal Fluid Flow (T2F) research group at the Federal University of Santa Catarina (UFSC) and made available through internal communication.

Since there are obstacles in numerically modeling such a massive pack, mainly due to computational cost, only the available measurements of the plate closest to the initial cover plate (plate number 10) were compared in the validation step, since the movement restriction conditions in these regions are closer to those used in the numerical model.

3.2 NUMERICAL METHODOLOGY

The development of this work will be based on the comparison of two approachs for the analysis of fluid-structural interactions to analyse the elastic deformation phenomena in GPHEs:

- Hydrostatic analysis: In this study, the extreme cases of load, displacement, and plate spacing are evaluated using uniform and maximum conditions to understand the critical behavior of the domains. There is no coupling between the domains;
- One-way hydrodynamic analysis: Domain coupling is performed manually and perturbations are isolated.

For this purpose, two different sets of geometries, meshes, and adapted boundary conditions will be applied to each relevant domain, namely the fluid and solid domains. This will be done with the development of two numerical models and an experimental setup applied to analyze the phenomenon and validation of the numerical model.

Figure 15 shows the rationale behind assembling the analysis cases. Both numerical methodologies employ the same geometry, consisting of plates and fluid volume.

Figure 15 - Flowchart for defining numerical analysis cases

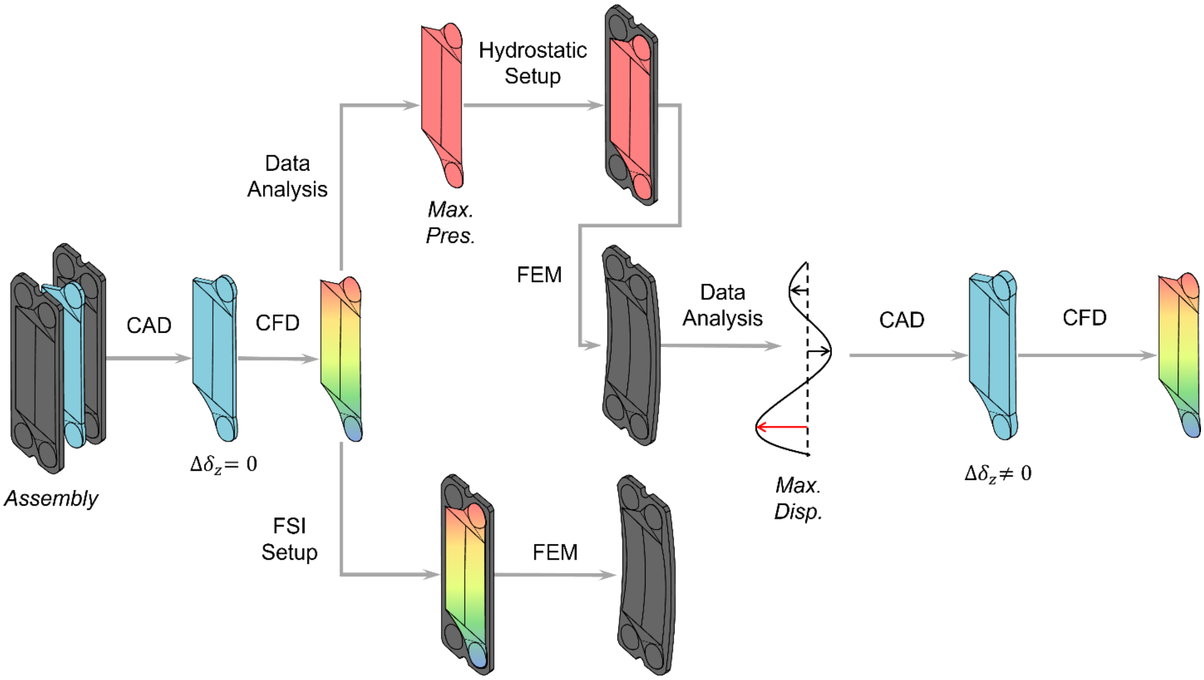

Source: Author (2023).

The objective of the study is to identify the limitations and possible applications of the two numerical methodologies, in order to facilitate the identification and study of elastic deformation phenomena (and other fluid-structural interactions) found in GPHEs.

3.2.1 Geometries for numerical analysis

3.2.1.1 Solution domains

The heat exchanger contains numerous parts, subparts, and fasteners, making the modeling process complex. Therefore, simplifications were implemented to model the solution domains addressed in this study.

The heat exchanger tops and all fasteners are modeled as being crimped onto the outer plates, while the racks are modeled as having movement restriction conditions. Sealing gaskets are replaced by elastic support conditions and initial sealing pressure, which will be elaborated further in the text.

The plate pack analysis is restricted to four corrugated plates to minimize the computational cost. Only the inner two plates are evaluated due to the symmetry of their geometry. Modeling only half of the heat exchanger to increase the number of plates was not considered as the loading condition is not symmetrical.

Such reduction of the plate count is solely feasible when there is homogeneous flow working on the apparatus, meaning that there are no distribution abnormalities throughout the pack's length. Figure 16 indicates the part of the metholodgy fluxograma in wich the CAD Generation for the original solution domains is inserted.

Figure 16 - Step indication: CAD generation

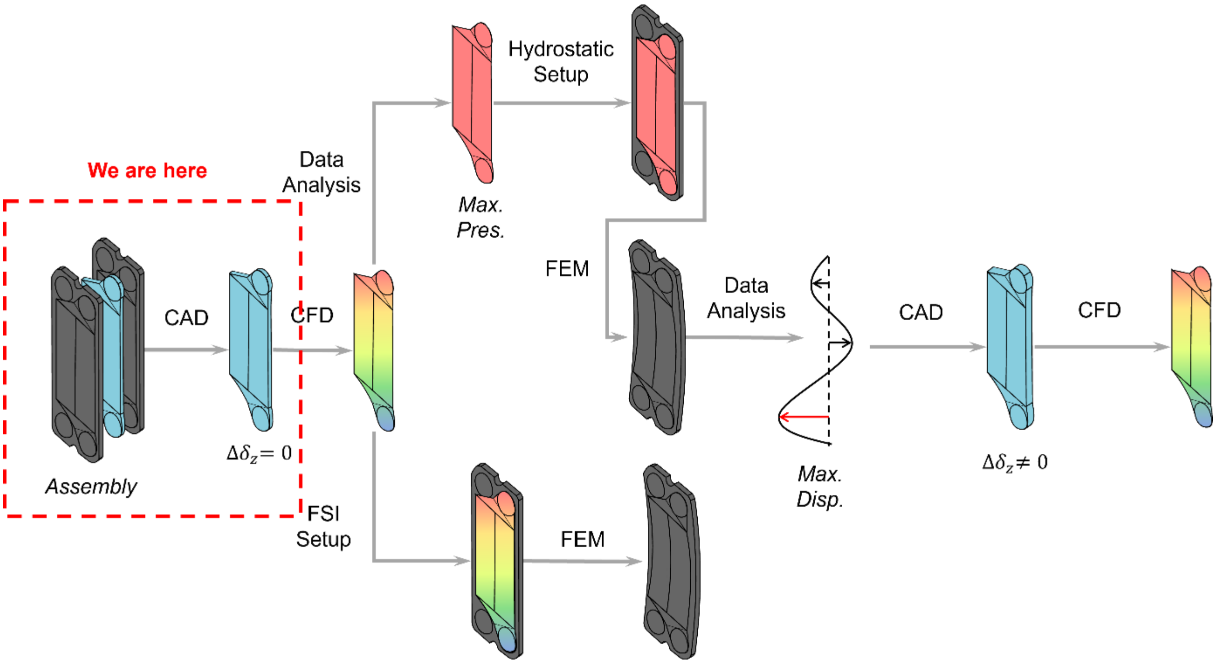

Source: Author (2023).

Figure 17 illustrates the arrangement of plates and fluid domains. The solid domain consists of a set of four corrugated plates. The negative volume created by pairs of plates 2-3 (defined as the internal fluid domain), as well as plates 1-2 and 3-4 (defined as the external fluid domains, united in a single body), define the fluid volumes. The flow perimeters are delimited by the gaskets. As for the coordinate axis, the horizontal axis of the pack is defined as the X direction, the vertical axis of the pack is defined as the Y direction, and the axis normal to the pack (coming out of the sheet) is defined as the Z direction. These directions define the widening, stretching, and separation directional displacements, respectively.

Figure 17 - Definition of the nomenclature and location of the main elements of the pack.

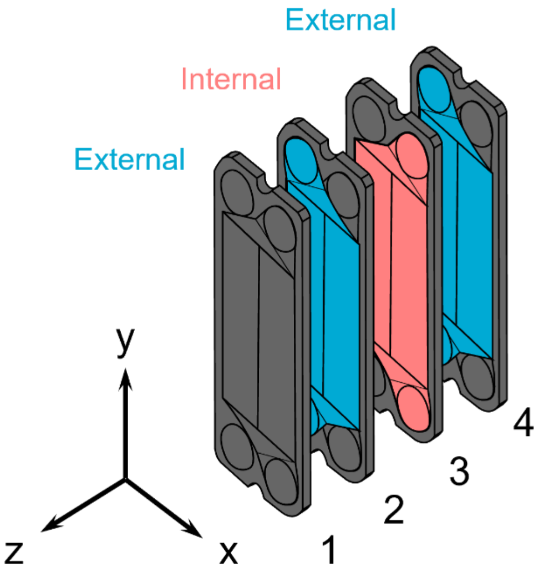

Source: Author (2023).

Each individual fluid domain, whether internal or external, is referred to as a branch. Within each branch are passes, and in this particular case, the internal branch contains one pass while the external branch contains two passes. The following terms have been established for future analysis:

- The first pass of the external branch (between plates 1 and 2) is defined as Fluid 1 or F1;
- The single pass of the internal branch (between plates 2 and 3) is defined as Fluid 2 or F2;
- The second pass of the external branch (between plates 3 and 4) is defined as Fluid 3 or F3.

Figure 18 depicts the solid and fluid domains used in numerical analysis. The geometries were originally acquired through 3D scanning, being treated and assembled with the modeler Ansys Design Modeler.

Figure 18 - Simulation domains

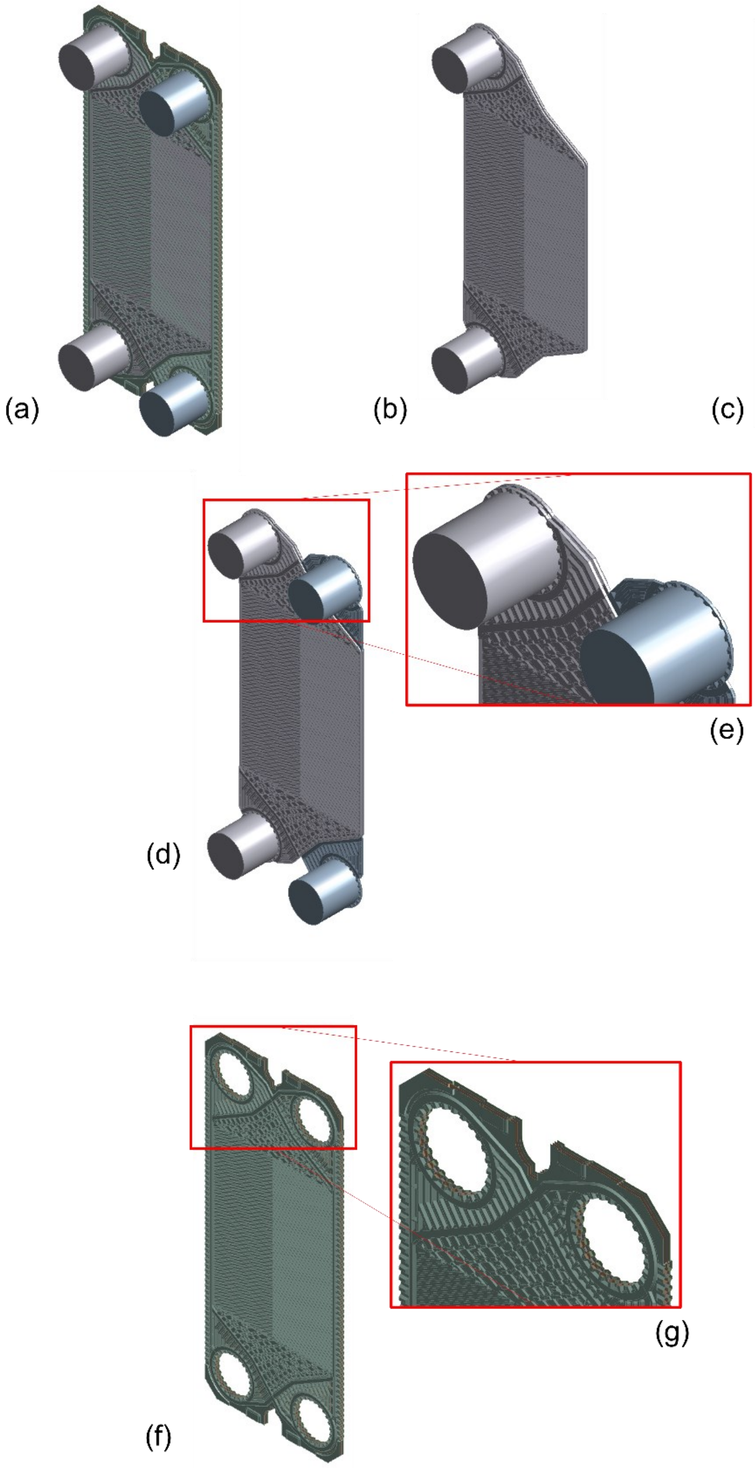

Source: Author (2023). a) Assembled pack; b) Extern fluid domain; c) Intern fluid domain; d) Arrangement of fluid domains; e) Detail of arrangement of fluid domains; f) Pack of plates; g) Detail of pack of plates.

The dimensions of the corrugated plate are presented in Figure 19. The dimensions of the internal fluid domain are displayed in Figure 20, and the dimensions of the external fluid domain can be found in Figure 21. A slight spacing between the plates was necessary during fluid volume generation due to the limitations of the geometry modeler. In actual assembly scenarios, the plates are tightened until they make contact due to the possibility of settling or minor deformation in the metallic material. It is, therefore, crucial to note that there exists a separation $\delta_{z,0}$ in each pair of plates, defined from the distance between the central planes of each plate, with origin defined in their respective centroids.

Figure 19 - Solid domain dimensions

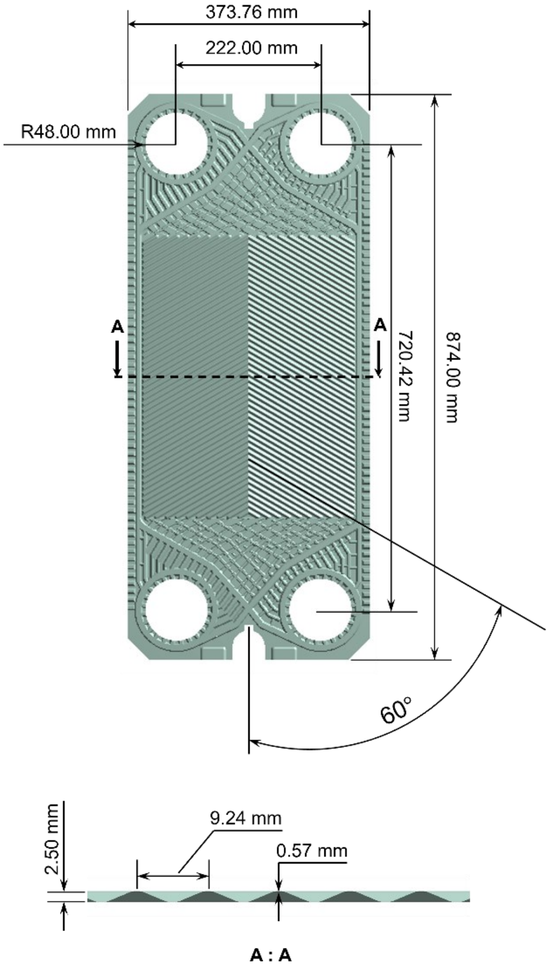

Souce: Author (2023).

Figure 20 - Dimensions of the internal fluid domain

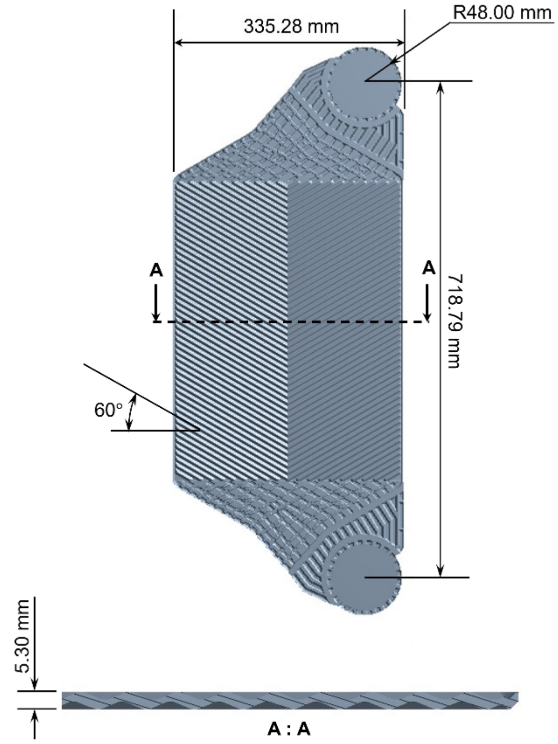

Source: Author (2023). Dimensions in mm

Figure 21 - Dimensions of the external fluid domain

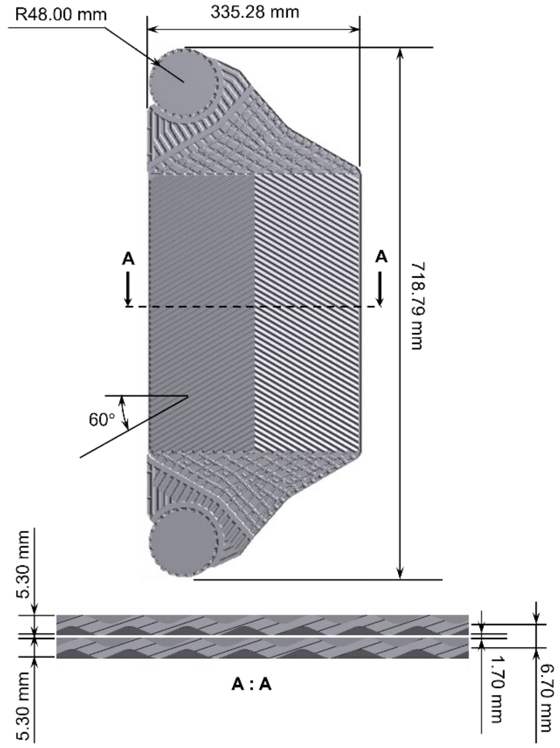

Source: Author (2023). Dimensions in mm

The fluid domain's thickness is determined by the plates' spacing, which is initially 0.3 mm and will be considered for future analysis. Both approaches share a similar starting configuration, but they differ as iterations occur.

3.2.2 Hydrostatic analysis

Hydrostatic analysis is the first method used in this study. It involves exciting a solid domain with a uniform pressure, regardless of whether or not it originates in a fluid domain.

For the hydrostatic analysis, the branches that were originally filled with water flow are now modeled as uniform and homogeneous pressure. This pressure is defined as the inlet pressure of the fluid. This simplification assumes the critical load condition, as there is a drop in pressure between the inlet and outlet of the plate.

3.2.2.1 Hydrostatic structural analysis

The objective of this structural analysis method is to evaluate stress and displacement distributions, as described by Donati et al. (2021). The study concluded that the hydrostatic approach is sufficient for estimating displacements in PSHE-type heat exchangers with low Reynolds values. It is expected that this approach will yield similar results when extrapolated to GPHE plates.

The authors state that the method is not advisable for stress assessment because the uniform load does not correspond to the actual scenario (wherein there is a pressure decrease along the plate length) and overestimates the maximum stress values. However, estimating displacements is relevant for the implementation of approximate fluid-structural interaction techniques like fluid dynamic analysis with uniform spacing.

3.2.2.2 Hydrodynamic analysis with uniform spacing

Once the maximum displacement values are determined in the structural analysis, it is possible to assess the behavior of deformed flow approximately by assigning these values as uniform spacing (the spacing is applied between the central planes defined by each centroid of each plate). Figure 22 illustrates the methodology . The figure on the left represents the displacement curve found after the FEM analysis, indicating the point of maximum displacement on the plate. Each maximum displacement value will create a fresh fluid domain with a different thickness compared to the original one. This methodology demonstrates that uniform spacing equivalent to the maximum spacing imitates an extreme flow scenario, as well as uniform pressure in the structural analysis.

Figure 22 - Schematic of uniform spacing methodology

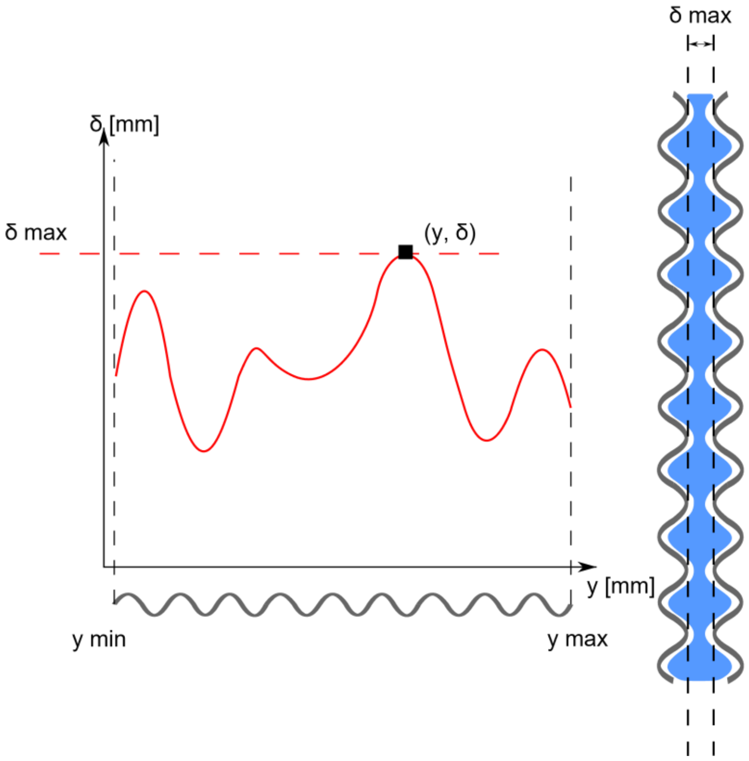

Source: Author (2023).

3.2.3 Hydrodynamic analysis

In the actual implementation of GPHEs, the phenomena are not separated as previously assumed. Consequently, the hydrostatic analysis serves as a basis for investigating the phenomenon of fluid-structural interaction.

For the evaluation of this coupling, two main methodologies can be employed: One-way, which examines the interaction by isolating the loads and manually feeding the system; and Two-ways, which concurrently analyzes both loads. This work will exclusively address the One-way methodology.

3.2.3.1 FSI one-way

Figure 23-a illustrates the flowchart of the FSI One-way approach for a pair of plates. In this study, 4 plates will be used.

1. Initially, the domain is undeformed, followed by the development of CFD analysis that generates velocity and pressure fields.
2. The resulting pressure distribution from the CFD analysis is then applied as a load in the solid domain.
3. Structural analysis is then developed, which generates stress and displacement fields. The displacement field indicates a deformed geometry with respect to the initial solid domain.
4. Such distorted geometry, when packed together, creates a negatively deformed volume in comparison to the original fluid domain. A new CFD analysis is developed;
5. New pressure and velocity fields are found.

This study will address the analysis until the fulfillment of item 3. Figure 23-b depicts the disparity between the thickness δ_i, denoting the initial fluid domain, and the thickness δ_o, relating to the deformed fluid domain.

Figure 23 - One-way fluid-structural interaction methodology

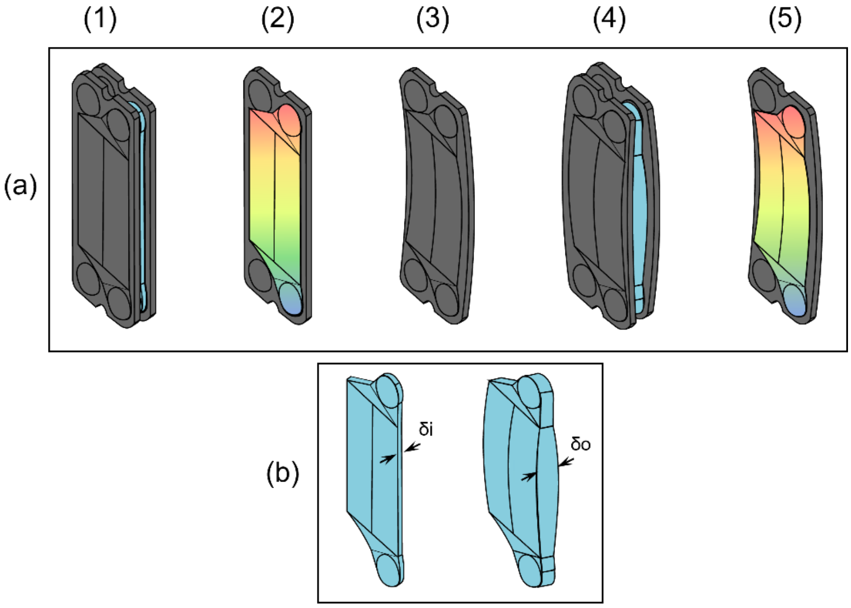

Source: Author (2023). a) Step-by-step of the One-way FSI methodology; b) Difference between the undeformed CFD geometry and the CFD geometry created by the deformation of the plates.

The One-way method is capable of multiple iterations. This step-by-step process allows for evaluating stress and strain states of the solid, as well as fluid velocity and pressure distributions at any point in the system feedback. The methodology is developed in sequential steps, requiring operator intervention to fulfill each coupling. However, it's noteworthy that there is a requirement for intermediate geometry treatment to identify the deformed fluid volume. The aforementioned process must be repeated for each assessed initial flow rate.

3.2.4 Numerical methods

Two separate techniques will be utilized to solve structural and fluid dynamics issues numerically: the finite element method and the finite volume method, respectively. Table 4 summarizes the software employed in this study at each stage for both approaches.

Table 4 – Applied softwares for numerical analysis

Methodology	Step	Software
Hydrostatic Analysis, FSI One-way Analysis	CAD	Ansys Design Modeler
	Mesh	Ansys Meshing
	CFD	Ansys CFX
	FEM	Ansys Mechanical APDL

Source: Author (2023).

3.2.4.1 Finite Volume Method (FVM)

The study employs the finite volume method (FVM) of Computational Fluid Dynamics (CFD). FVM linearizes conservation equations by dividing the domain into infinitesimal volumes and applying balance equations to their boundaries. This study addresses the conservation of mass and momentum, denoted as Equation (15) and Equation (16), respectively, for a newtonian fluid.

$$\frac{\partial \mathrm{\rho}}{\partial \mathrm{t}} + \frac{\partial}{\partial \mathrm{x_j}}\left(\mathrm{\rho u_j}\right) = 0 \qquad (15)$$

$$\frac{\partial}{\partial \mathrm{x}_{i}}\left(\mathrm{\rho u_i}\right) + \frac{\partial}{\partial \mathrm{x_j}}\left(\mathrm{\rho u_j u_i}\right) = \frac{\partial \mathrm{P_i}}{\partial \mathrm{x_i}} + \frac{\partial}{\partial \mathrm{x_i}}\left(\mathrm{\mu}\frac{\partial \mathrm{u_i}}{\partial \mathrm{x_j}}\right) \qquad (16)$$

For information regarding the method's construction, refer to Appendix A and the literature (MALISKA, 2017; VERSTEEG; MALALASEKERA, 2007; PATANKAR, 1980; ANDERSON, 1995). Table 5 includes all pertinent simplifying assumptions and finite volume analysis definitions, encompassing the advection method, turbulence, and solution regime.

Table 5 - Simplifying hypothesis and models used in the finite volume method

Condition	**Hypothesis**
Buoyancy	g_y = -9.81 m/s²
Compressibility	$\frac{d\rho}{dx} = \frac{d\rho}{dy} = \frac{d\rho}{dz} = \frac{d\rho}{dt} = 0$
Solution Regime	$\frac{d\phi}{dt} = 0$
Advection	High Resolution
Turbulence Model	$k - \varepsilon$ standard

Source: Author (2023).

The buoyant fluid condition signifies the impact of buoyancy within a solid-fluid system, with clear definitions of the direction and magnitude of gravity's effect. Compressibility measures the fluid's density change; however, as this fluid is deemed incompressible, there is no alteration in density. The solution regime is steady state, meaning the variables of interest remain unchanged over time, while the chosen advection scheme is the High-Resolution scheme for solving the discrete conservation equations' advective terms.

The $k - \varepsilon$ standard turbulence model was selected due to the higher computational cost required for the $k - \omega$ SST model. The deviations between the two models for this application can be found in the literature (TASCHECK et al.; 2022). The geometry is highly complex, and the number of interfaces between domains is extensive, resulting in a high computational cost. Finally, this study evaluates only the mechanical loads (derived from the flow’s pressure fields) on the device and does not address heat transfer in the system. As a result, temperature variations are not taken into consideration. The analysis fluid was water and Table 4 contains the physical properties of the fluid required to solve Equations 26 and 27 using the finite volume method.

Table 6 - Physical properties of water at 1 atm and 25ºC

Property	**Value**
Density (ρ_{H_2O})	997.1 kg/m³
Absolute Viscosity (μ_{H_2O})	8.905x10^{-4} [kg/ms]

Souce: Author (2023).

Table 7 presents all boundary conditions applied in the fluid domain. The surfaces listed in the table coincide with those indicated in Figure 24. As depicted in the figure, the fluid domain comprises one inlet and outlet only. The inlet condition for the domain is defined as prescribed flow, outlined for each case. On the domain walls, the no-slip condition is applied, which establishes the velocity of the fluid layer closest to a solid surface as zero. Additionally, the domain output condition considers the relative static pressure as the same as the ambient pressure, defined as 1 atm.

Table 7 - Boundary conditions of the finite volume method

Condition Nature	**Condition Type/Value**	**Applied Surfaces**
Inlet	Prescribed mass flow rate $(1.0\frac{kg}{s} \leq \dot{m}_{in} \leq 4.0\frac{kg}{s})$	Inlet
Outlet	Relative Static Pressure $(P_{domain} - P_{amb} = 0Pa)$	Outlet
Wall	No Slip	Wall (All remaining surfaces)
Turbulence Intensity	5%	Inlet

Source: Author (2023)

Figure 24 indicates the surfaces defined as inlet, outlet and wall for each of the fluid domains, as well as the definition of the flow direction for both branches. It is important to highlight that the external branch is made up of two passes, but the fluid inlet is the same for both. The case studied in this methodology was defined as countercurrent, as shown in the last figure.

Figure 24 - Boundary surfaces and definition of flow direction.

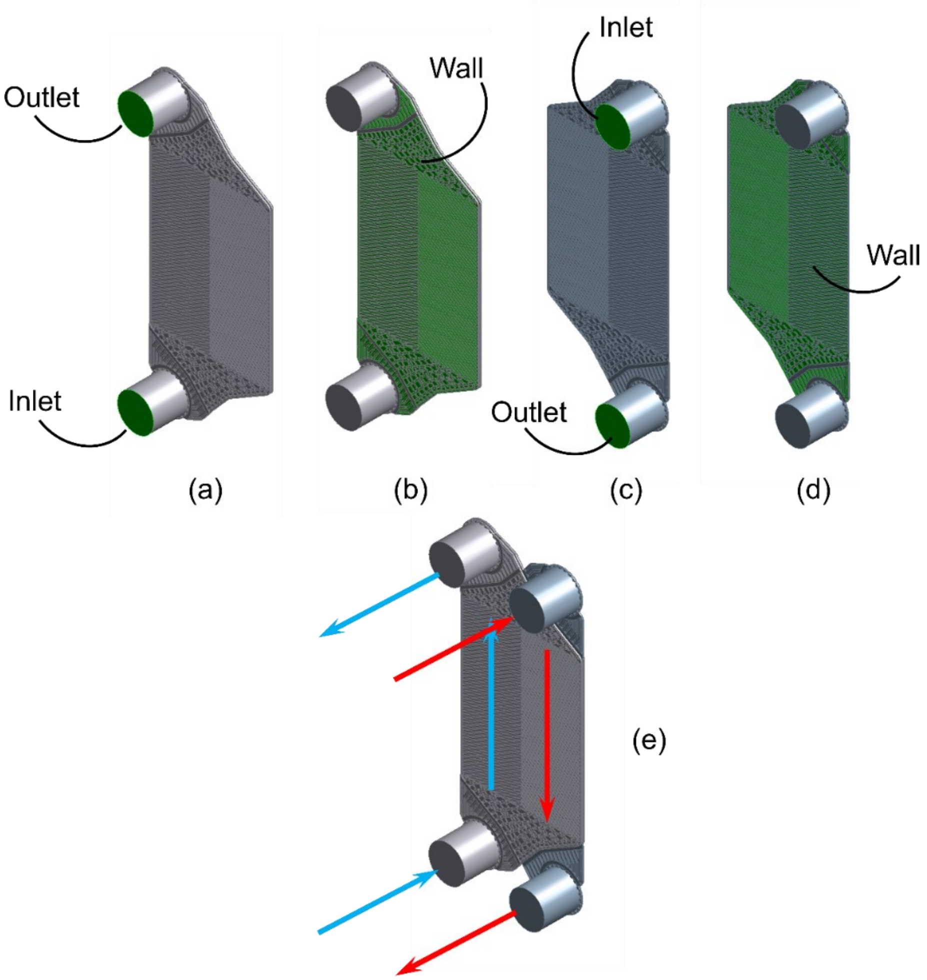

Source: Author (2023). a) External fluid inlet and outlet surfaces; b) External fluid wall surfaces; c) Internal fluid inlet and outlet surfaces; d) Internal fluid wall surfaces; e) Direction of fluid flow

3.2.4.2 Finite Element Method (FEM)

The finite element method (FEM) is founded on discretizing the solid domain to obtain stress and displacement results for the entire domain, from equations (17) and (18), rewritten below, which represent Hooke's Law generalized for a material with homogeneous properties. Subsequent to discretization, the FEM's objective is to solve a system of linear equations of order NxN, where N is the number of nodes in the discretization.

$$\varepsilon_i = \frac{\sigma_i}{E} - \frac{\nu}{E}\left(\sigma_j + \sigma_k\right) = \frac{1}{E}\left[\sigma_i - \nu\left(\sigma_j + \sigma_k\right)\right] \tag{17}$$

$$\gamma_{ij} = \frac{\tau_{ij}}{G}; \gamma_{jk} = \frac{\tau_{jk}}{G}; \gamma_{ik} = \frac{\tau_{ik}}{G} \tag{18}$$

For details on method construction, please see Appendix A and the literature (COOK, 1995; ALVES FILHO, 2000). This analysis employs stainless steel 316L as the material. Table 8 contains the mechanical properties essential for resolving the FEM. The indicated yield stress representes the minimum yield stress of the material, taking into consideration a undeformed sheet of metal as described in the ASME standard. Martins et al. (2022) define yield stress values equivalent to approximately 370 MPa for plates already formed from the same material.

Table 8 - Mechanical properties for 316L stainless steel.

Property	**Value**
Density (ρ_{316L})	8.00 g/cm³
Young's Modulus (E_{316L})	195.00 GPa
Poisson's Coefficient (ν_{316L})	0.31
Minimum Yield Stress (σ_{esc})	170 MPa

Source: Adapted from ASME Section II: Materials. Part D (2010)

In this study, the Finite Element Method (FEM) analyzes the problem with an elastic regime and isotropic mechanical Properties through static analysis. The hypothesis of small deformations is not applied in this analysis since the deflections can exceed the original value by up to 200% in certain plate zones. As a result, the applied finite element method recalculates the system's stiffness in each iteration.

The mechanical properties are analyzed in the linear-elastic regime, suggesting that the problem is primarily an elastic analysis problem. Any zones displaying plastic deformations must be evaluated qualitatively as they are extrapolated using the applied method. Therefore, the present problem always defines the stress as $0 \leq \sigma_{LIN} \leq \sigma_{ESC,316L}$; $\sigma_{PLAST} > \sigma_{ESC,316L}$, where $\sigma_{ESC,316L}$ represents the material's yield strength, σ_{LIN} indicates the stress within the linear-elastic regime, and σ_{PLAST} denotes the stress within the plastic regime.

Despite the absence of non-linearities in the mechanical properties of the material, in the problem modeled in this study, the contact conditions serve as a crucial source of non-linearity. This is due to the fact that the contact region between bodies changes as the load is applied, requiring the method to recalculate these regions in each iteration of the problem, regardless of whether the yield limit has been exceeded.

This condition is required as the load is applied incrementally to minimize the likelihood of diverging from the linear system solution method. Nevertheless, contact nonlinearities increase the method's complexity, implicating in the addition of implicit solution methods that simultaneously resolve current and future problem states. Additionally, nonlinear problems impede the use of the superposition principle.

Table 9 lists all boundary conditions applied in the solid domain for the hydrostatic analysis. Surfaces listed in the table correspond to those indicated in Figure 25.

Table 9 - Boundary conditions of the finite element method for hydrostatic analysis

Condition Nature	Condition Type	Applied Surfaces
Boundary	Fixed Support	All surfaces of plates 1 and 4
Boundary	Displacement Restriction: X = 0mm Y = 0mm Z = free	Surface in contact with the rack, on plates 1 to 4
Gasket	Elastic Support ($K\_eq = 5.4667$ [N/mm³])	Plate gasket channel 1 to 4
Sealing	Internal branch sealing pressure	Gasket channel on the Z- face of plate 2; Gasket channel on the Z+ face of plate 3
Sealing	External branch sealing pressure	Gasket channel on the Z- face of plate 1; Gasket channel on the Z+ face of plate 2; Gasket channel on the Z- face of plate 3; Gasket channel on the Z+ face of plate 4
Contact	Frictionless	Corrugated surfaces in contact of plates 1 and 2; Corrugated surfaces in contact of plates 2 and 3; Corrugated surfaces in contact of plates 3 and 4
Loading	Prescribed uniform pressure (Internal Flow)	Gasket-interior surfaces on the Z- face of plate 2; Gasket-interior surfaces on the Z+ face of plate 3

Source: Author (2023).

Figure 25 - Surfaces of the solid domain where the boundary conditions are applied.

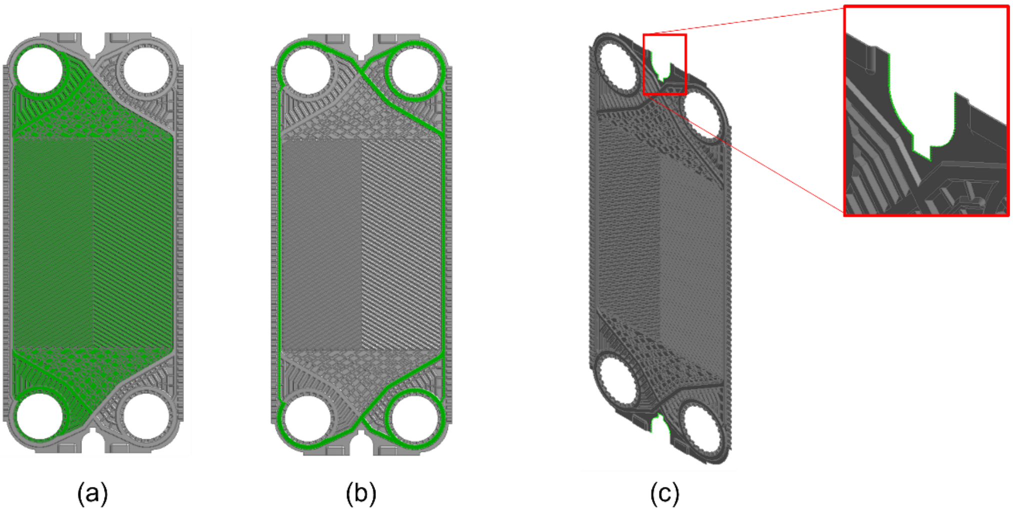

Source: Author (2023). a) Fluid-solid interface; b) Gasket channel; c) Rack support.

The boundary conditions for the FSI One-way method are comparable to those outlined in the previous table, with the exception of the application of loads. Unlike the hydrostatic method, these loads vary depending on the CFD's resulting pressure field. Additionally, the fluid pressure influences the sealing pressure, which is defined based on the maximum load pressure. This condition will be detailed in further sections.

As stated before, the heat exchanger cover plates are replaced to ensure crimping on the outer plates. In addition, contact conditions, elastic support, and sealing pressure were determined according to the studies from Nascimento (2013) and Peliccione et al. (2019).

3.2.4.2.1 Elastic support condition

Considering a gasket with a square section, as shown in Figure 26, with width l_g and height h_g, the stress variation $\Delta\sigma$ produced by the application of compressive force F is defined by Equation (19), where E_t is the Young's modulus of the gasket material in the section and $\Delta\varepsilon$ is the deformation of the section in the direction of the applied force.

Figure 26 - Main dimensions of the gasket

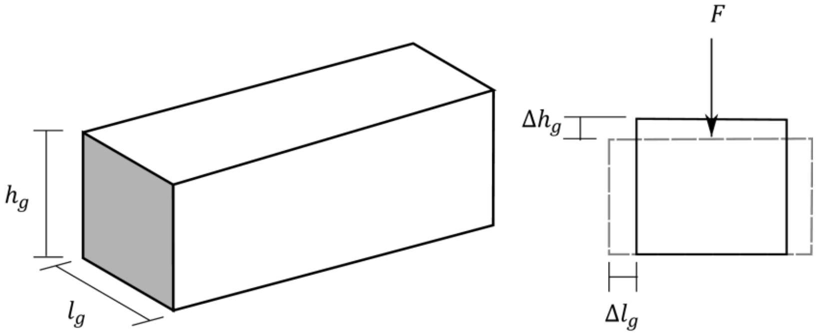

Source: Author (2023).

Equation (20) gives the deformation in geometric terms of the seal. Applying (20) to (19) gives equation (21).

$$\Delta\sigma = E_t \cdot \Delta\varepsilon \tag{19}$$

$$\Delta\varepsilon = \frac{\Delta h_g}{h_g} \tag{20}$$

$$\Delta\sigma = E_t \cdot \frac{\Delta h_g}{h_g} = \frac{E_t}{h_g} \cdot \Delta h_g \tag{21}$$

In an elastic base, the developed stress is proportional to the normal displacement to the surface of the base (NASCIMENTO, 2013), a condition that can be seen from Equation (22). The constant of proportionality is known as the elastic base's stiffness.

$$K_g = \frac{E_t}{h_g} \tag{22}$$

However, K_g represents the elastic base stiffness for a single gasket. To define a pack of four plates, it is necessary to determine the equivalent stiffness K_{eq}. The equivalent stiffness indicates, in this case, the stiffness that accounts for the interaction of all gaskets present in the model and is applied to each of the resistances independently (unlike the classic definition, which simply groups each stiffness into a single global one).

Figure 27 illustrates two plate systems modeled with a resistance model. The stiffness produced by the plate contacts is defined by K_p, whereas the gasket stiffness is defined by K_g. It is evident that, when the system on the left is excited with a displacement of δ, the nodes maintain a displacement value of $\delta_i = 4\delta$, as each node experiences two compressive and two tensile displacements.

Figure 27 - Equivalent system of resistances for modeling the elastic support condition

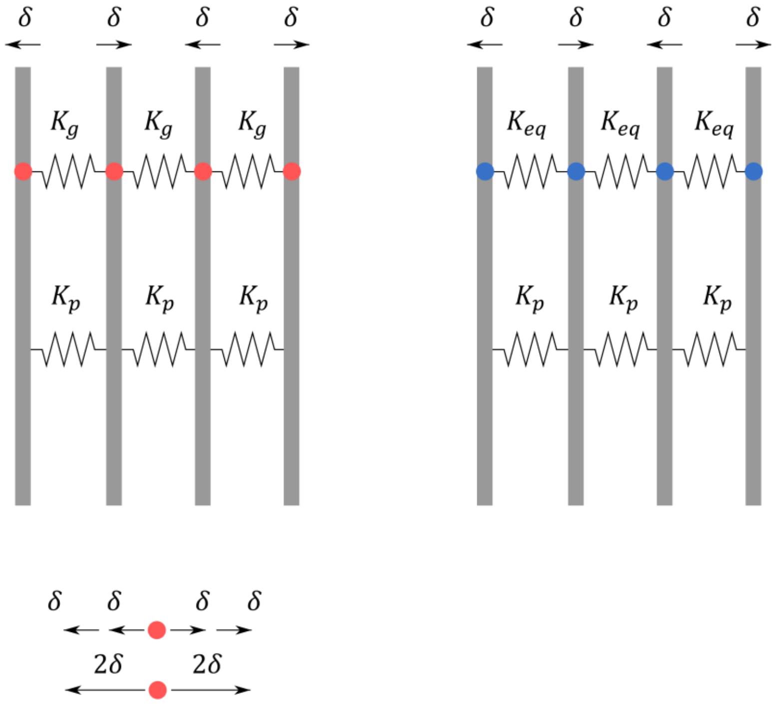

Source: Author (2023).

In the right system, the stiffness of the gasket, K_g, is substituted with an equivalent stiffness, K_{eq}. To confirm the equivalence of the two systems, the subsequent set of equations is established with F_o representing the force applied on the left system and F_{eq} signifying the force applied on the right system.

$$F_o = K_g \cdot 4\delta = 4K_g \cdot \delta$$

$$F_{eq} = K_{eq} \cdot \delta$$

$$F_o = F_{eq}$$

$$4K_g \cdot \delta = K_{eq} \cdot \delta$$

$$K_{eq} = 4K_g \qquad (23)$$

$$K_{eq} = 4\frac{E_t}{h_g} \qquad (24)$$

For an HNBR gasket, the Transverse Modulus of Elasticity value is E_t = 4.1 MPa (NISHIMURA; ODAGAWA; HAYASHI, 1997), and the height used in this work is h_g = 3 mm. Therefore:

$$K_{eq} = 4 \cdot \frac{E_t}{h_g} = 4 \cdot \frac{4.1 \times 10^6}{3 \times 10^{-3}} = 4 \cdot 1.3667 \times 10^9$$

$$K_{eq} = 5.4667 \times 10^9 \text{ [N/m³]}$$

The model presented here has been previously tested in the literature using sensitivity analysis (MARTINS et al., 2022).

3.2.4.2.2 Sealing pressure

Seal pressure is a compressive load that is applied before the stress load to seat the gasket in the groove. This load is applied in the gasket channel (see Figure 25-b) and has a variable value dependent on the internal pressure of the fluid (PELLICCIONE et al., 2019). The value is proportional to the $\frac{h_g}{l_g}$ ratio.

This definition conforms to the ASME (American Society of Mechanical Engineers) Sec. VIII D-1 (2010) standard, appendix , which outlines a minimum sealing pressure ($P_{sealing}$) as per Equation (25). P_{fluid} refers to the internal fluid pressure, and m represents an experimental factor specified by the gasket manufacturer, which is reliant on the type and material of the gasket. Pelliccione et al (2019) utilize a value of $m = 6$ for nitrile-based gaskets.

$$P_{sealing} = 2 \cdot m \cdot P_{fluid} \tag{25}$$

Table 10 displays sealing pressure values for all cases analyzed in the hydrostatic methodology, using the maximum pressure of each branch, denoted as P_{fluid}. In symmetrical cases, both sides of the plates receive the same sealing pressure, while in asymmetrical cases, the plates receive different pressures.

Table 10 - Sealing pressure values

P_{fluid}[MPa]	0.2	0.4	0.6
$P_{sealing}$ [MPa]	2.4	4.8	7.2

Source: Author (2023).

Since the FSI methodology involves utilizing variable pressure loads derived from the CFD simulation results, P_{fluid} refers to the maximum pressure in the relevant branch, resembling the critical loading condition. Furthermore, because the external branch has two fluid passes, a pressure difference between the front and bottom of the pack exists, necessitating distinct values of P_{fluid} for each pass.

3.2.4.2.3 Frictionless contact condition

Nascimento (2013) compares two contact conditions in his work: rough contact and frictionless contact. In rough contact, the plates have zero tangential movement, and contact stresses occur only when there is compression between them due to the non-linear contact. This restriction is justified as the contact condition prevents the plates from sliding during the operation of the heat exchanger. In the frictionless contact type, a non-linear contact, there are no restrictions on tangential movement between the plates.

The author observed a maximum variation of 1.5% between both models for residual compression in the evaluated region, with an average variation of 1.2%. Thus, it was concluded that determining the coefficient of friction between the plates is unnecessary, and that the frictionless contact model adequately models the problem.

3.2.5 Studied numerical cases

The CFD analysis begins by examining the internal and external volumes separately, under inlet conditions of $1.0\,kg/s \leq \dot{m}_{in} \leq 4.0\,kg/s$. The findings are assessed, and the maximum pressures of 2.0 bar, 4.0 bar, and 6.0 bar are used as the uniform loading in the hydrostatic method. After completing the FEM step, maximum displacement values along the Z axis are selected to generate new fluid volumes (internal only) and a second CFD step is performed under the same input conditions as in the first step.

In the FSI methodology, the pressure fields reaching a maximum value of 2 bar (which will correspond to different $\dot{m}_{in}$ values for the external branch compared to the internal one, as the external branch has two passes) will be utilized for the FEM setup. However, due to time constraints and computational costs, this method will solely be applied to the symmetrical case of 2 bar-2 bar.

Table 11 correlates the inlet mass flow values with the inlet Reynolds values for each branch. Such results make clear the difference in inlet conditions created by the number of passes for each branch. The mass flow values will be used when it is necessary to refer to the definitions of each case or simulation, as this quantity refers to the GPHE input condition and not each pass. However, Re values will be present in the analysis of results, to situate the data in relation to the flow transition bands and provide better comparison between branches.

Table 11 - Correlation between inlet massic flow and Reynolds number for undeformed internal and external branches in the numerical analysis

$\dot{m}_{in}$	$Re_{internal}$	$Re_{external}$
1.0 kg/s	4986.99	2493.50
1.5 kg/s	7480.49	3740.25
2.0 kg/s	9973.99	4986.99
2.5 kg/s	12467.48	6233.74
3.0 kg/s	14960.98	7480.49
3.5 kg/s	17454.48	8727.24
4.0 kg/s	19947.97	9973.99

Source: Author (2023).

3.2.6 Mesh and analysis parameters

3.2.6.1 Hardware definition

Three different computers were used for the development of this work. Table 12 compiles the main configurations of each one of them.

Table 12 - Utilized hardware identification

Machine ID	Processor	RAM
Dell Cluster	Intel® Xeon® CPU E5-2650 v4	128.0GB
Dell Workstations	Intel® Core™ i7-9700 CPU	64.0GB

Source: Author (2023).

The Dell Cluster was used for the calculation of all FEM steps, as well as for the mesh independence analysis and the CFD of the external fluid. The Dell Workstation was used for CFD calculation of the internal fluid, setup configuration, data processing, and analysis, generation of simple geometries, and processing of deformed geometries.

3.2.6.2 Solution meshes

Appendix B discusses in detail the definition of the solution meshes for both numerical methods in each of the geometries analyzed in this work, both the undeformed originals shown in section 3.2.1 and the new geometries generated by the numerical methods themselves amid the methodology of analysis. Also, in this appendix is the analysis of mesh independence for each of these geometries, using physical parameters and mesh quality parameters relevant to the work for monitoring independence.

3.2.6.3 Convergence criteria

The convergence criteria chosen for the CFD solution was 1.0×10^{-4} in the maximum value of the residuals, with a maximum value of iterations of 1000. The convergence criteria are fulfilled when the difference between the values of the last two iterations of each of the equations of the system reaches such a value. All developed simulations converged before the maximum of iterations fulfilling one of the following situations: the maximum residual value was reached or the convergence curves reached periodic behavior for at least 200 iterations.

Since this is a problem of nonlinear contacts, the solution of the FEM system of equations is done in an iterative and weighted manner, based on the Newton-Raphson method with a convergence criteria of approximately 0.5 %.

If the load used in the problem is too abrupt, the solution can generate bisections. To converge satisfactorily, the software divides that load in half, attenuating the slope of the curve. Each time the solution encounters a bisection, the software then decreases the initial force and adds smaller increments between substeps. The step control parameters used were initial timestep equal to 0.01s, a minimum timestep of 0.0001s, and a maximum timestep of 0.01s.

4 RESULTS AND DISCUSSION

4.1 EXPERIMENTAL RESULTS

4.1.1 Hydrodynamic results

Figure 28 shows the results for case 1, the only case in which the bench is defined in parallel flow configuration. The pressure drop values measured by the needle and the rod show variations from 0.29 bar to 0.44 bar for the internal branch, while the external branch indicated a variation from 0.26 bar to 0.29 bar. This variation between measurements indicates the pressure drop present in the region comprised by the distribution gallery and the fluid inlet nozzle in each branch. The variation of measurements between branches indicates that, even under the condition of parallel flow and symmetrical loading, the branches behave differently, mainly because the tightening of the pack were unsufficient to prevent the plates from moving.

Figure 28 - Results of hydrodynamic bench tests for parallel flow configuration in two inlet pressure ratio conditions

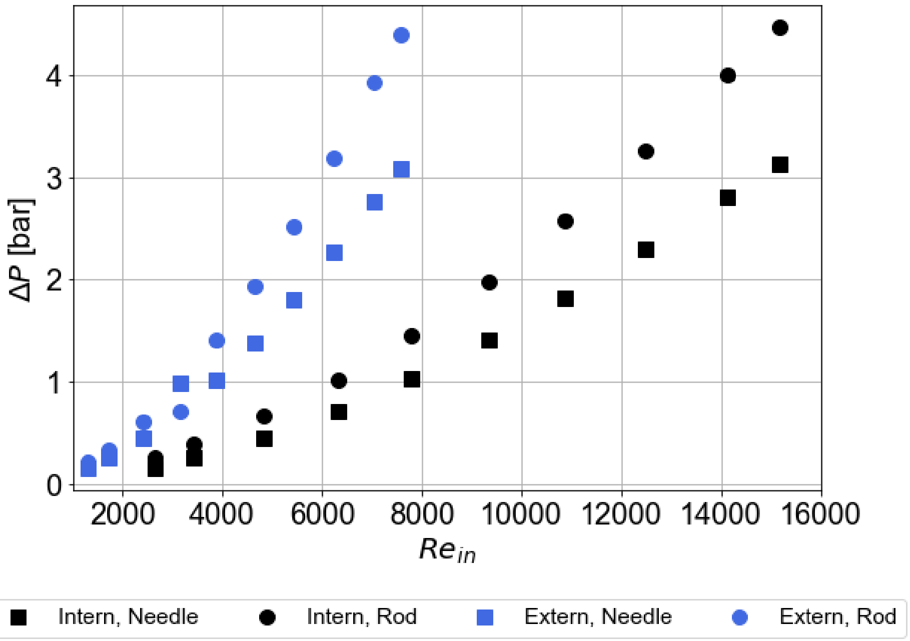

Source: Author (2023).

The behavior of each channel is Illustrated in Figure 29 (the first and second graphs for cases 2 and 3, respectively) considering both the rod and needle measurements. In the case of countercurrent flow, the elastic deformation profile of the plate becomes more complex due to the difference in flow direction. This is because there is a variation in the gradient direction between the inlet and outlet of each branch. The orientation of the curves of the expanded inner channel and the constricted outer channel illustrates this phenomenon. The channels exhibit an opposed profile as the inlet flow increases, indicating that the plates do not deform uniformly, creating gripping zones and independent separations on each channel despite the pressure difference causing constriction in one of the channels.

Figure 29 - Results of hydrodynamic bench tests for countercurrent flow configuration in two inlet pressure ratio conditions

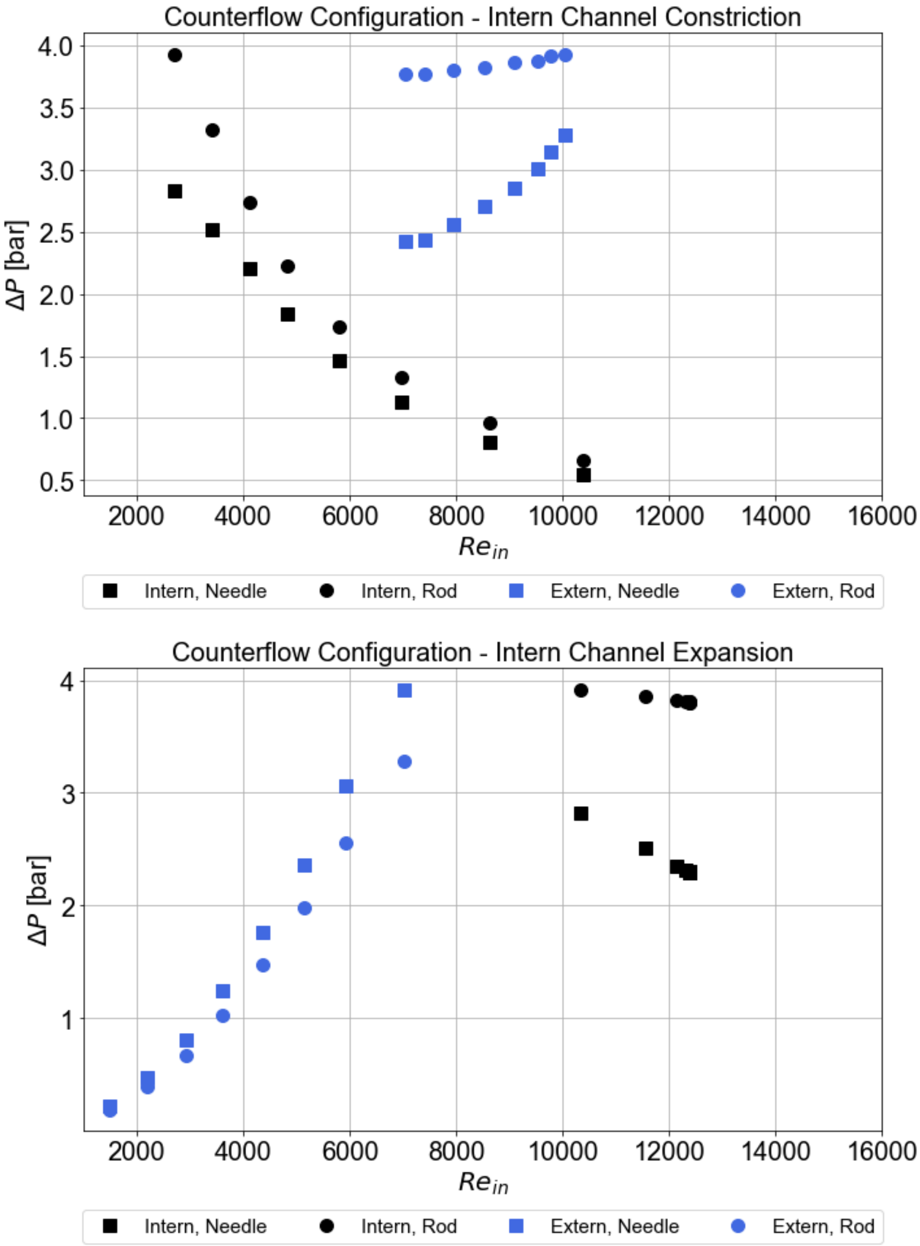

Source: Author (2023). Above: Countercurrent configuration with internal channel under constriction (Case 2); Below: Countercurrent configuration with internal channel under expansion (Case 3).

Figure 30 - Analysis of the pressure drop variation in relation to the branch pressure measurement point

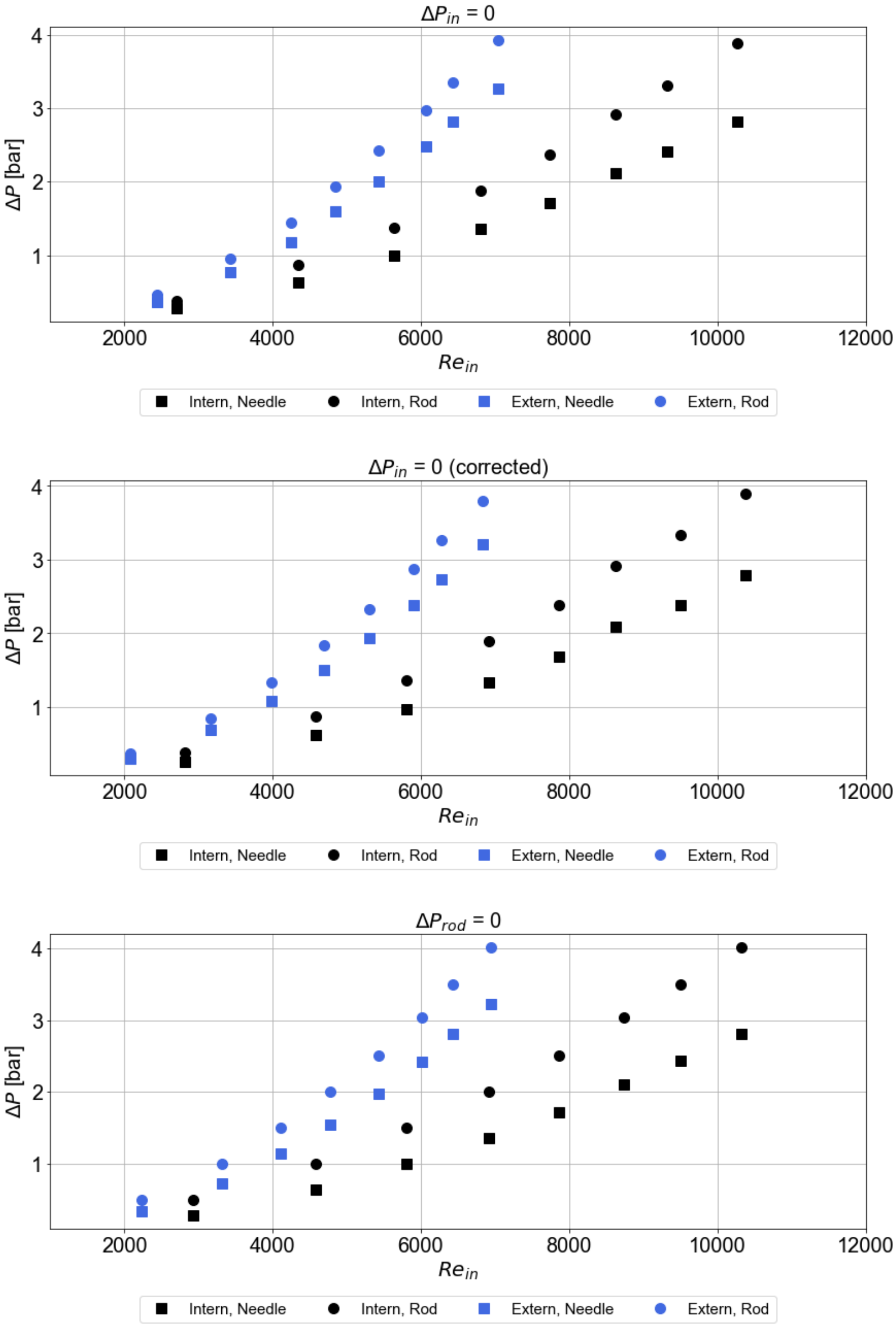

Source: Author (2023).

Figure 30 shows the results of testing case 4 under three different scenarios: $\Delta P_{in} = 0$, $\Delta P_{in,rod} = 0$ and $\Delta P_{in,corrected} = 0$. In the first scenario, the inlet pressures in each branch were symmetrical, as measured by the pressure transducer installed on the piping prior to the inlet nozzles. The second scenario is akin to the initial one, but incorporates a correction for measurement that considers the internal branch sensor's zero point (measurements always commence from a point other than zero relative to the pipe's water column).The third scenario also involves symmetrical inlet pressures in each branch, but the condition of ΔP_{in} is now defined as $\Delta P_{in} = \Delta P_{in,rod} = \left|P_{rod,1} - P_{rod,2}\right|$, that is, the piping is ignored and the reference value is the measurement made by the rod in the center of the inlet nozzles of each branch. Conducting this test is vital to ascertain if the pipeline's head loss impacts the measurements, thereby affecting the data's assessment. It is possible to see that there is no significant variation in the pressure drop values, however, in order to compare the input values at the same point as those measured in the future using the numerical method, the measurement point chosen was that of the rods.

Figure 31 presents the results of cases 5 through 12 in a clockwise sequence. Internal branch in expansion; external branch in constriction; internal branch in constriction and external branch in expansion. Case 4 is added to all figures for comparison of the symmetrical situation. The titles of the graphs indicate the reference used for comparison, in the format Be (S, Br, M) where: "Be" indicates the behavior of the pack (constriction or expansion of the internal branch or the external branch); "S" indicates the load application condition, with $\Delta P_{in} = cte$ referring to a test in which there is no variation of ΔP_{in} between the points of the curve and $\Delta P_{in} = cte$ referring to a test in which there is variation of ΔP_{in} between the points of the curve. curve; "Br" indicates the reference branch to which the plotted measurements belong, which can be the internal or external branch; and "M" indicates the measurement point chosen to display, which could be the rod or the needle. Thus, "Intern Channel Expansion ($\Delta P_{in} = cte$, Intern, Needle)" indicates that the graph shows data collected through the needle in the internal branch, and such data refers to tests in which the inlet pressure of the internal branch is greater than the than the inlet pressure of the external branch and there is no variation in ΔP_{in} between the points of the curve.

Figure 31 - Results of tests on a hydrodynamic bench for the condition of constant pressure difference between branch inlet pressures

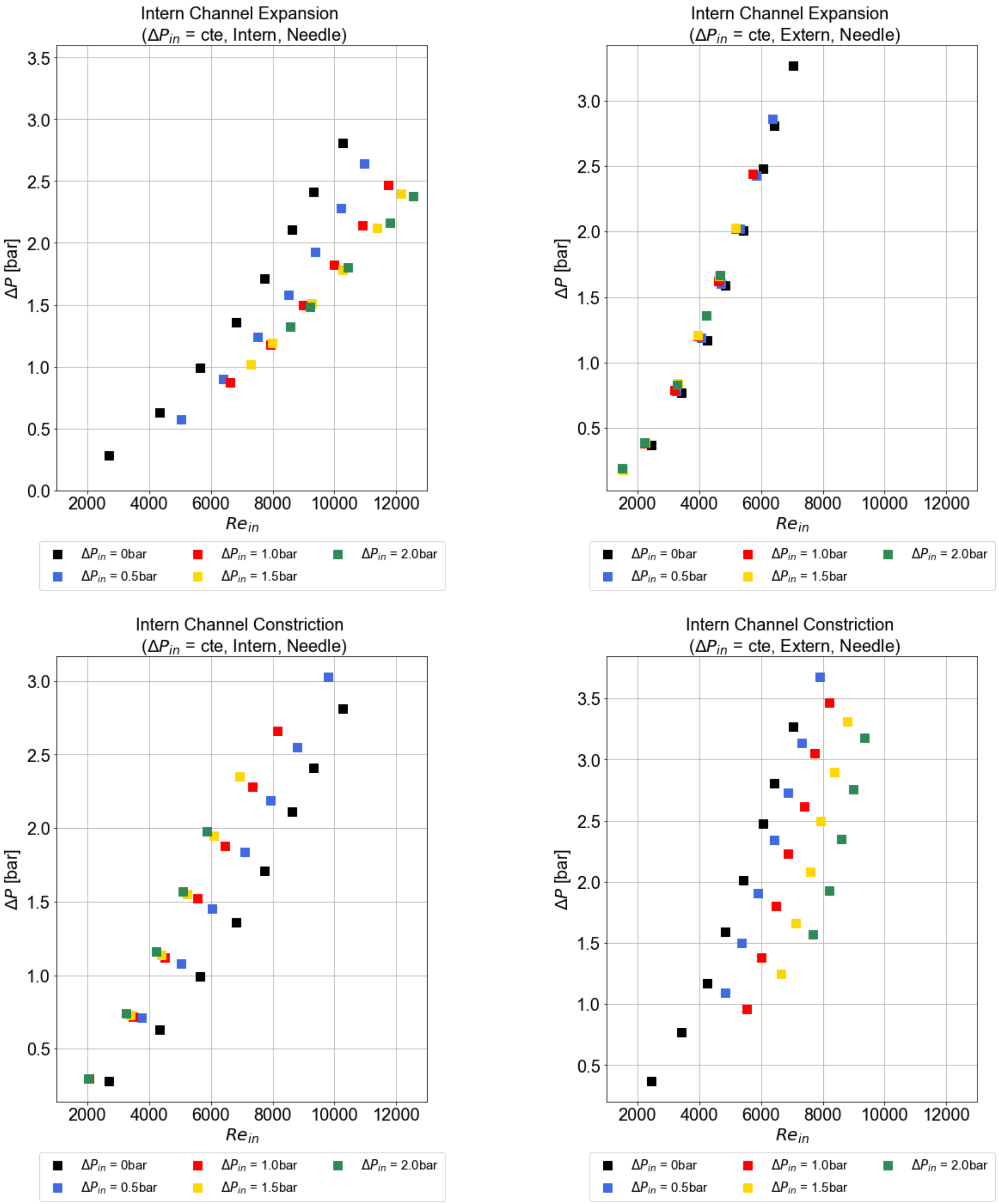

Source: Author (2023). Upper left: Intern channel expansion; Upper right: Extern channel constriction; Lower left: Intern channel constriction; Lower right: Extern channel expansion.

The initial two graphs portrayed in the figure showcase the contrasts between expansion and constriction situations across each channel. Due to the limitations imposed by the cover plates on the external branches, the expansion that would occur uniformly on the branch walls is instead concentrated solely on the interfacial plate of the two branches. Subsequently, the load on the plate doubles, giving rise to a more severe expansion. In cases of strangulation, the challenging nature of the branch's ability to adjust becomes apparent, ultimately restricting its ability to deform.

The two graphs below compare the behavior of each branch in the given conditions, demonstrating the most abrupt variation of the friction factor in the expansion conditions as anticipated, where there is opening of the preferential flow path. This pair of graphs also shows the load asymmetry condition in the external branch, since the friction factor curves in the expansion conditions are noticeably more pronounced in the external branch compared to the internal one.

In the constricted condition, both branches present curves varying in the same range, but with different inclinations: the internal branch varies its friction factor between 0.55 and 0.25, showing inverse dependence of the variable with an increase in the inlet flow and direct with an increase of the pressure difference. In turn, the external branch varies between 0.45 and 0.20, but with curves directly proportional to flow and inversely proportional to pressure.

In the following sections, the previously presented results will be revisited, with the aim of validating the curves obtained with the numerical methods used in this work.

4.1.2 Structural results

Figure 32 shows the results of structural tests on a hydrostatic bench for single and double loading (one or both of the pressurized branches) in 11 load conditions (0 to 10 bar). On the left are the widening curves and on the right are the stretching curves. The first two graphs show the data collected on plate number 10 of the pack, near the fluid inlet, while the two middle graphs show the data collected on plate number 44 of the pack, in the middle of the exchanger, and finally the last two graphs show the data collected on plate number 78 of the pack, near the end of the exchanger.

Figure 32 - Experimental results of widening and stretching for plates 10, 44 and 78 under single and double loadings

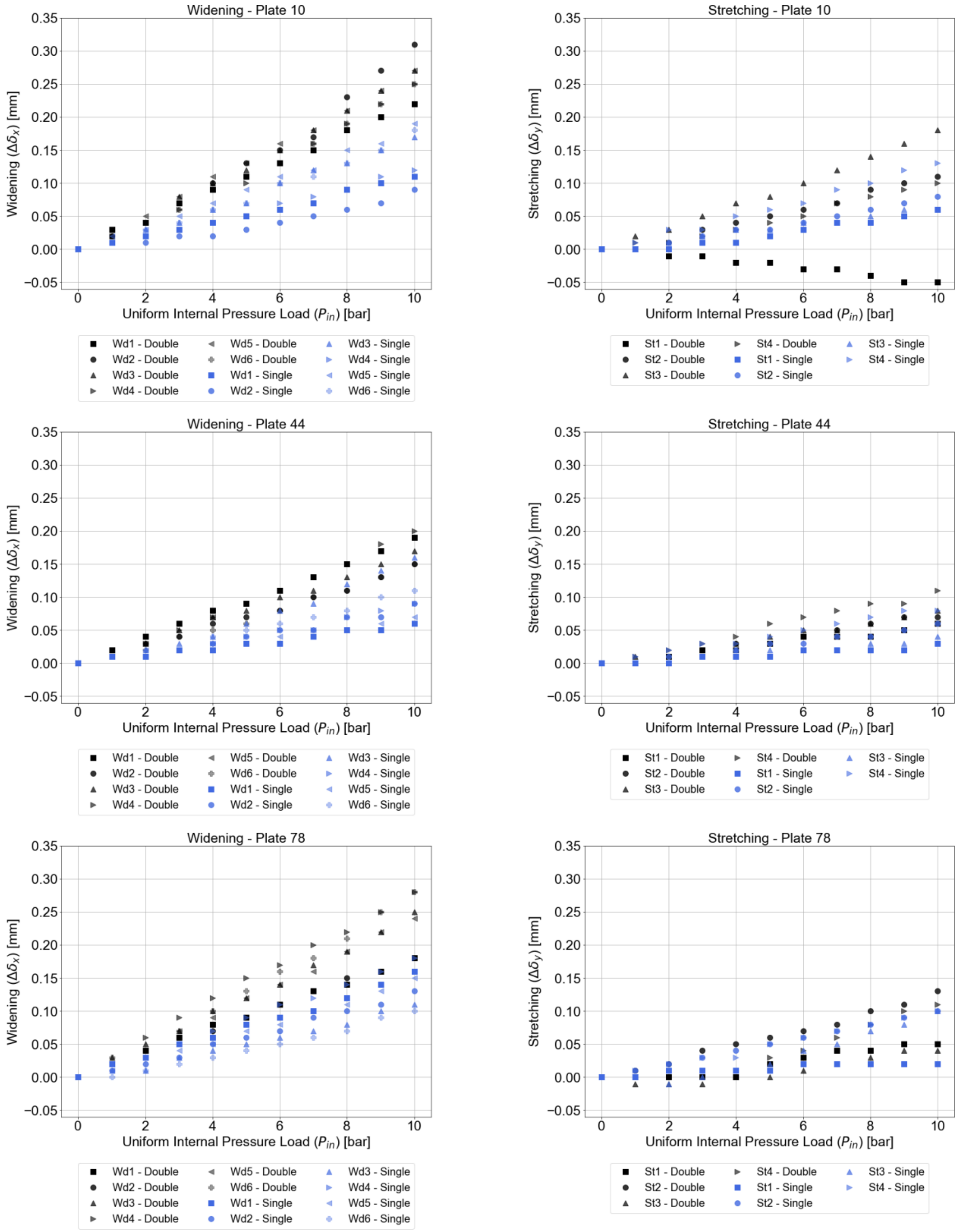

Source: Author (2023).

The curves show linear behavior with respect to inlet pressure for all measurements. Both displacements have the same order of magnitude, confirming the idea that they are coupled phenomena, with the widening presenting slightly higher magnitudes.

The Wd2 point presents larger magnitudes on plate 10 compared to plate 78, indicating that the plate inlet nozzle widens more significantly on the first plates of the pack, with this behavior attenuating as the fluid flows to the end of the exchanger. Point Wd6, which indicates the plate outlet nozzle, shows the opposite behavior. The widening in the middle of the plate is maintained throughout the exchanger.

In terms of stretching, the four points maintain similar behavior among themselves and throughout the pack, with valid mention of the point St1, in the upper left nozzle of the plate, which presents a different behavior from the others and requires careful evaluation.

In all cases, for both displacements, the double loading condition proved to be more significant, a behavior that can be attributed to the fact that single loading allows greater freedom for the plate to deform in the normal direction (separation), while double loading restricts such movement, causing deformations in the plane of the plate to be more accentuated. For validation purposes, only double loading will be considered in the next sections.

4.2 NUMERICAL RESULTS

4.2.1 CFD results – Undeformed geometry

Figure 33 - Step indication: CFD of undeformed geometry

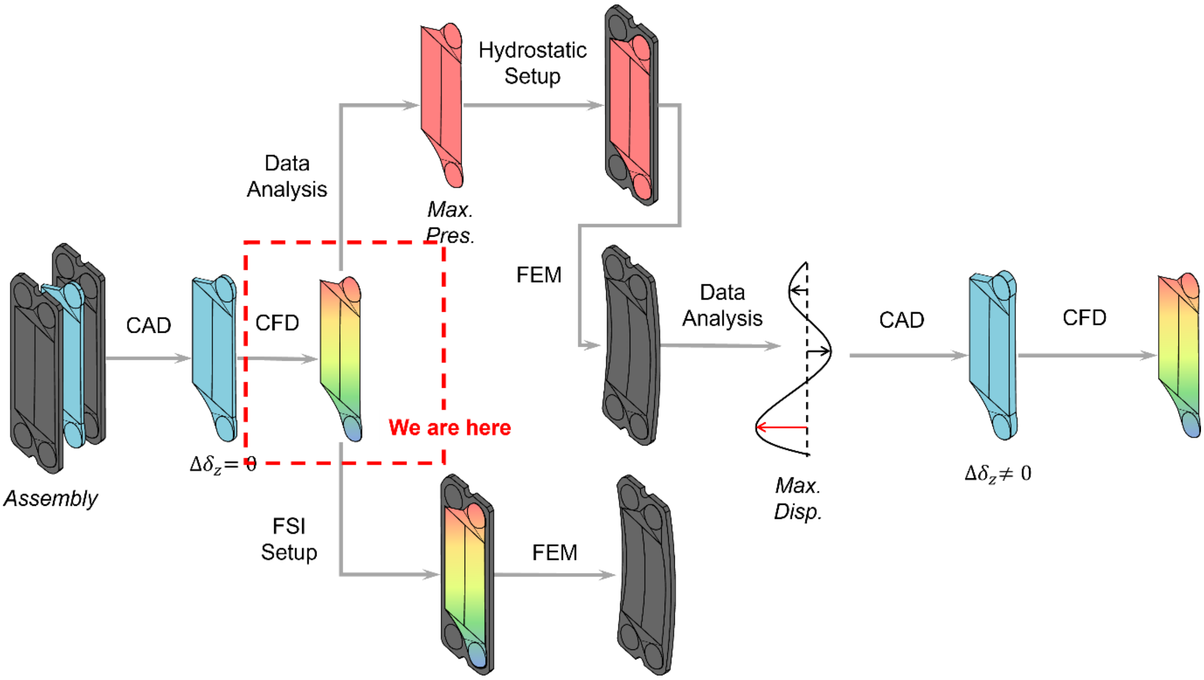

Source: Author (2023).

4.2.1.1 *Internal flow*

Figure 34 shows the distribution of velocity in the central plane of the internal flow for the original domain (initial fluid geometry, without considering the fluid-structural interaction), varying the inlet mass flow ($\dot{m}_{in}$) between 1 kg/s and 4 kg/s. It is possible to identify characteristic structures from the flow in corrugated plates, such as the acceleration of the fluid at the edges, the stagnation near the center of the corrugated channel, the sudden acceleration in the distribution gallery – both inlet and outlet – and the vorticity in the outlet port. It is also noticeable the deceleration zones that are caused by the contact points in the heat exchange channel, a fact that promotes greater local turbulence and greater heat exchange for the fluid. Absolute velocity values in the fluid range from close to zero (in stagnation zones) to approximately 19.5 m/s.

Figure 34 - Internal flow velocity distribution for the original geometry of the fluid domain

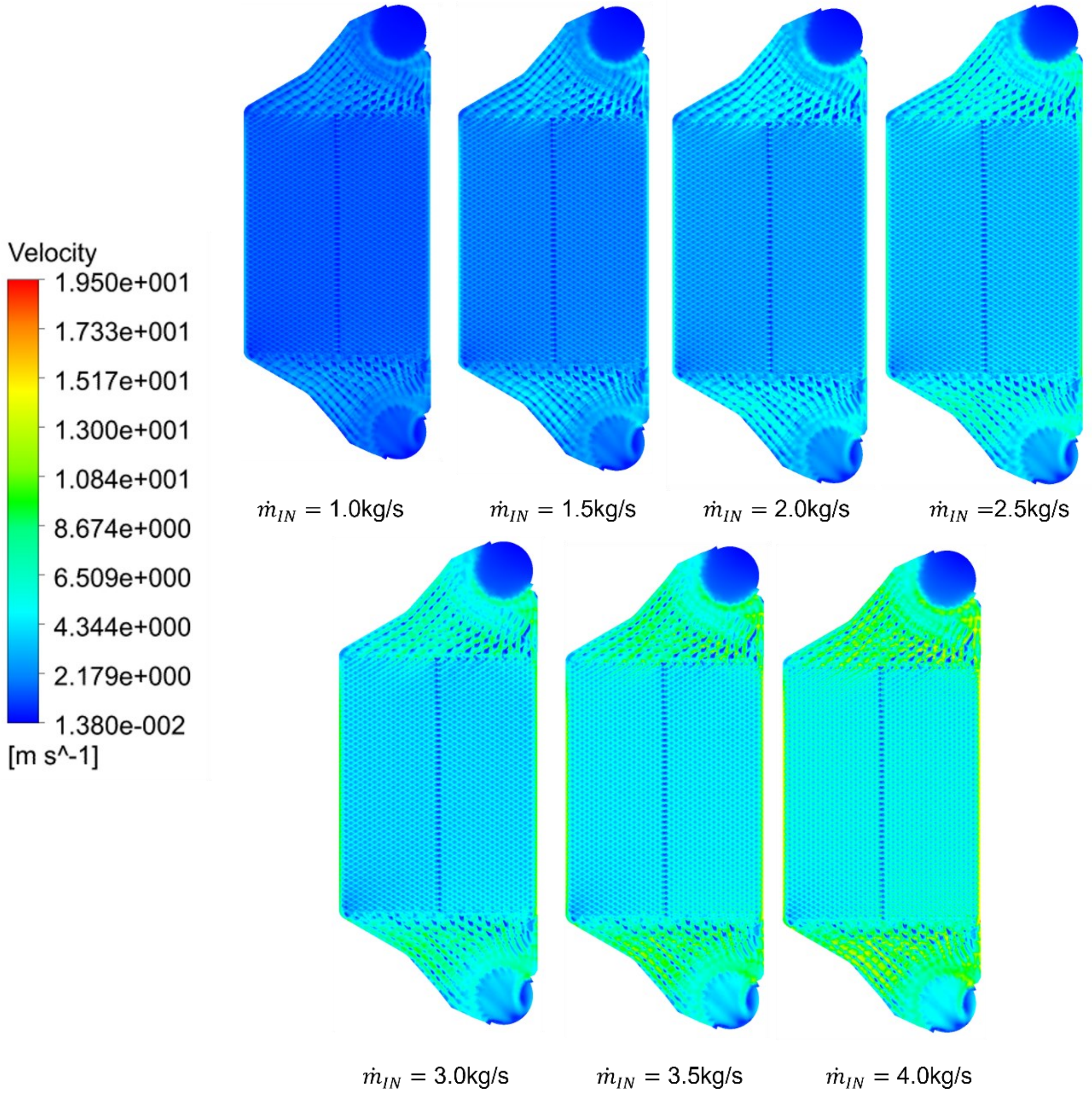

$\dot{m}_{IN}$ = 1.0kg/s $\dot{m}_{IN}$ = 1.5kg/s $\dot{m}_{IN}$ = 2.0kg/s $\dot{m}_{IN}$ =2.5kg/s

$\dot{m}_{IN}$ = 3.0kg/s $\dot{m}_{IN}$ = 3.5kg/s $\dot{m}_{IN}$ = 4.0kg/s

Source: Author (2023).

Figure 35 shows the pressure distribution in a central plane of the internal fluid domain without deformation. An almost linear profile can be seen for the pressure drop in the fluid, with an increase in magnitude as the inlet flow increases, but with no change in the behavior of the profile. The highest pressure zone is found at the entrance of the channel, dropping drastically as the fluid travels through it, as a result of the acceleration caused by the distribution galleries and the friction. Along the transverse axis, there is a small variation in the magnitude of the pressure, with an accentuation in the slope of the profile as the fluid approaches the outlet distribution gallery.

The velocity and pressure profiles can be seen in greater detail in Figure 36, in which curves of such variables are acquired in a straight vertical line formed between the centers of the two ports of the domain (following the y-axis defined at Figure 17). The approximately linear profile verified in the pressure field corroborates results found extensively in the literature for GPHEs. The symbols used in the legend of Figure 36 indicate the variation in displacements in the Z+ direction (separation) of the plates that form the fluid volume. This variation is relative to the original distance previously mentioned in the geometry definition section and $\Delta\delta_z = 0$ indicates the undeformed geometry.

Figure 35 - Internal flow pressure distribution for the original geometry of the fluid domain

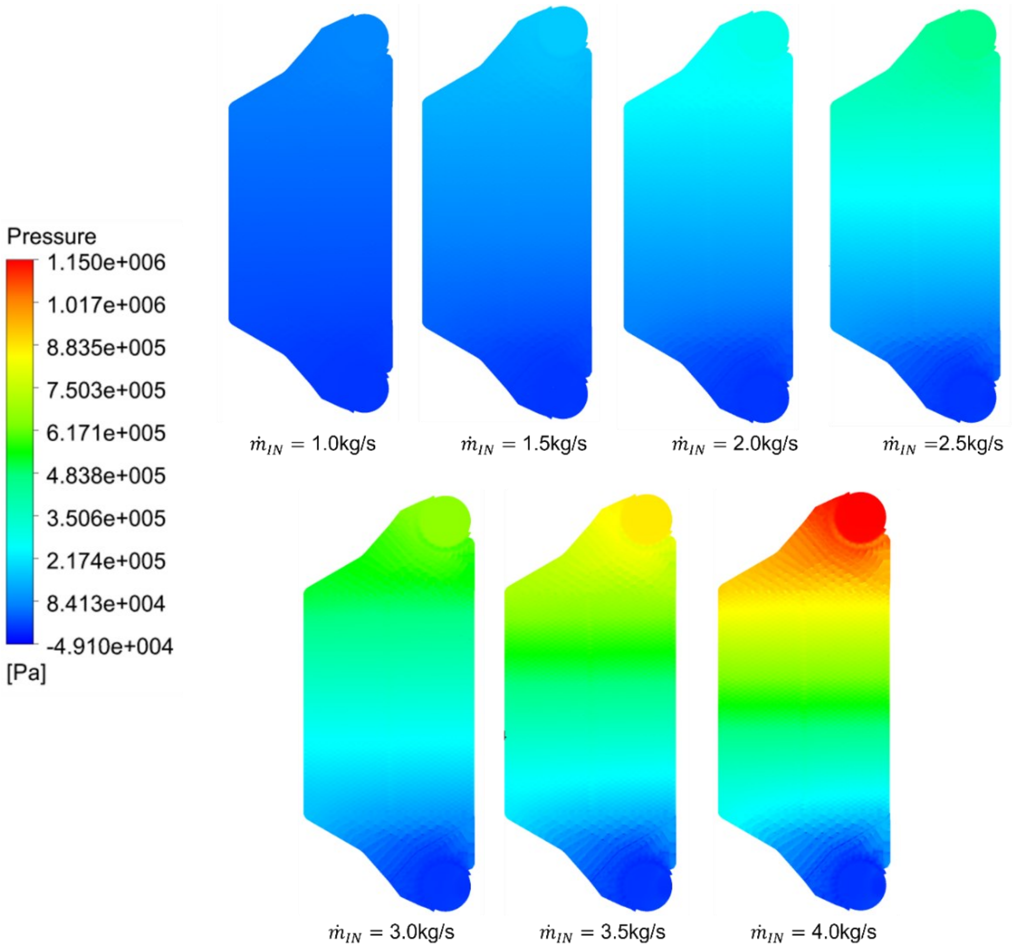

Source: Author (2023).

Figure 36 - Velocity and pressure curves on the path between ports of the internal channel (undeformed geometry)

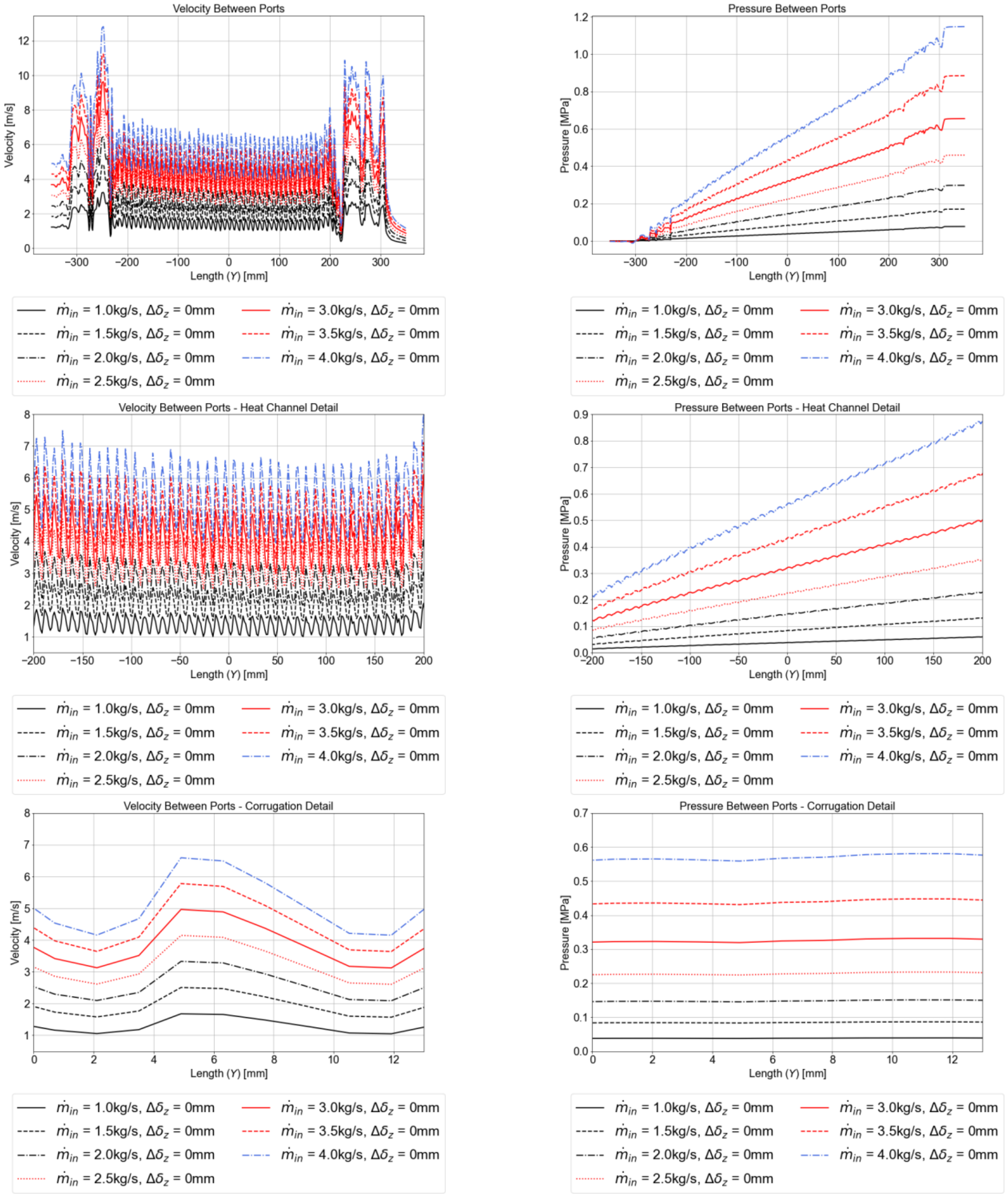

Source: Author (2023). First row: profiles for the whole plate; Second row: profiles for the heat Exchange channel; Third row: Profiles for one only corrugation; Left: Velocity profiles; Right: Pressure profiles.

It can be noticed that with the increase in the inlet flow, the velocity profile maintains the general behavior of its curve, with an increase in the amplitude and the average of the oscillations. In the pressure profile, the most visible change caused by the inlet flow in the curve is its slope, indicating that greater inlet Reynolds number values generate greater pressure drops along the domain. A section dedicated to the validation of such results with the aid of the previously shown experimental data will be presented later in the work.

For future analysis, it is important to highlight the following behaviors of the internal channel:

- Significant flow acceleration in the areas of the inlet and outlet distribution galleries;
- Stagnation zones in the center of the Exchange channel (the tip of the "V" of the Chevron angle) and at the contact points;
- Large magnitudes of pressure at the channel inlet and low pressures at the outlet forming a linear pressure profile along the length;
- Presence of vorticity in the channel outlet port, causing the referred pressure drop at the outlet;
- Negligible pressure variation along the width despite the geometric asymmetry in that Direction (see Figure 18).

4.2.1.2 External flow

The external flow channel was defined in an upward direction, unlike the internal channel, to characterize a countercurrent flow pattern in the plate pack. Both fluid passes in this channel have an inlet at the bottom and an outlet at the top. Figure 37 shows the pressure distribution for the channel, which varies with the application of inlet mass flow with values between 1 kg/s and 4 kg/s.

The indicated inlet mass flow always refers to the data collected just before entering the branch and it is important to note that each pass of the channel receives half of this value. With the help of Figure 18, it is possible to infer, then, that the indicated inlet flow is defined for the branch (fluids F1-F3) and not individually for the passes. In the figure, F1 represents the first pass of the branch and F3 the second one.

It is possible to notice that the same behavior shown by the internal branch is shown in both passes of the external branch. Compared to the internal branch, there is greater attenuation in the magnitude of the pressures (maximum values drop from 11.5 bar to 3.5 bar) due to the increase in passes. When comparing the two passes of the external branch, it is noticed that there are no visible differences in the behavior of the pressure distribution between them, since the maldistribution along the passes is not so critical with such a low number of plates.

Figure 37 - Pressure distribution in the central plane of the external fluid domain for inlet flow conditions of 1.0 kg/s ≤ $\dot{m}_{in}$ ≤ 4.0 kg/s

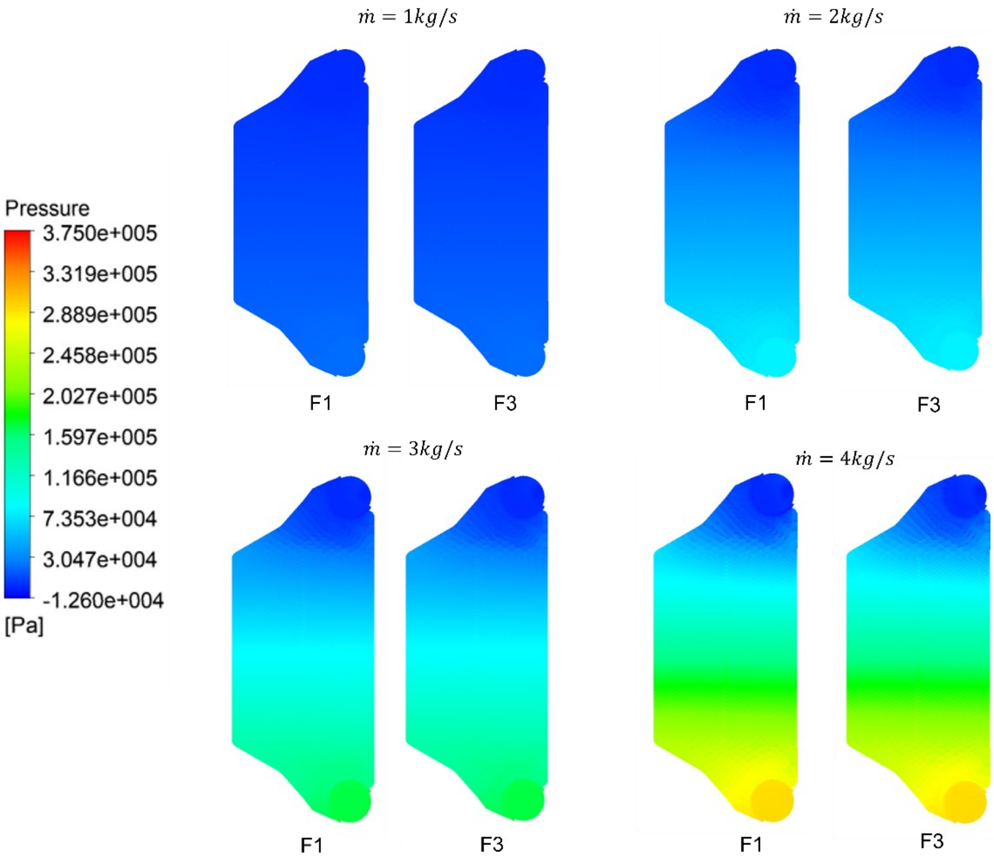

Source: Author (2023). F1: First pass of the external branch; F3: Second pass of the external branch.

The same trends observed in the pressure distribution can be seen in the velocity distribution (Figure 38), such as the drop in velocity magnitudes (maximum values drop from 19.50m/s to 9.45m/s) and the consistency of the profile observed in the internal channel on both external channel passes. Due to the change in flow direction, the recirculation zones are located at the top of the channel.

Figure 38 - Distribution of velocities in the central plane of the external fluid domain inlet mass flow conditions of 1.0 kg/s ≤ $\dot{m}_{in}$ ≤ 4.0 kg/s

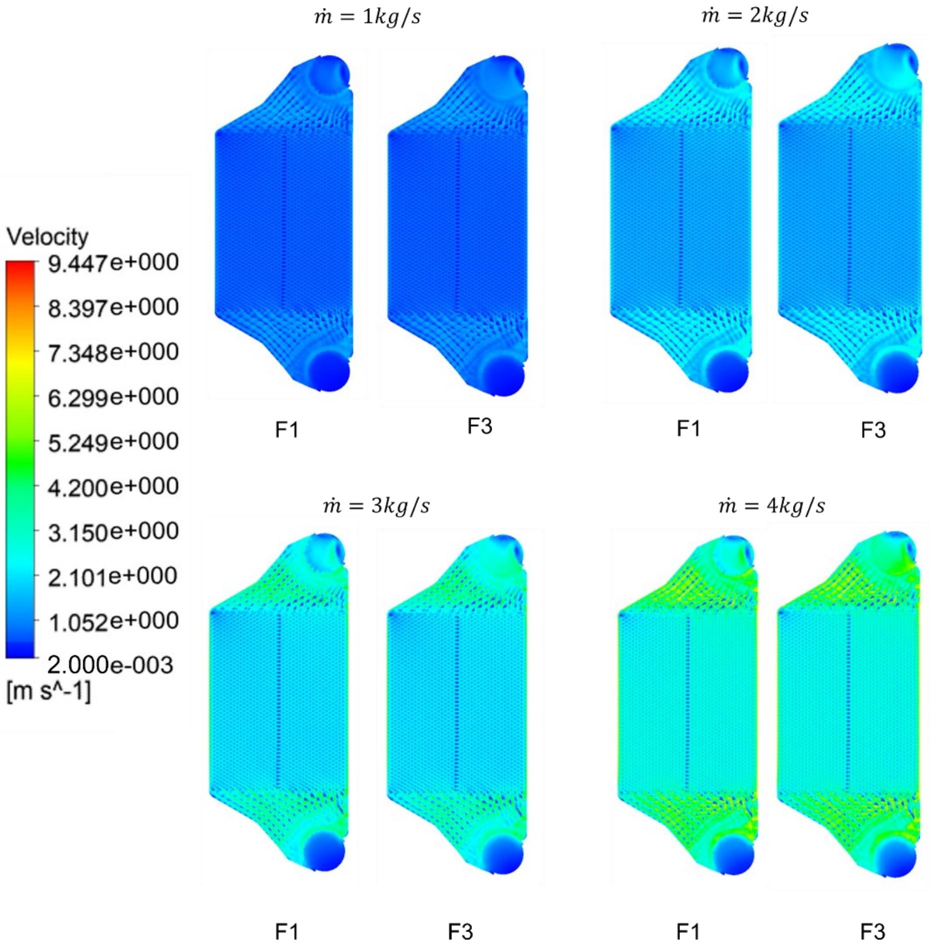

Source: Author (2023). F1: First pass of the external branch; F3: Second pass of the external branch.

Figure 39 shows the comparison of the profile results between the internal and external branches. It shows the amplitude and average attenuation of the external branch in relation to the internal branch. Also, it is important to note that in neither case is the peak of the oscillation in the corrugated channel centralized. In the figures above, 0 mm indicates the center of the plate, while -300 mm indicates the bottom of the plate.

Figure 39 - Velocity profiles for the path between inlet and outlet ports for the internal and external fluid domains under the conditions of $\dot{m}_{in}$ = 2.0 kg/s

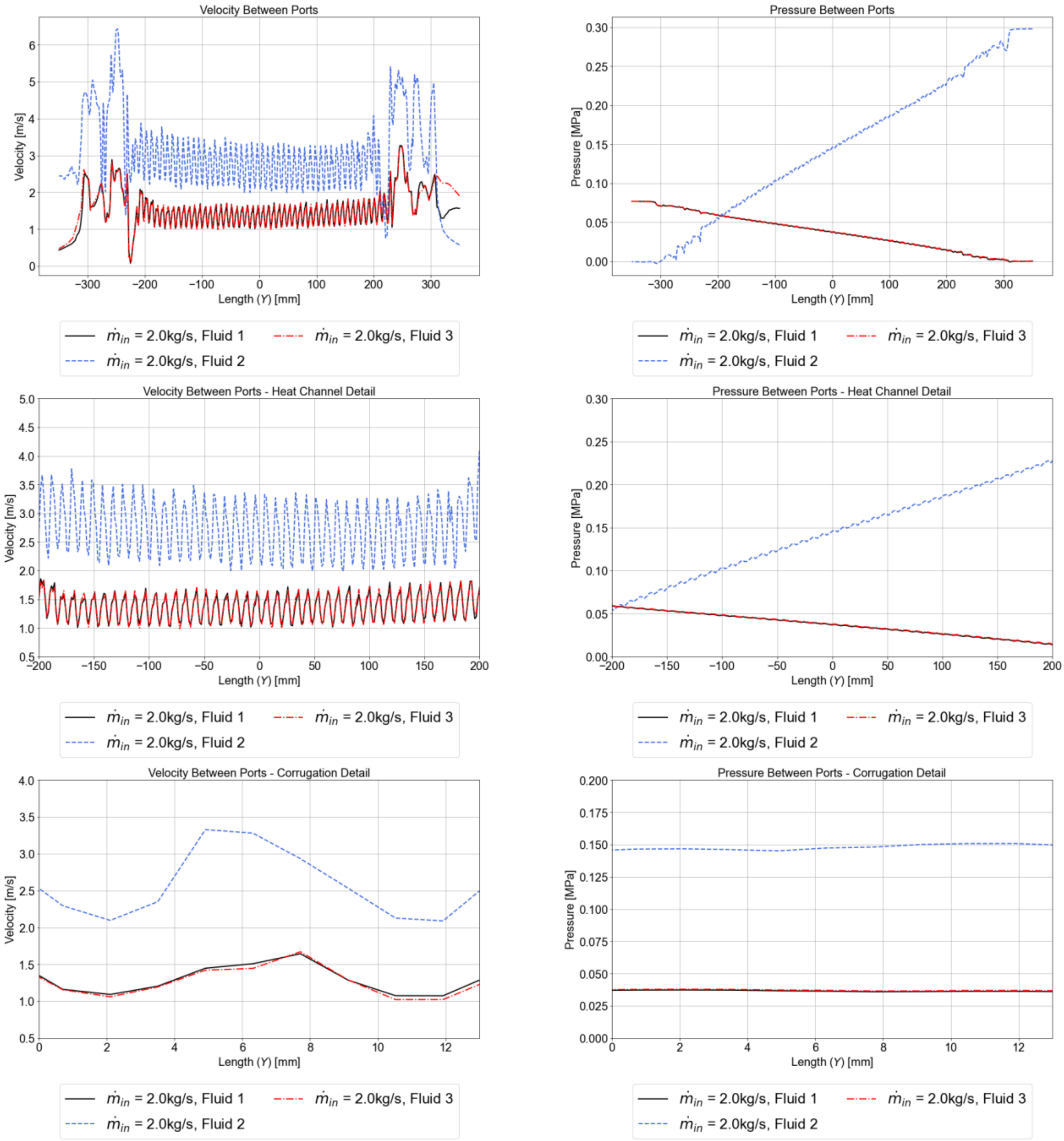

Source: Author (2023). First row: profiles for the whole plate; Second row: profiles for the heat Exchange channel; Third row: Profiles for one only corrugation; Left: Velocity profiles; Right: Pressure profiles.

4.2.1.3 Validation

Figure 40 shows the comparison of the experimental results described in Part I with the pressure drop curves acquired by the numerical method, CFD, on both branches (internal and external). When there is no clear indication of the measurement point chosen for the curve, it is defined as needle measurement.

The numerical curves, indicated in red, extrapolate the values for larger inlet mass flow rates than those shown by the experimental results, since the hydrodynamic bench has restricted operating limits.

It is possible to notice that the experimental analysis condition that most diverges from the numerical results is that of variable ΔP_{in}, represented by Cases 2 and 3, illustrated by the sets of points in blue and yellow. Such divergence occurs, because different pressure levels (both at the channel inlet and between channels) generate different deformations, while numerical simulation alone (CFD only) is not able to identify the final state after elastic deformation. Therefore, pure CFD is highly representative in conditions of non-varying ΔP_{in}, such as the parallel flow condition or the crossflow condition for identical inlet pressures ($\Delta P_{in} = 0$).

In the $\Delta P_{in} = 0$ condition, there is a greater agreement between the numerical and experimental curves for the inner channel - about 10% deviation - mainly for the points collected through needles, to the detriment of the points collected through the rods. This is because, as seen in the section above, the regions of the inlet port and the inlet distribution gallery are the ones that suffer the greatest influence of the flow because they are the regions of higher pressure value.

Another important point is the condition of symmetry of the loading with respect to the two sides of the plate: there is no symmetry with respect to the longitudinal axis of the fluid, indicating that there is no loading in opposite direction on the other side of the plate in the zone of higher pressure (inlet port and inlet distribution gallery), unlike the exchange channel. Therefore, the CFD model - which does not take into account the effects of the elastic deformation of the plate on the flow structure - describes more faithfully the region between the two needle pressure inlets.

Figure 40 - Hydrodynamic results validation

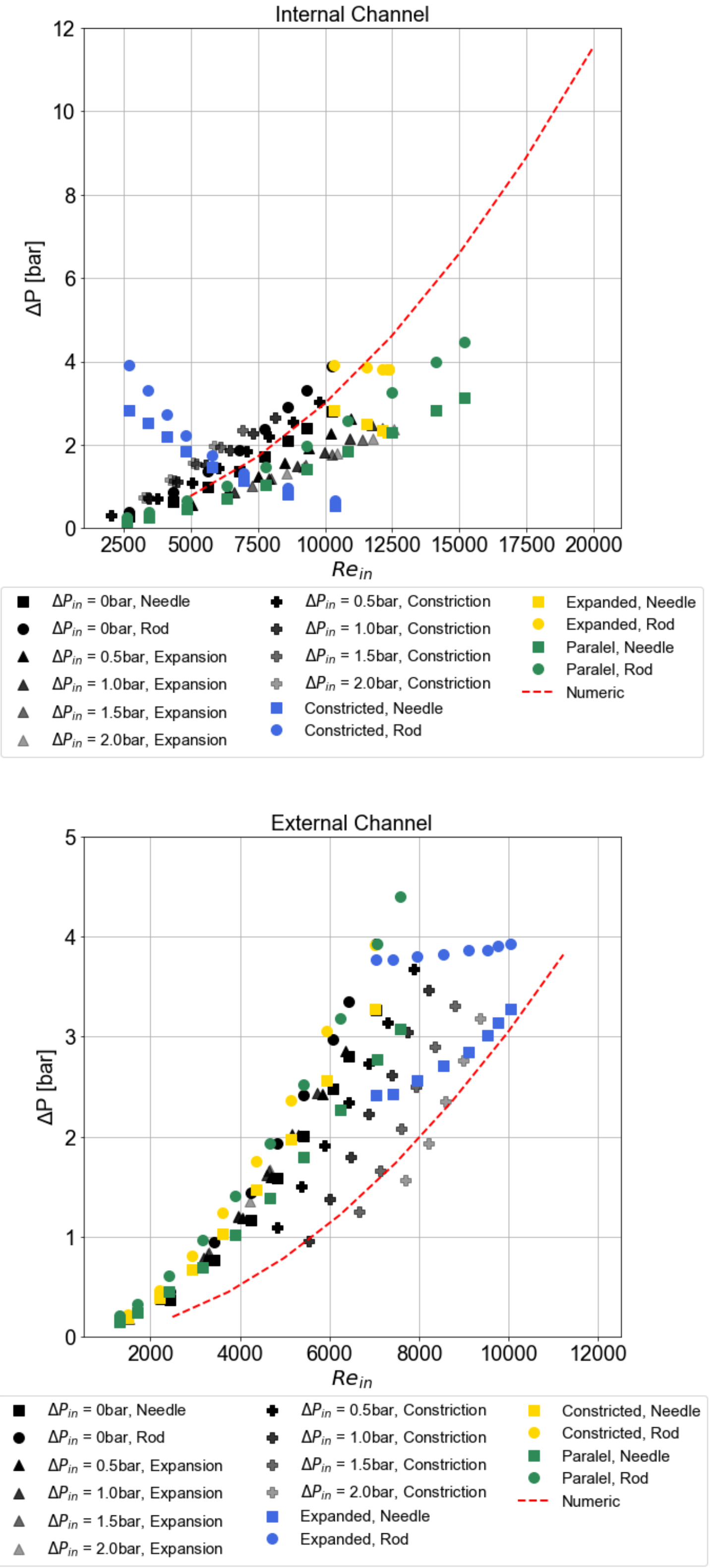

Source: Author (2023).

In the last graph of Figure 40 the comparisons of numerical and experimental data for the external channel can be found. The agreement present in the pressure difference curves is remarkable, especially in relation to the data series that represent the constriction condition of the external channel. Table 13 lists the deviation values, calculated by the expression ${\Delta P_{EXP} - \Delta P_{NUM}}/{\Delta P_{EXP}}$:

Table 13 - Numerical-experimental deviation for intern and extern channels

Data Series	Min. Numerical Error (%)	Max. Numerical Error (%)
Intern Channel		
ΔP_{IN}=0bar	1.04	22.48
ΔP_{IN}=0.5bar (Expanded)	30.36	39.64
ΔP_{IN}=1.0bar (Expanded)	42.45	66.87
ΔP_{IN}=1.5bar (Expanded)	23.89	91.63
ΔP_{IN}=2.0bar (Expanded)	51.01	141.00
ΔP_{IN}=0.5bar (Constricted)	3.62	38.09
ΔP_{IN}=1.0bar (Constricted)	1.98	63.38
ΔP_{IN}=1.5bar (Constricted)	14.05	63.83
ΔP_{IN}=2.0bar (Constricted)	24.89	64.96
Extern Channel		
ΔP_{IN}=0bar	46.65	53.30
ΔP_{IN}=0.5bar (Expanded)	55.44	57.52
ΔP_{IN}=1.0bar (Expanded)	57.07	58.74
ΔP_{IN}=1.5bar (Expanded)	58.11	64.70
ΔP_{IN}=2.0bar (Expanded)	57.87	69.06
ΔP_{IN}=0.5bar (Constricted)	31.66	48.13
ΔP_{IN}=1.0bar (Constricted)	1.74	73.92
ΔP_{IN}=1.5bar (Constricted)	5.55	46.09
ΔP_{IN}=2.0bar (Constricted)	2.25	37.72

Source: Author (2023).

It is possible to notice a greater variation in the CFD result in relation to asymmetric cases (with expansion and constriction), realizing that more work is needed to evaluate correlations to identify an expression that can better encompass the behavior of the GPHE. An approach to correct such a distortion effect is to use geometries that already take into account a pre-deformed profile (the result of fluid-structural interaction).

The understanding of the profiles generated by the flow, especially the pressure gradient, is important in order to establish a reasonable cause and effect relationship in the elastic deformation phenomenon and, consequently, to understand the deformation and stress profiles of the plates.

In a problem with complex loads and behaviors, it is necessary to isolate and simplify the sources in the first moments of the analysis, in order to understand which degrees of freedom are activated at each moment. For example, the loading can be limited to homogeneous applications and the effects of pressure drop can be ignored initially, working only with critical pressure levels, as indicated in the hydrostatic analysis methodology and discussed in the following section.

4.2.2 FEM results – Hydrostatic loading

Figure 41 - Step indication: Hydrostatic FEM

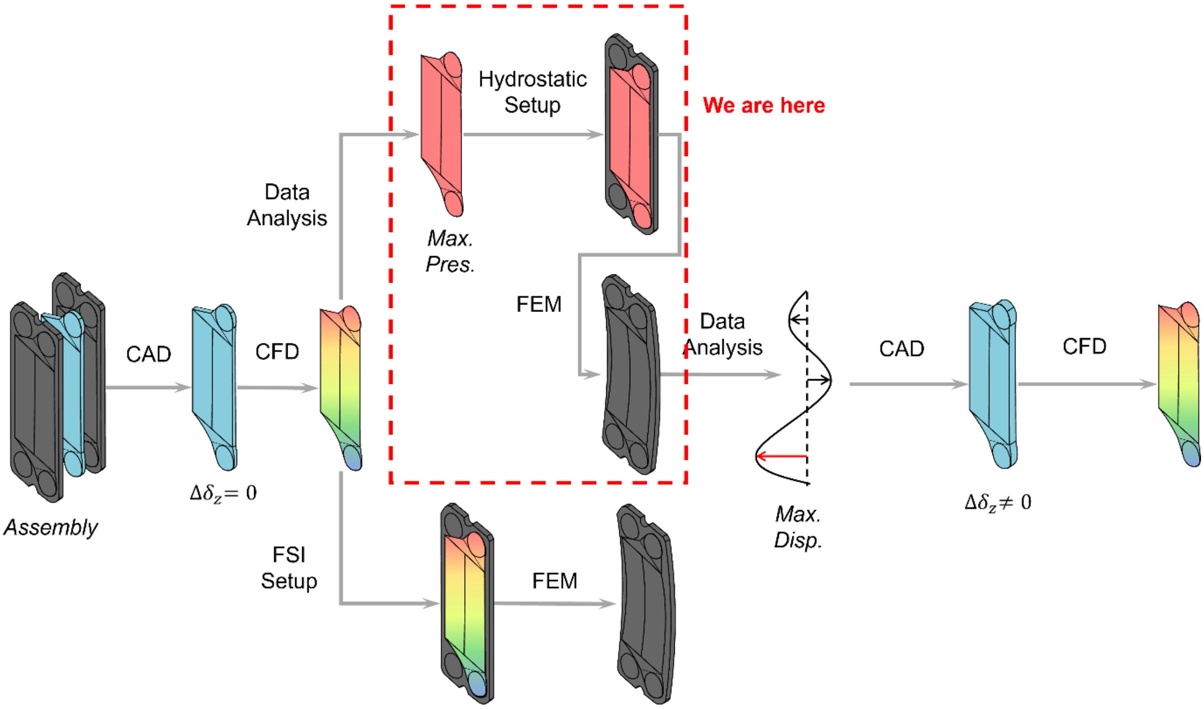

Source: Author (2023).

Figure 42 illustrates the stress and displacement behavior of plate 3 (Z+ direction, between plates 2 and 3) for the symmetric loading of 2bar-2bar. In Figure 42-a, Figure 42-b and Figure 42-c, it's found, respectively: the directional displacement distribution in the Z-axis, $\Delta\delta_z$ (Separation); the directional displacement distribution in the Y-axis, $\Delta\delta_y$ (Stretching); and directional displacement distribution in the X-axis, $\Delta\delta_x$ (Widening). Also, it is possible to see the displacement distribution in the von Mises equivalent stress direction for the assembly and loading steps (Figure 42-d and Figure 42-e, respectively).

The separation profile indicates rotation of the plate about its longitudinal axis, with displacements of greater magnitude near the ports. The profile tends towards the center of the plate and gradually decreases in intensity, growing again as it approaches the outlet port. With magnitudes close to 0.5 mm, the displacement reaches about 20% of the corrugation height.

The plate widening is more prominent in the heat exchange region, however, its order of magnitude is approximately 10 times smaller than the separation (maximum magnitude of 0.073 mm), leading to the conclusion that it is not the most critical elastic deformation mode for the plate. At the same order of magnitude as the widening (maximum magnitude of 0.053 mm), the stretching is concentrated at the ports, with cross behavior (maxima at the upper right and lower left ports, minima at the upper left and lower right ports).

Both in the assembly stage (pre-loading stage in which there is the initial tightening of the pack and the accommodation of the gaskets applied in all cases of structural analysis) and in the loading stage, the stresses are concentrated in the region of the upper and lower left nozzles, an effect caused by the positioning of the gasket in the channels (for visualization of the assembly, see Figure 17). Knowing that the maximum yield stress for mechanically formed 316L steel is 370MPa, all regions above this value are under plasticization and, since the analysis described here is in the elastic regime, they cannot be considered quantitatively, that is, it is known that there is plasticization, but there is no way to estimate its magnitude. The stress plot legend is in logarithmic scale for better visualization of the results.

Figure 42 - Stress and displacement behavior for 2bar-2bar symmetric loading

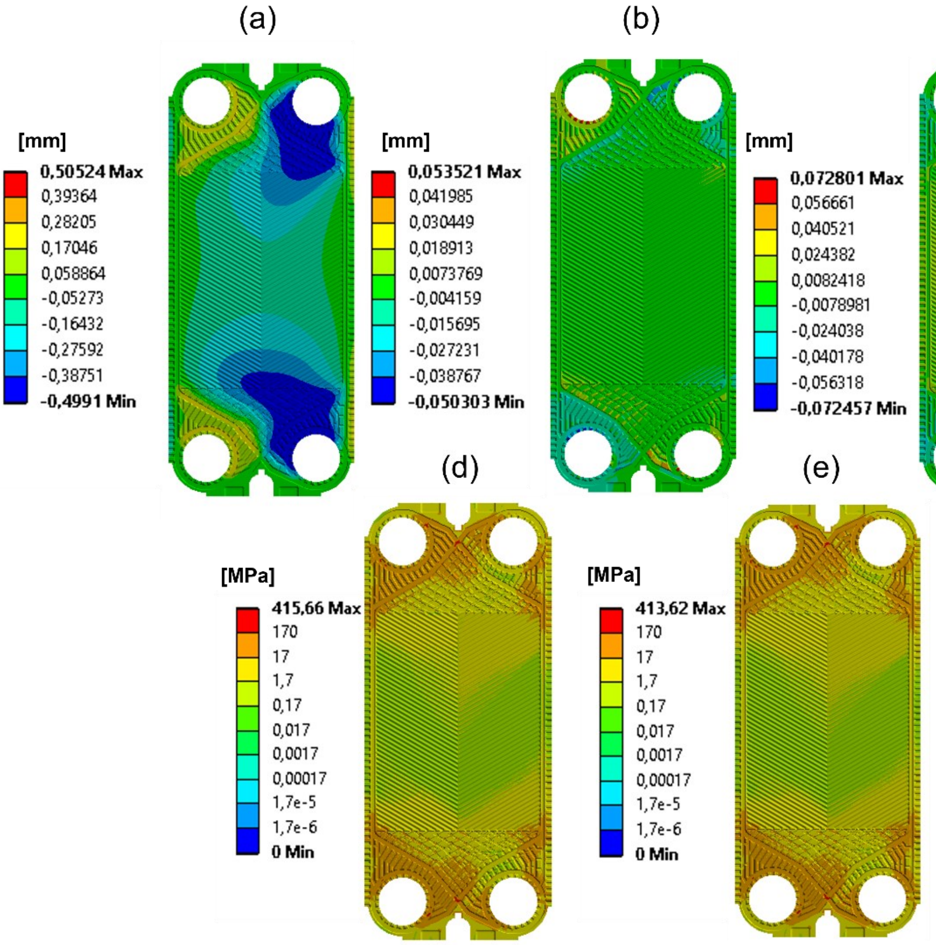

Source: Author (2023). a) Directional displacement distribution in the Z-axis, $\Delta\delta_z$ (Separation); b) Directional displacement distribution in the X-axis, $\Delta\delta_x$ (Widening); c) Directional displacement distribution in the Y-axis, $\Delta\delta_y$ (Stretching); d) Equivalent von Mises stress distribution in the sealing substep, $\sigma_{sealing}$; e) Equivalent von Mises stress distribution in the loading substep, $\sigma_{loading}$;

Figure 43 helps to understand the behavior of the stress field. The separation profile observed in symmetric loading promotes load balance in the heat exchange region, preventing the channels from being abruptly affected by hydrostatic loading, except at very high magnitudes, such as 6bar-6bar. However, for asymmetric loading, where there is no equilibrium, the exchange channel tends to deform much more than the ports, as seen in channel expansion at 2bar-4bar and channel compression at 4bar-2bar.

As this is a normalized legend, the torsional behaviour of the plate around the longitudinal axis is not as visible as seen in Figure 42-a, however, the difference in displacement directions between the right and left regions of the plate is still noticeable. It is estimated that such a torsional profile also happens around the transverse axis if the loading is no longer hydrostatic but takes into account the fluid pressure drop.

Figure 43 - Distribution of directional displacement in the Z axis (separation) in the pack loading substep for the hydrostatic methodology in the first iteration, for symmetrical loads of 2, 4 and 6bar and asymmetrical pressures of 2-4bar and 4-2bar.

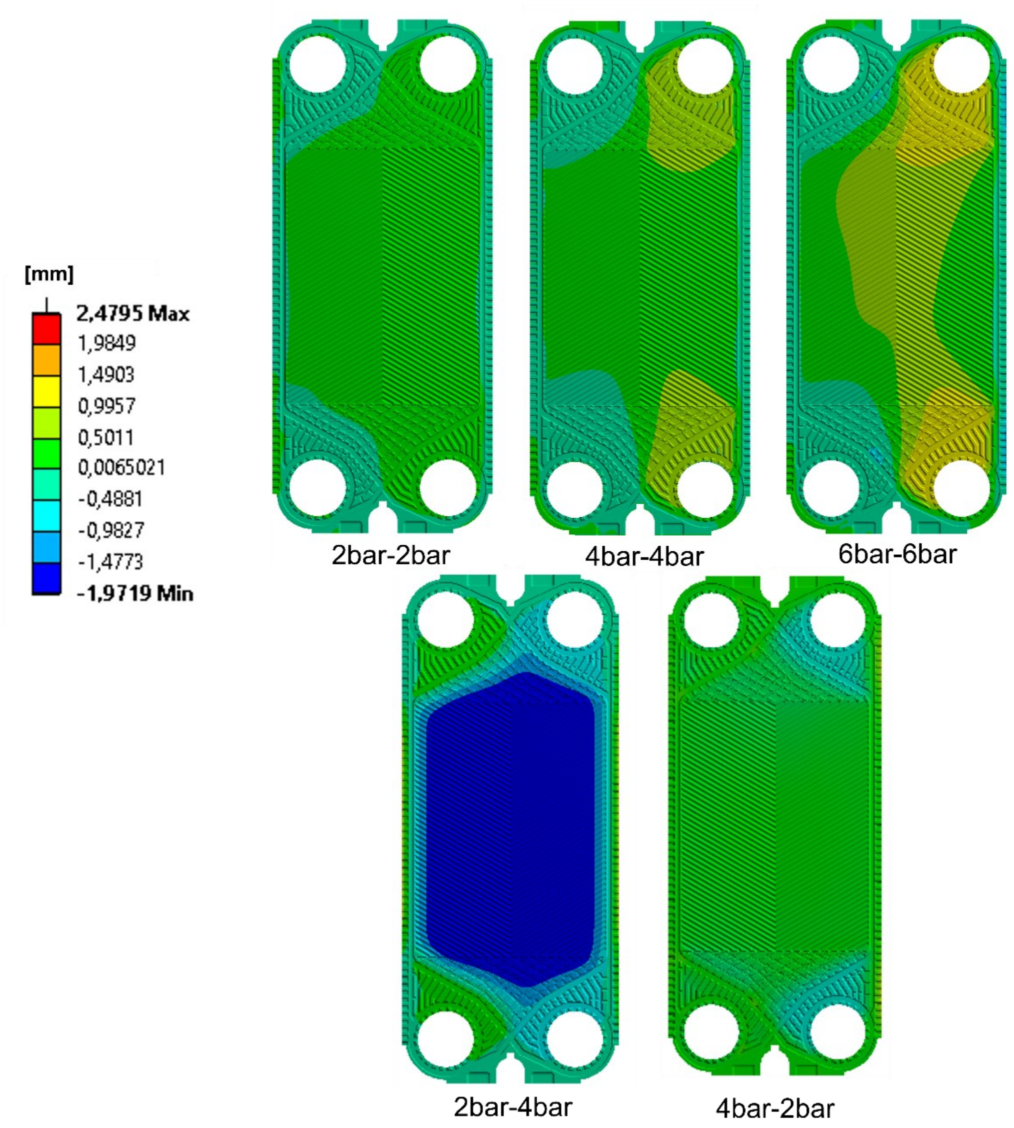

2bar-2bar 4bar-4bar 6bar-6bar

2bar-4bar 4bar-2bar

Source: Author (2023).

Given that separation presents itself as the most notable mode of displacement in the elastic deformation phenomenon, paths of interest were defined to evaluate detailed profiles of such a displacement. The investigation cover plateed three horizontal paths (between nozzles on the top, in the center, and between nozzles at the bottom), three vertical paths (between nozzles on the left, in the center and between nozzles on the right), and two gasket channels (top and bottom); as displayed in Figure 44.

Figure 44 - Paths of interest in the solid domain

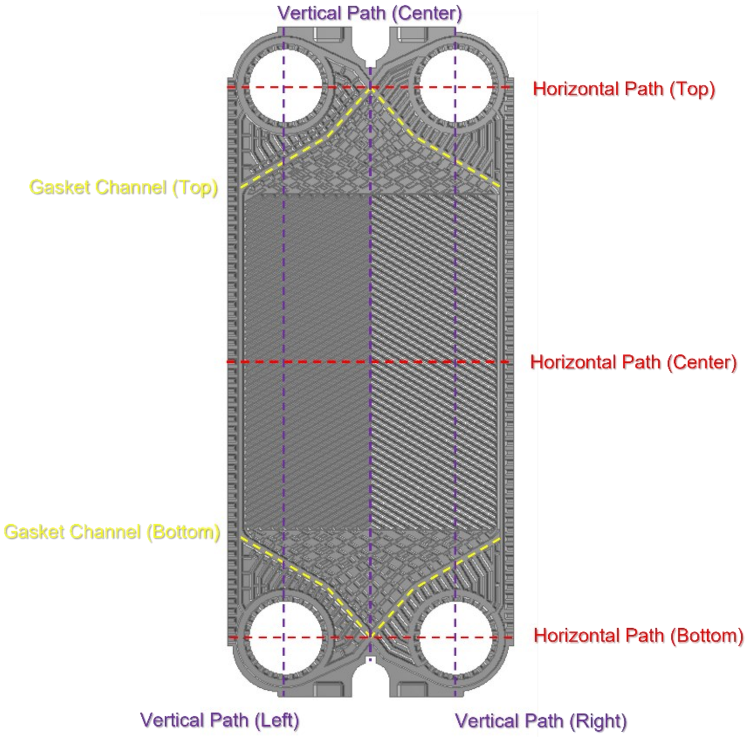

Source: Author (2023).

Figure 45 displays the separation profiles defined on the paths of interest of plate 2. The profiles for asymmetric loads are on the left. The profiles for symmetrical loads are on the right. For better comparison, the axes have been normalized.

In the gasket channels, the separation profiles indicate that the plate torsion profile is sustained in both inlet and outlet regions. Moreover, it is apparent that the alteration in loading nature (from symmetric to asymmetric or vice versa) does not have any apparent effect on the conduct of this region when external loading is considered as a reference. This can be observed by comparing the 2bar-2bar and 2bar-4bar curves or the 4bar-4bar and 4bar-2bar curves.

The horizontal pathways exhibit greater variation with loading, as demonstrated in the two central plots of Figure 45. Although the curves relating to the paths between the nozzles display behaviour comparable to the gasket channel's curves, the profile of the plate's center exhibits parabolic behaviour, which rises in degree with the magnitude of the loading pressure. In symmetrical loads, the rise is gradual and almost linear. Under asymmetric loads, the profile is nearly linear under compression (4bar-2bar) and is distinctly accentuated when under expansion (2bar-4bar). The linear sections of the profiles that drop between the ports relate to the port void space.

The vertical profiles between ports exhibit oscillatory behaviour, with peaks at the inlet and outlet and troughs at the center. Approaching the top of the plate, the central vertical profile experiences a gradual increase in its displacement. The vertical profile of the 2bar-4bar loading differs from the others once again by showing a more pronounced expansion behaviour, of approximately 2.5 mm as compared to the other profiles that expand their exchange channel to maximum values that are close to 0.75 mm.

The separation is considerably large, cover plateing 20% of the corrugation height for the 2bar-2bar loading, nearly 40% for 6bar-6bar loading and up to the full corrugation height, that is, 100% for 2bar-4bar loading.

Figure 45 - Separation profiles defined on paths of interest.

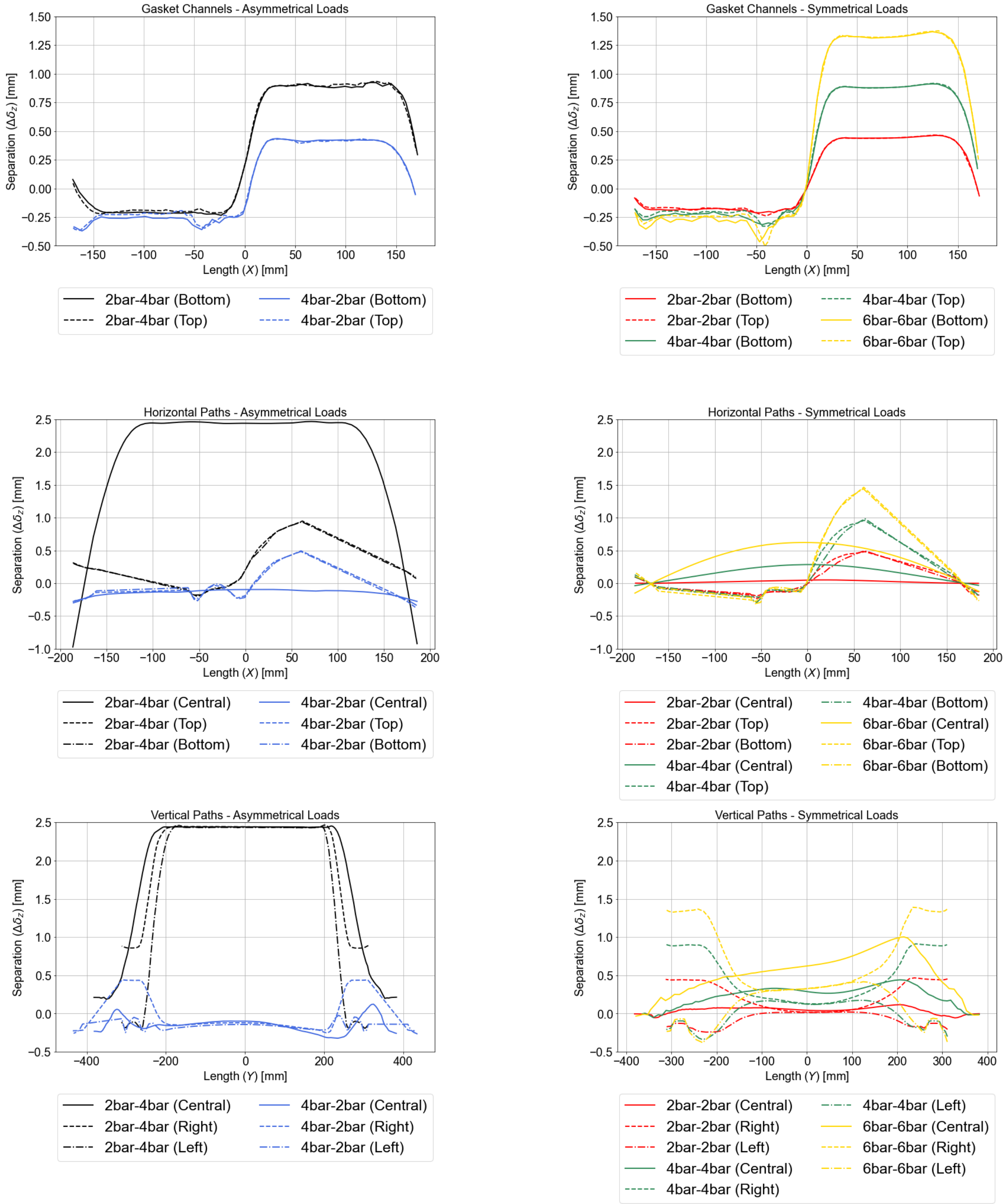

Source: Author (2023). First row: Profiles for top and bottom gasket channels; Second row: Profiles for horizontal paths between inlet and outlet ports and in the center plane; Third row: Profiles for vertical paths between inlet and outlet ports and in the center plane; Left: Asymmetrical loads; Right: Symmetrical loads.

Figure 46 and Figure 47 show the von Mises equivalent stress profiles on the paths of interest for asymmetric and symmetric loading, respectively. The profiles for the assembly step are located on the left of the figures. The profiles for the loading step are located on the right. The presentation is the same as in the previous figure, from top to bottom: gasket channels at the top, horizontal paths in the center, and vertical paths at the bottom. The minimum yield stress limit of the material is represented by the dashed red line, and the maximum yield stress limit (MARTINS et al.; 2022) is represented by the dash-dot red line.

The stress profile in the gasket channels is opposite to the displacement profile, with highest stresses found in the diagonal below the left port, where the external fluid enters the plate; this diagonal is referred to as unsupported. The results acquired in the 2bar-2bar and 4bar-2bar cases remain primarily within the elastic region, while the other cases have a significant portion of their curve positioned above the minimum yield limit. Furthermore, at 4bar-2bar, one can observe that the supported diagonal has an inverted profile, while the unsupported diagonal undergoes high stress concentrations during the loading step.

Stresses generally concentrate at the center of the plates in horizontal paths, with the exception of the 2bar-4bar loading, which displays edge concentrations at the loading step. Vertical paths, on the other hand, show varying behavior: low stress concentrations in the center of the plate (central region of the graphs) and high stress concentrations in areas nearer to the ports (right and left areas of the graphs). Again, 4bar-2bar is an exception, with considerable stress concentration at the center.

Similar to the gasket channels, the 2bar-2bar loading displays mostly elastic behavior in the vertical and horizontal paths, while higher loadings (e.g., 6bar-6bar) exhibit plasticity in significant regions.

Figure 46 - Equivalent von Mises stress profiles for paths of interest: asymmetric loads

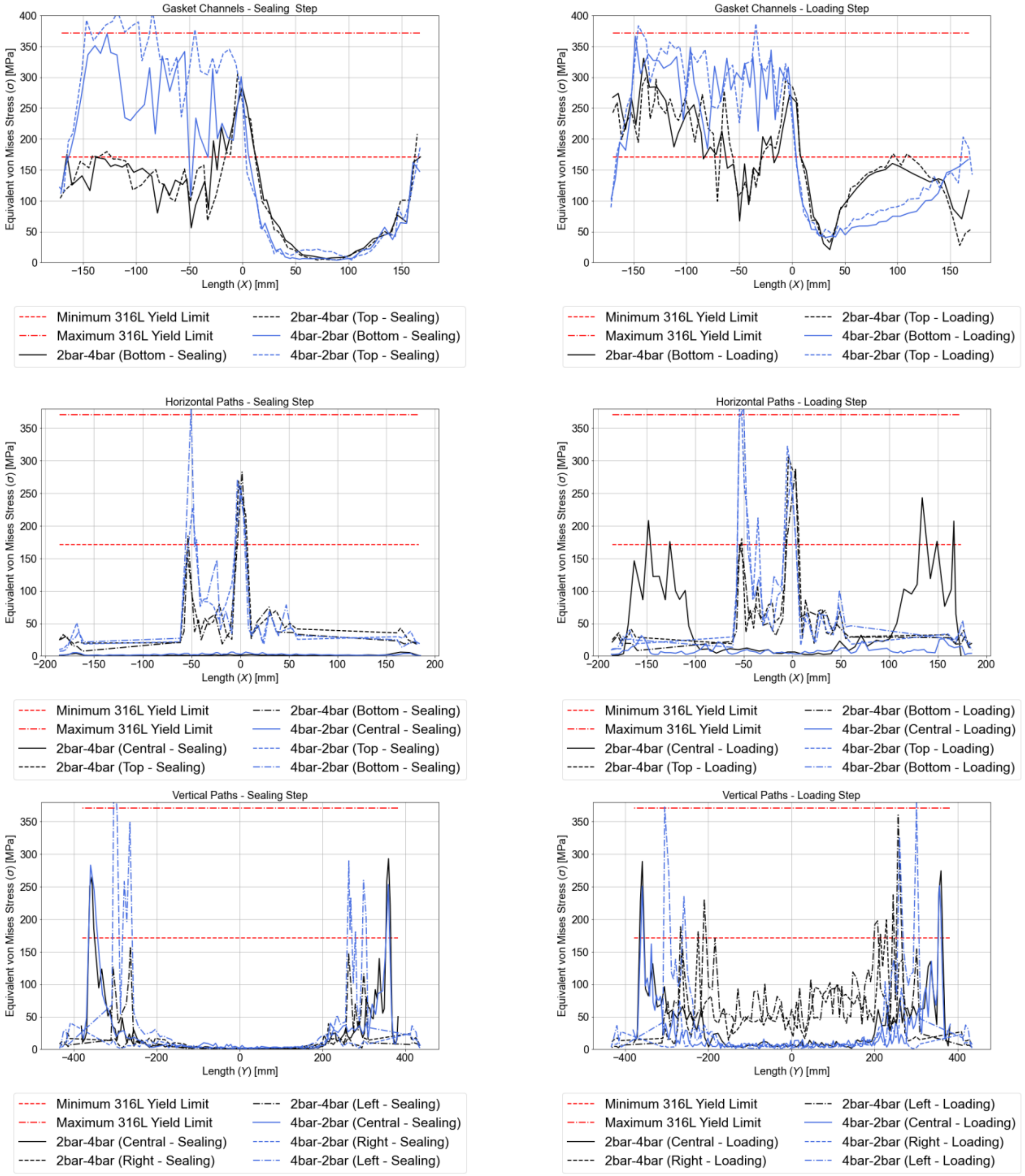

Source: Author (2023). First row: Profiles for top and bottom gasket channels; Second row: Profiles for horizontal paths between inlet and outlet ports and in the center plane; Third row: Profiles for vertical paths between inlet and outlet ports and in the center plane; Left: Sealing step; Right: Loading step.

Figure 47 - Equivalent von Mises stress profiles for paths of interest: symmetric loads

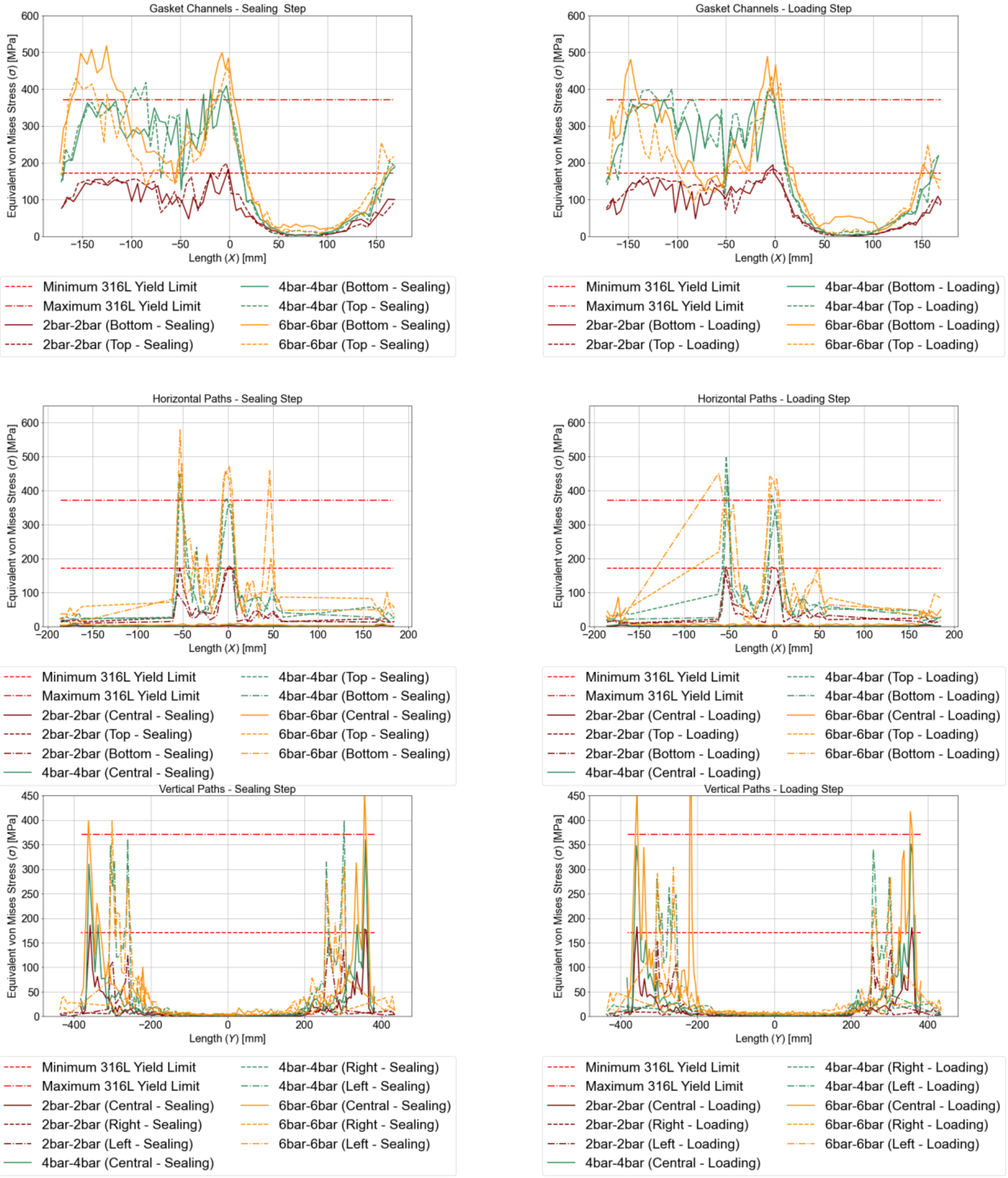

Source: Author (2023). First row: Profiles for top and bottom gasket channels; Second row: Profiles for horizontal paths between inlet and outlet ports and in the center plane; Third row: Profiles for vertical paths between inlet and outlet ports and in the center plane; Left: Sealing step; Right: Loading step.

It is necessary to evaluate the impact of the stress and strain state of the plates, obtained from the hydrostatic analysis methodology, on the working fluid.

Figure 47 was used to determine three maximum displacement values relevant to the evaluation of its influence on flow structures caused by the displacement of plates. The respective maximum displacement values for loads of 2bar-2bar, 4bar-4bar and 6bar-6bar are 0.51027 mm, 1.01770 mm, and 1.52590 mm. These values indicate an almost linear relationship between P_{IN} and $\Delta\delta_z$.

As an initial approach, the distance was defined uniformly for the entire plate profile, resulting in the generation of a new fluid volume in each of the cases. Figure 48-b illustrates the side view of the three new geometries, highlighting that the modification of one domain relative to the other is very subtle.

Figure 48 - Step indication: Uniform spaced geometries generation

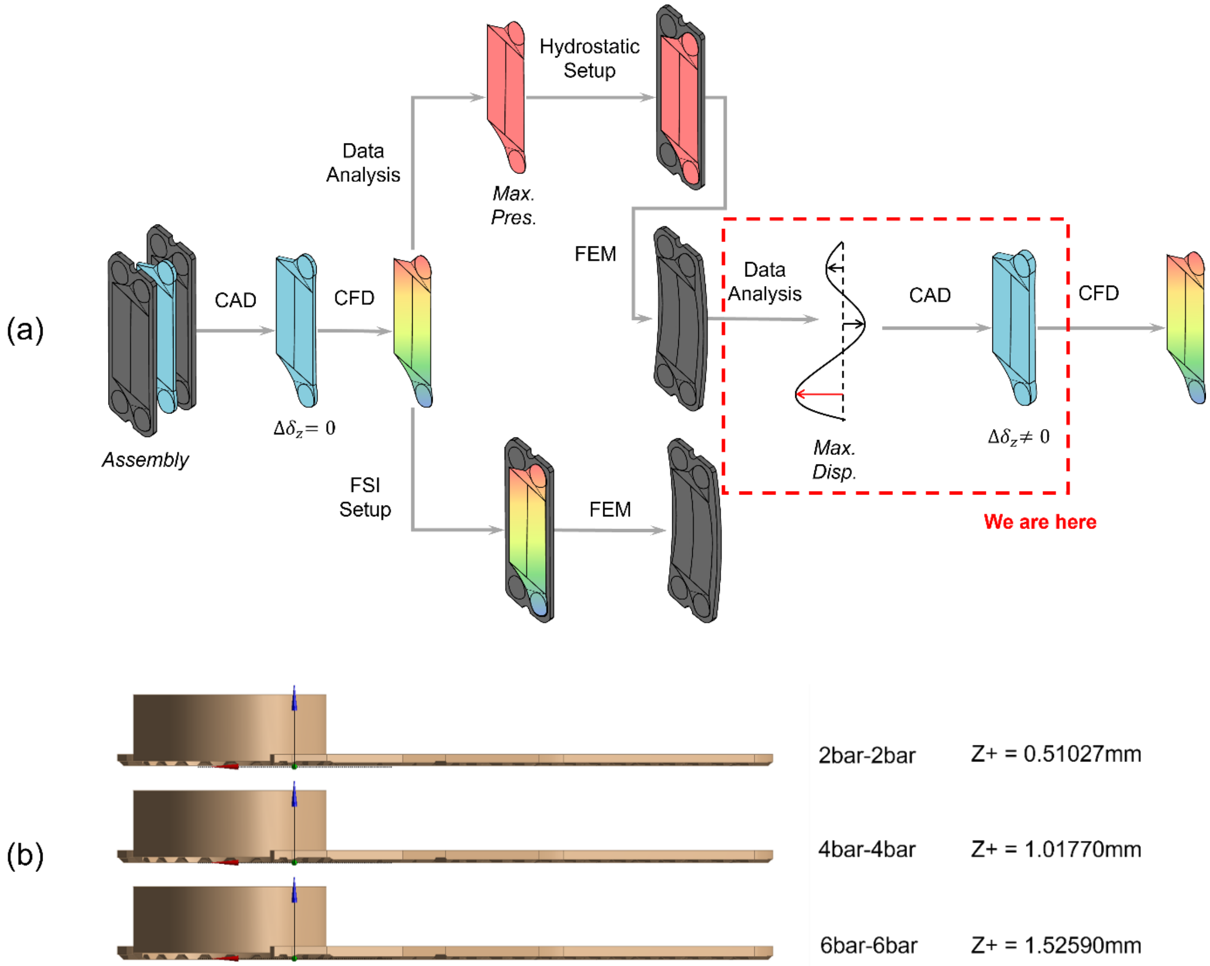

Source: Author (2023). a) Fluxogram step indication; b) Comparison of deformed geometries after uniform spacing.

4.2.2.1 Validation

To verify the obtained values in this section, the experimental data acquired with the setup shown in Part I is used to compare the widening and stretching results. The nomenclature employed to identify each monitoring point is illustrated in Figure 14. Stx and Wdx indicate points used to monitor stretching and widening, respectively.

Figure 49 shows the numerical and experimental results, taking into consideration that the experimental results were acquired with symmetrical and double loading conditions (with loading applied on both sides of the plate). On the left-hand side of the figure, the graphs include the 2bar-2bar, 4bar-4bar, and 6bar-6bar tests. On the right-hand side, the 2bar-4bar and 4bar-2bar tests are presented, where the external loading value is compared in this latter case.

Because these points are located on the periphery of a thin plate, which, as demonstrated in the previous figures, has its greatest deformation effect within its periphery, significant differences between the methods are expected. Numerical curves may diverge from the behavior presented in the experimental data when they reach 4bar and especially 6bar input values.

These pressure levels cause plasticity effects in the plate, leading to more and more deviations in the numerical results. Under symmetric loading, the results for 2bar-2bar are closer, yet weakened. The average deviation for 2bar-2bar is around 82%, with a minimum of 36% and a maximum of 126%. The average deviation for the 4bar-4bar is around 97%, with the deviation ranging between 50% and 126%. The average deviation for the 6bar-6bar is roughly 113%, and the deviation varies from 74% to 186%.

Under asymmetric loading, the deviation for 4bar-2bar is smaller, with a mean deviation of approximately 68%, which can range from 21% to 163%. The mean deviation for the 2bar-4bar configuration is approximately 76%, with a minimum deviation of 21% and a maximum deviation of 144%. As previously demonstrated, internal loading governs the stress and strain states of the plates.

Figure 49 - Widening and stretching validation

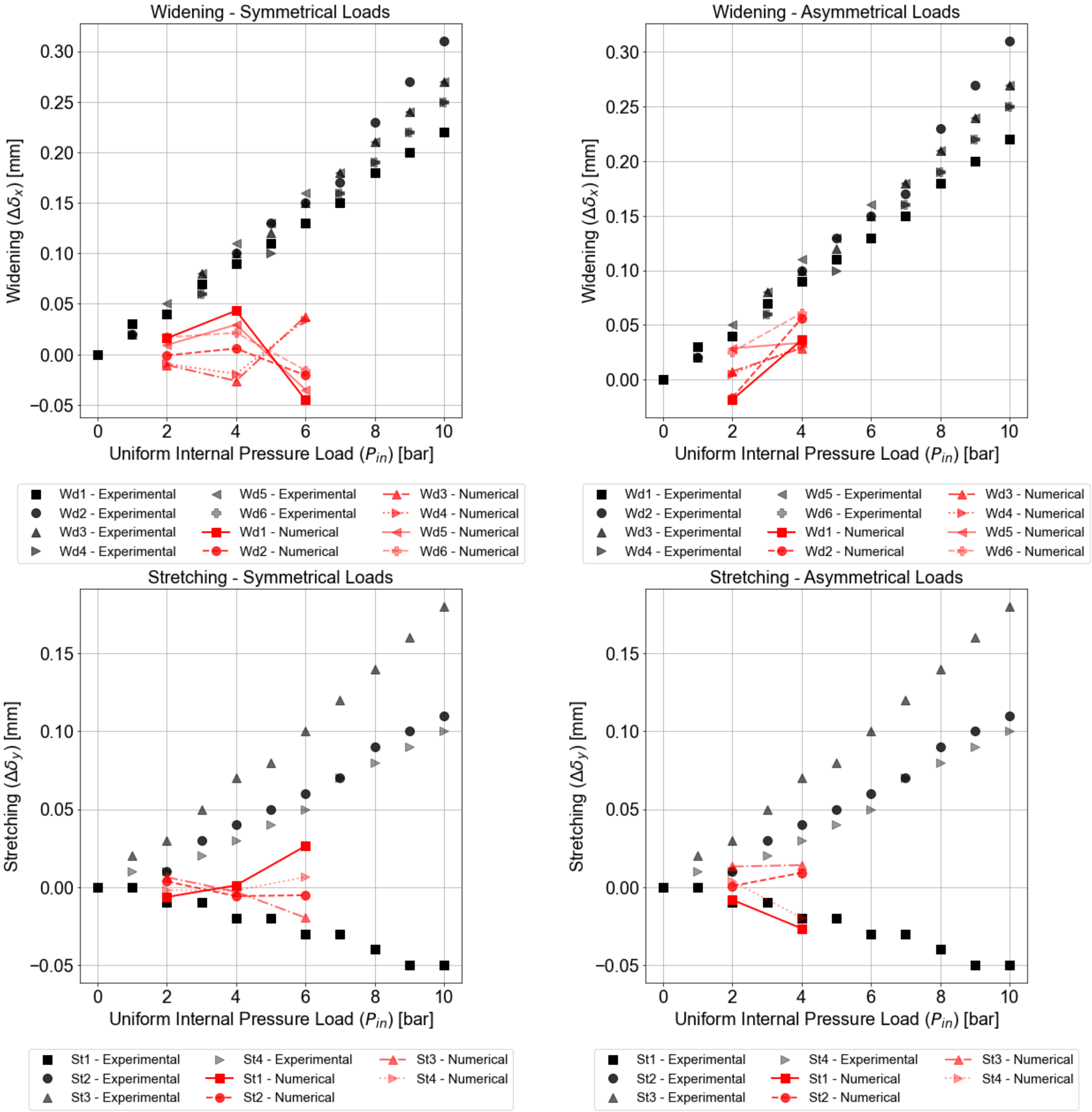

Source: Author (2023).

Initially, it may seem that such deviations are highly significant. However, considering the reference dimension used in this work, the orders of magnitude of widening and stretching displacements, even with the experimental values, amounts to only about 1.6% of the height of the corrugation.

Furthermore, it is important to highlight the difference in boundary conditions (number of plates) between the numerical and experimental methods, which can be a source of aggregate error in the analysis, as well as the potential difference between the modulus of elasticity of non-formed plates (used in the numerical method) and that of formed plates.

4.2.3 CFD results – Uniform spacing

Figure 50 - Step indication: CFD with geometries generated by uniform spacing

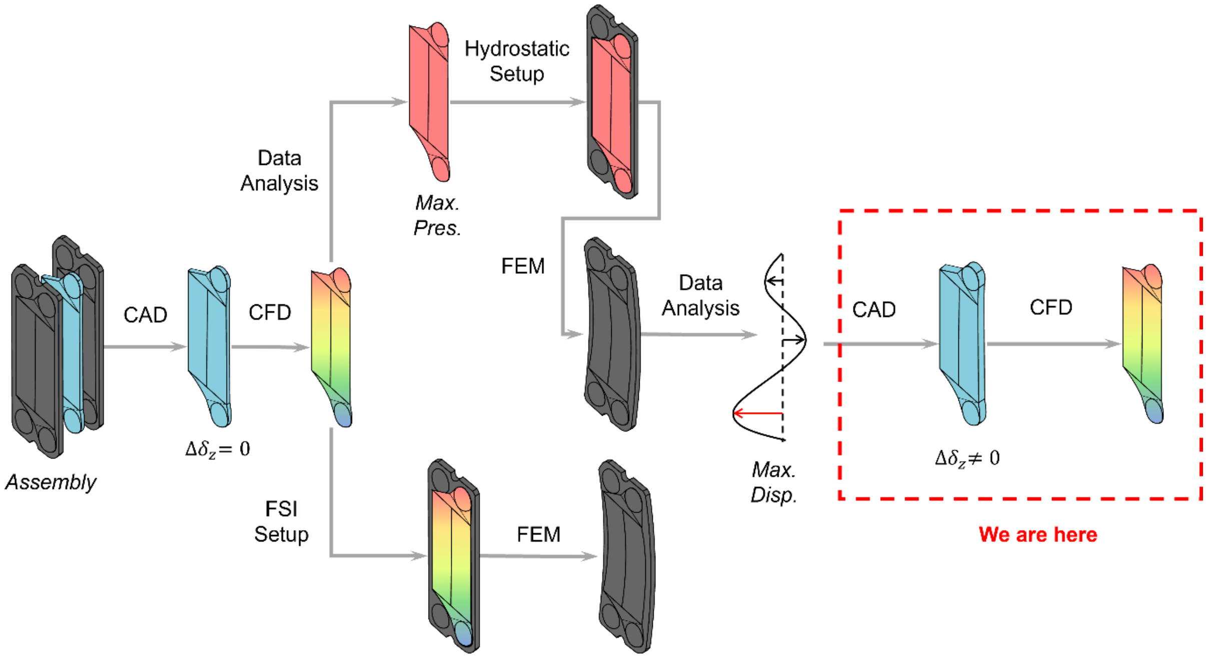

Source: Author (2023).

Figure 51 displays the velocity distribution results in the central plane of the inner fluid domain for initial separation conditions of $\Delta\delta_z$ = 0.0 mm (undeformed geometry), $\Delta\delta_z$ = 0.5 mm, $\Delta\delta_z$ = 1.0 mm, and $\Delta\delta_z$ = 1.5 mm, with an inlet flow rate at $\dot{m}_{IN}$ = 2.0 kg/s. A gradual deceleration of the fluid can be observed as the domain opens, with velocities ranging from 3.165 to 2.112 m/s in the first configuration, and substantially larger near-zero zones in the final configuration. Starting from the second configuration, it is evident that the left half of the exchange channel experiences significantly more deceleration than the right half.

Figure 51 - Distribution of velocities in the internal flow for the inlet flow rate of $\dot{m}_{IN}$=2kg/s varying the initial spacing of the plates

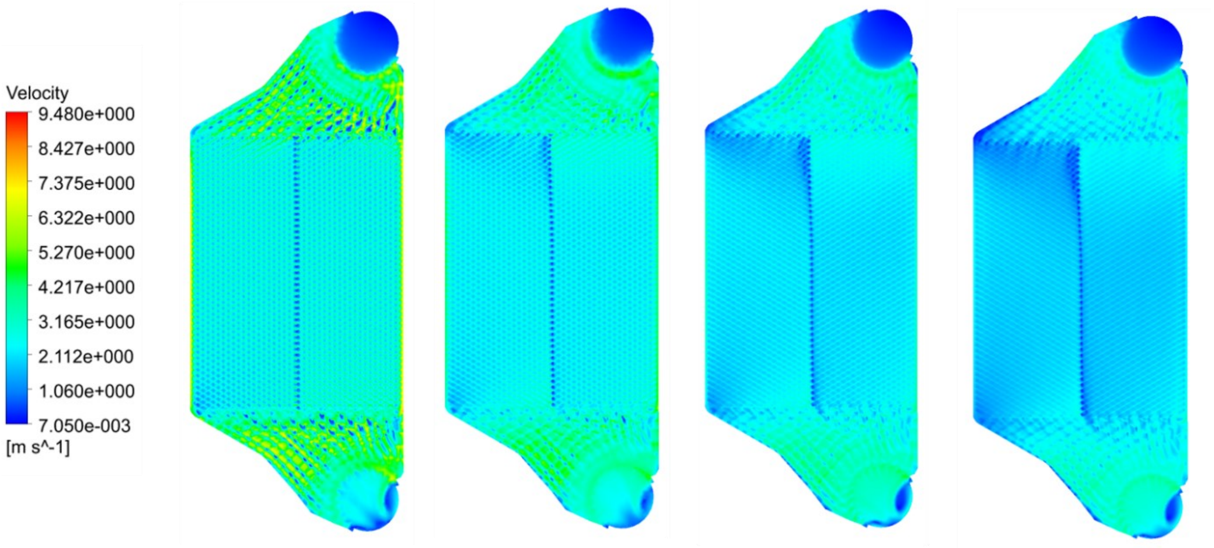

$\Delta\delta_z$ = 0.0mm $\Delta\delta_z$ = 0.5mm $\Delta\delta_z$ = 1.0mm $\Delta\delta_z$ = 1.5mm

Source: Author (2023).

Figure 52 depicts the pressure distribution on the central plane of the internal fluid domain at the same separation and inlet flow configurations. It is observed that the inlet pressure decreases by about 5 times between the first and last configuration. Moreover, the pressure drop in the domain also decreases in the same proportion.

Figure 53 establishes the point of $\dot{m}_{in}$ = 2kg/s as a comparison between the cases and it is possible to identify the sharp drop in pressure, mainly leading to the conclusion that the relationship $\Delta\delta_z$ x ΔP is not linear. As for the velocity profile, in addition to the attenuation of the magnitude of the profile there is also the lateral displacement of the peaks, indicating that they are on the face closest to the entrance of each corrugation.

Figure 52 - Distribution of pressure in the internal flow for the inlet flow rate of $\dot{m}_{IN}$=2kg/s varying the initial spacing of the plates

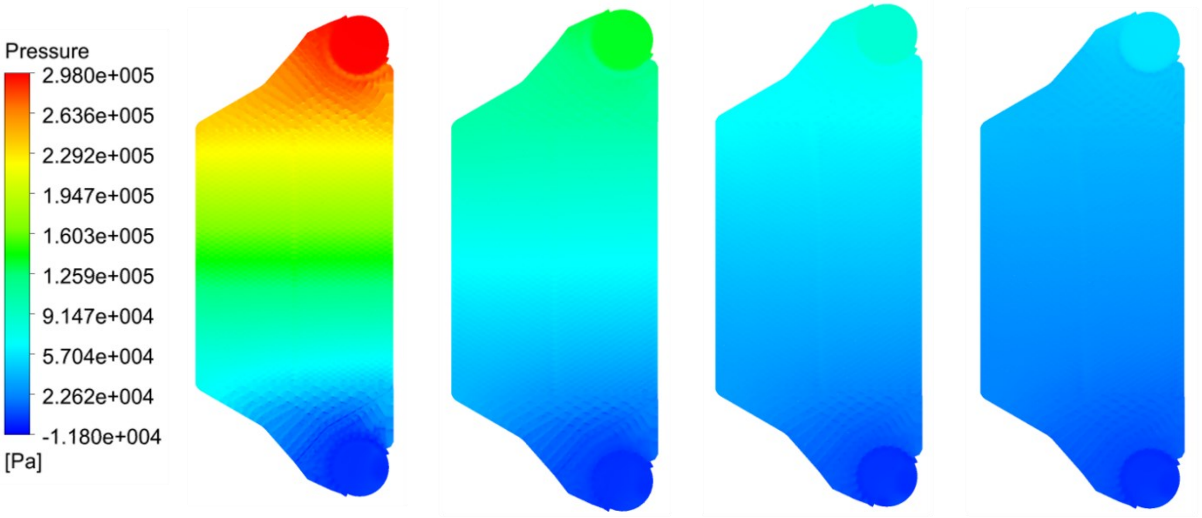

$\Delta\delta_z = 0.0$mm $\Delta\delta_z = 0.5$mm $\Delta\delta_z = 1.0$mm $\Delta\delta_z = 1.5$mm

Figure 53 - Velocity and pressure curves in the path between ports of the internal channel (Uniform Spacing - Details)

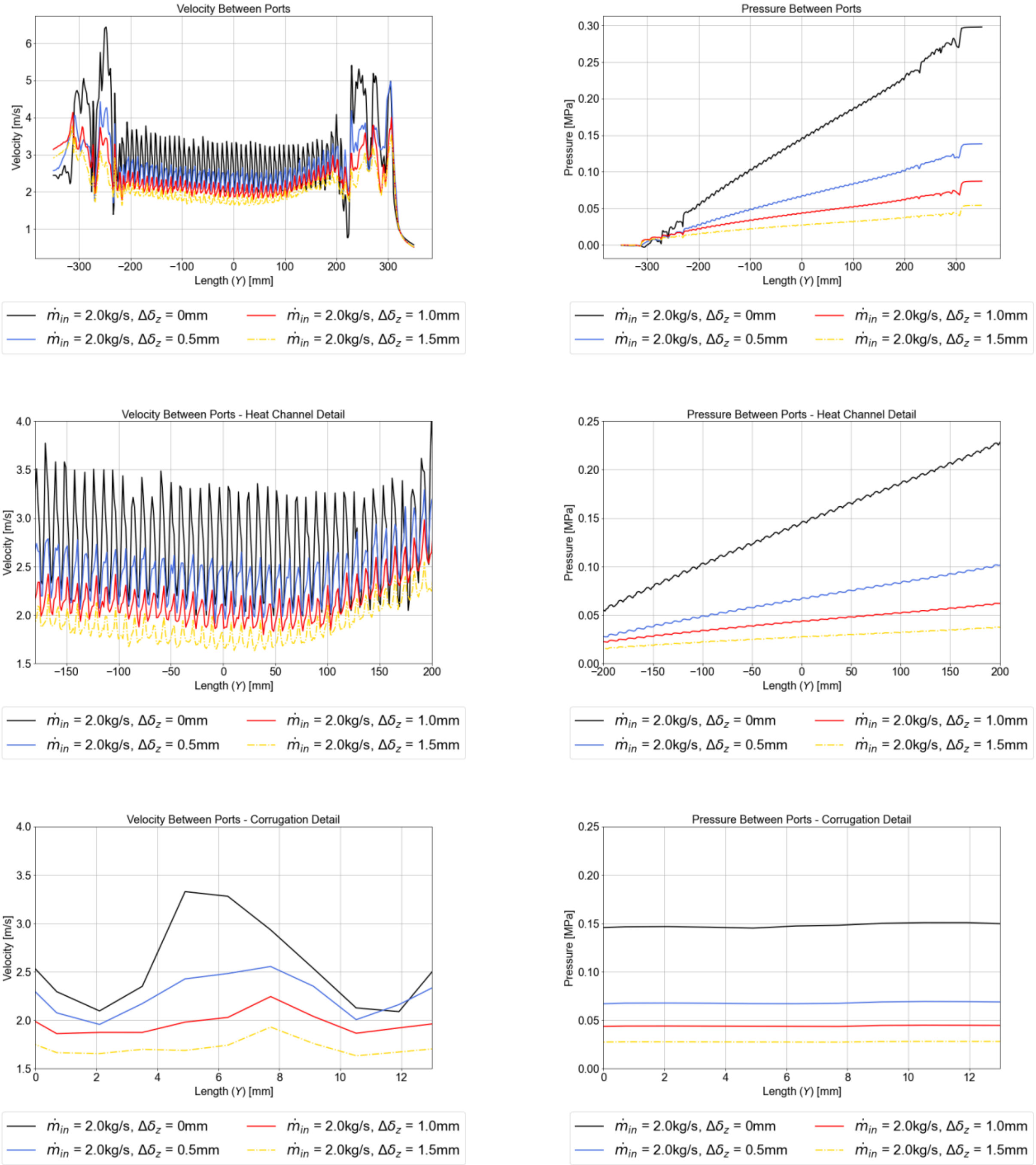

Source: Author (2023). First row: profiles for the whole plate; Second row: profiles for the heat Exchange channel; Third row: Profiles for one only corrugation; Left: Velocity profiles; Right: Pressure profiles.

Figure 54 shows the pressure drop curves of the numerical results for uniform spacing analysis compared to the experimentally collected data. It can be seen that the curve obtained for the spacing of $\Delta\delta_z$ = 0.5 mm (generated by the 2bar-

2bar condition) agree with the needle measurements for the expansion conditions of ΔP_{IN} = 2.0 bar. The higher-$\Delta\delta_z$ curves (generated by the 4bar-4bar and 6bar-6bar conditions) show larger deviations, leading to the conclusion that they could represent profiles for higher inlet pressures.

Figure 55 presents the results of mean Reynolds number within the domain and pressure drop with spacing. The conclusion previously obtained regarding the exponential relationship between the variables is evident. The graph of $\Delta\delta_z$ x ΔP shows the creation of a preferential flow path in the domain, making it insensitive to the increase of the input flow.

Figure 54 - Curves of variation of pressure drop in internal fluid domain given variation of inlet flow rate

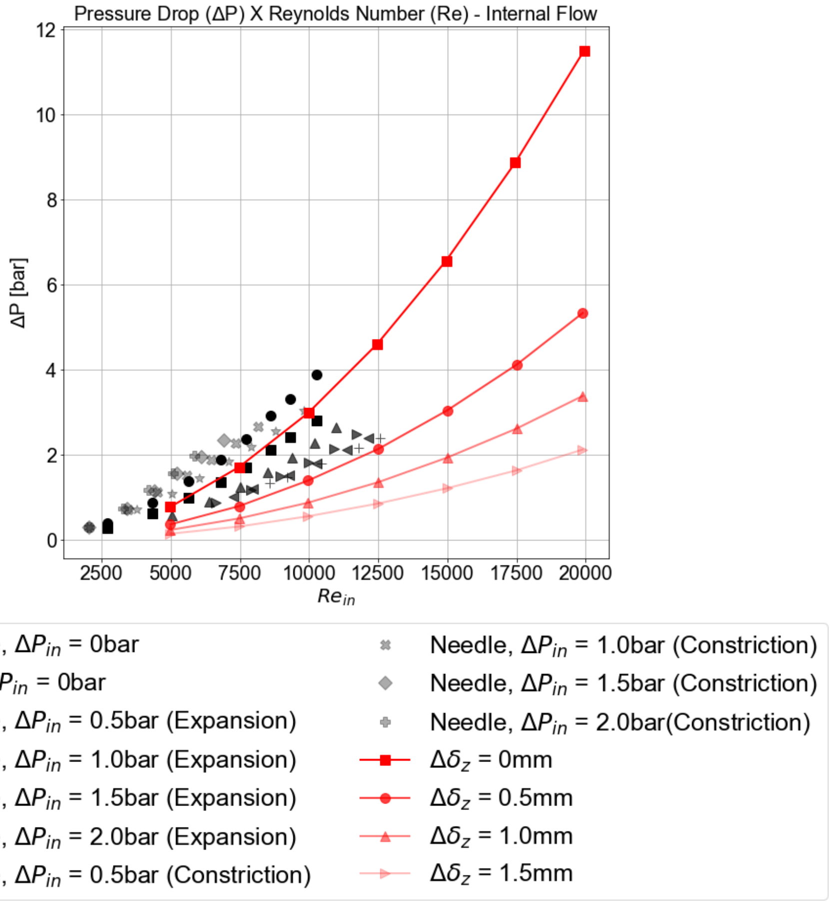

Source: Author (2023).

Figure 55 - Curves of variation of pressure drop and domain average Reynolds number in the internal fluid domain given the variation of initial distance of the plates

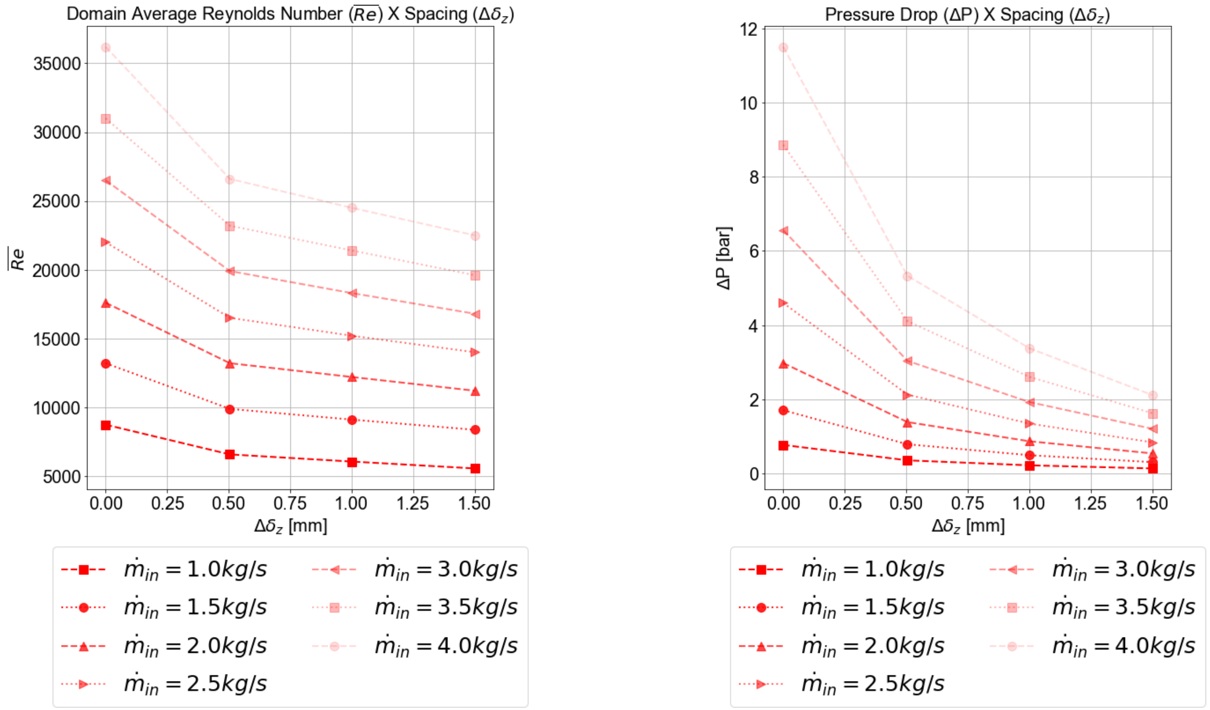

Source: Author (2023).

4.2.4 FEM results - FSI

Figure 56 - Step indication: FSI one-way FEM

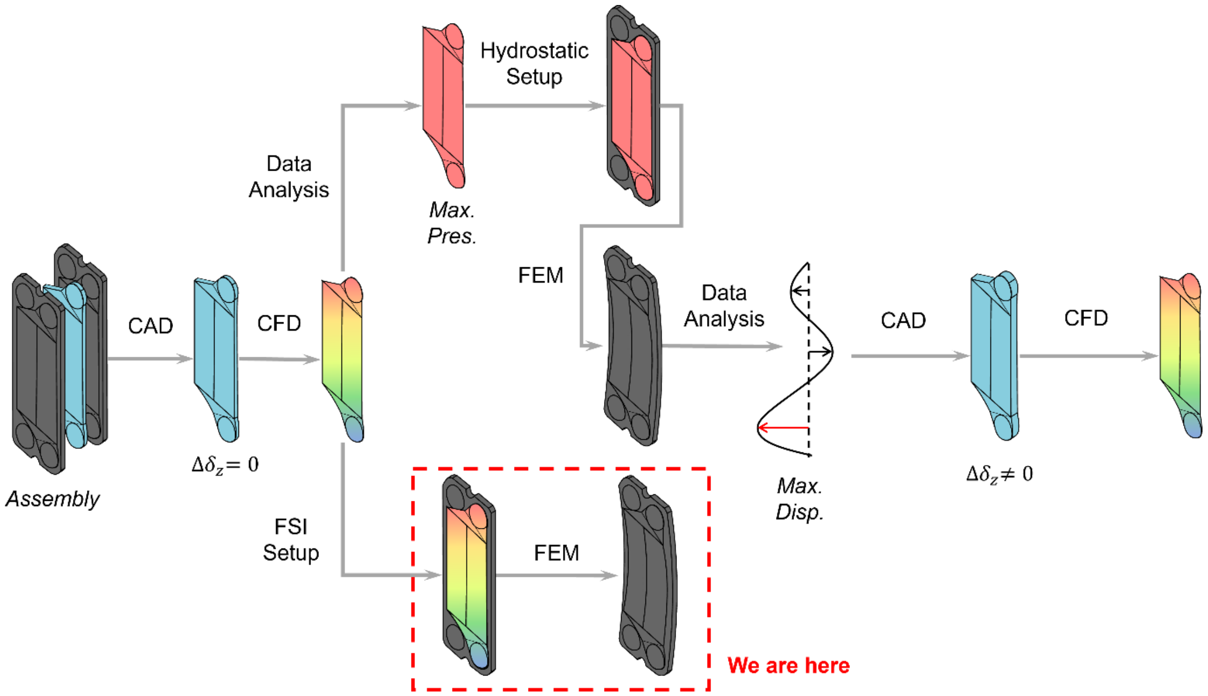

Source:Author (2023).

Figure 57 shows the pressure loads generated by the external (left) and internal (right) branches applied to the plate. Each of the loads indicates flow in one direction: the internal branch flows downwards and the external branch ascends, characterizing a countercurrent flow. The reading is always made from red, zones of higher pressure, to blue, zones of lower pressure, since the inlet is always more pressurized than the outlet.

A single case was evaluated, since the FSI analysis is time consuming (approximately 110h), and the condition chosen for comparison was that of symmetrical maximum pressures near the case 2bar-2bar. For this, the inlet conditions were chosen among the cases previously analyzed in the CFD and are the following: inlet flow rate in the internal branch of 2 kg/s, indicating a maximum pressure of 2.9 bar; and inlet flow in the external branch of 3.5 kg/s, indicating a maximum pressure of 2.2 bar.

Figure 57 - CFD loads for FSI matching

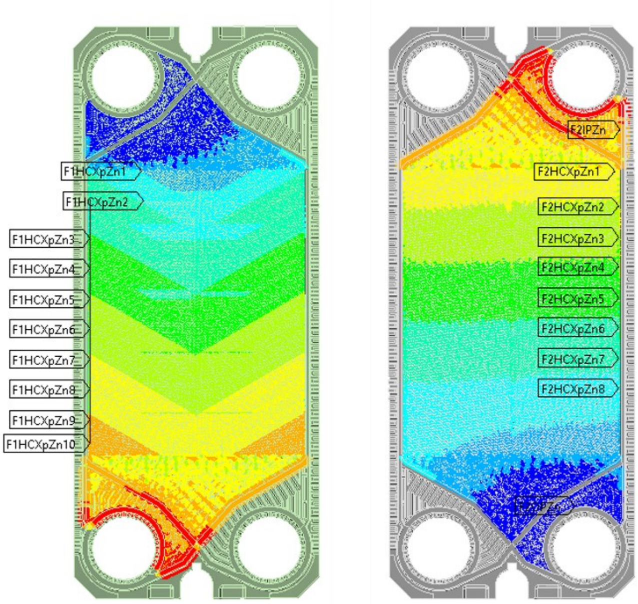

Plate 2 Plate 3

Source: Author (2023).

Figure 58 shows the directional displacement and stress fields. In comparison with Figure 42, from the hydrostatic methodology, it is possible to notice that the symmetry around the X axis is no longer present, as a result of the pressure drop in the channel. Again, the images illustrate the Z+ view of plate 3, which indicates the view of the internal branch.

In the separation figure (Figure 58-a) it is possible to notice that there is an extremely clear zone of concentration of normal displacement in the regions of the distribution gallery. As expected, in the upper part there is greater separation, a behavior caused by the proximity to the entrance port of the internal branch, and in the lower part there is greater strangulation, caused by the proximity of the entrance port of the external branch. There is a certain balance of directions in the region close to the center of the plate, with the profile undergoing deformation to follow the angle of the corrugations.

Figure 58 - Profiles of spacing, widening, elongation, assembly stress and loading stress for the 2bar-2bar loading condition under the FSI methodology.

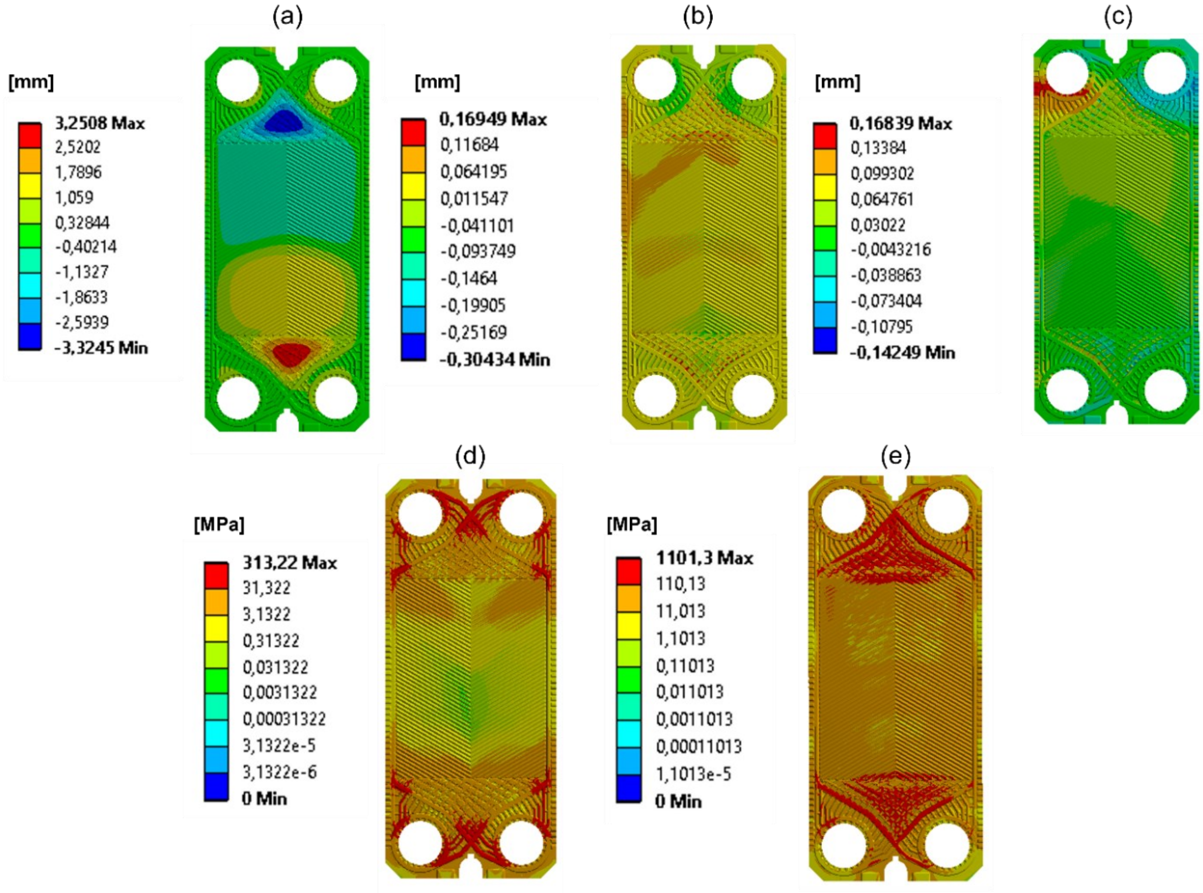

Source: Author (2023). a) Directional displacement distribution in the Z-axis, $\Delta\delta_z$ (Separation); b) Directional displacement distribution in the X-axis, $\Delta\delta_x$ (Widening); c) Directional displacement distribution in the Y-axis, $\Delta\delta_y$ (Stretching); d) Equivalent von Mises stress distribution in the sealing substep, $\sigma_{sealing}$; e) Equivalent von Mises stress distribution in the loading substep, $\sigma_{loading}$;

In the stretching profile (Figure 58-b), it is possible to notice a greater distribution of displacements, with concentration on the edges of the plate and in the transition between the distribution gallery and the thermal exchange channel. In widening (Figure 58-c) it is possible to identify the compression of the top of the distribution gallery, since the right nozzle deforms in X-, to the left, and the left nozzle deforms in the opposite direction.

The stress figures for the assembly stage (Figure 58-d) and loading stage (Figure 58-e) demonstrate behavior similar to that shown previously, with a high concentration in the gasket channels and in the distribution gallery, however, with more pronounced plastification zones in the inlet gasket channel.

Figure 59 shows the displacement (left) and loading stress (right) profiles in the same preferred paths previously shown for the Z+ direction of plate 3. Similar profiles are observed, with evidence of their asymmetry and the indication of modes of plate torsion. The zones corresponding to the distribution galleries show drastic normal deformation, however, they also correspond to the zone with the increasing evidence of plastification in the stress graphs, indicating the need for more robust modeling in these areas.

Figure 59 - Separation and stress profiles defined on paths of interest (FSI)

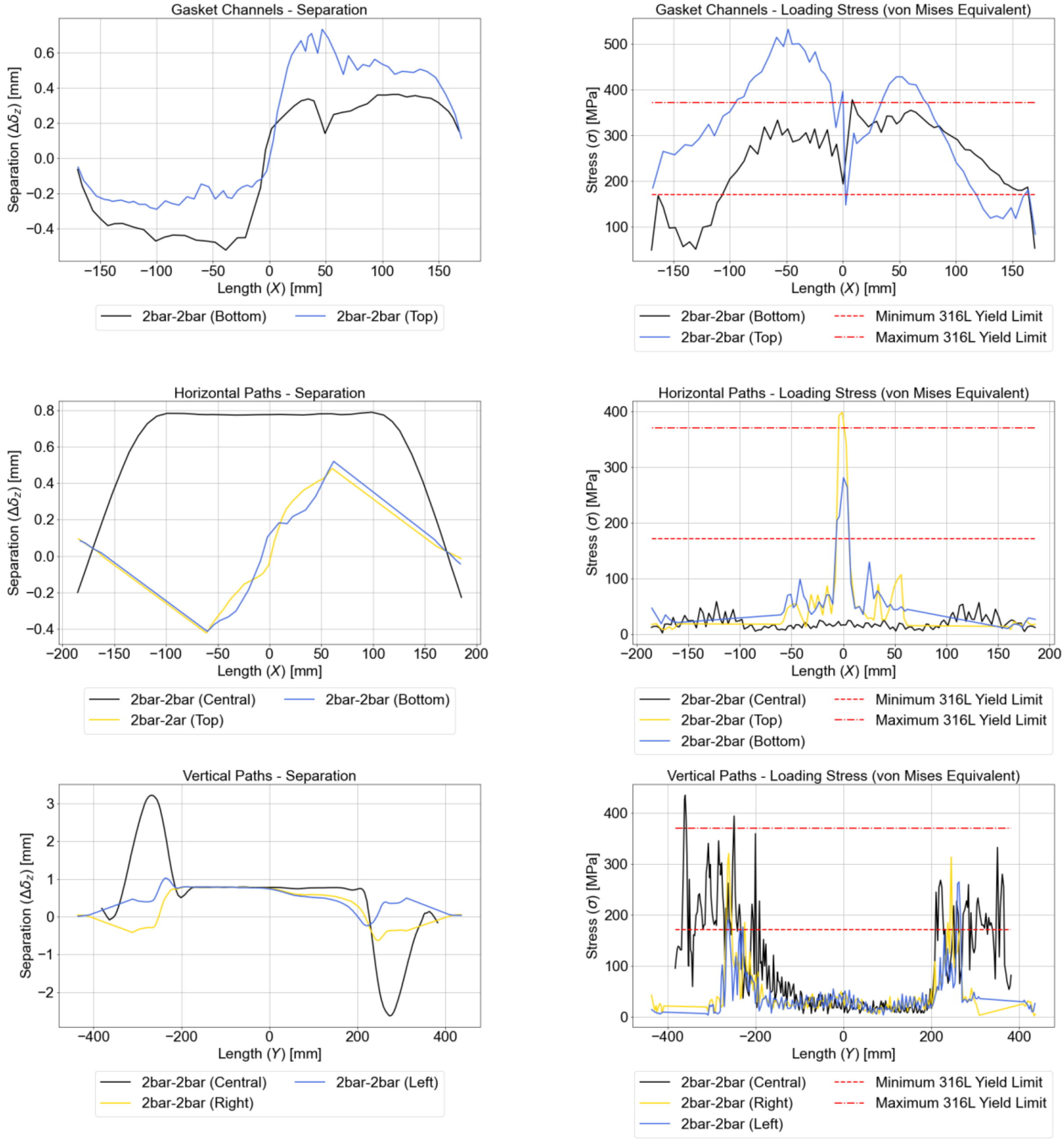

Source: Author (2023). First row: Profiles for top and bottom gasket channels; Second row: Profiles for horizontal paths between inlet and outlet ports and in the center plane; Third row: Profiles for vertical paths between inlet and outlet ports and in the center plane; Left: Separation profiles; Right: von Mises equivalent stress profiles.

Figure 60 shows the separation comparison between the 2bar-2bar loading of the hydrostatic methodology (left) and the FSI methodology (right). The legend is normalized for better comparison, with the result displacement range for the hydrostatic analysis being -0.4991 to 0.50524mm and the range for the FSI is -.3245 to 3.2508mm.

Figure 60 - Comparison between the separation profiles acquired by the hydrostatic and the FSI methods

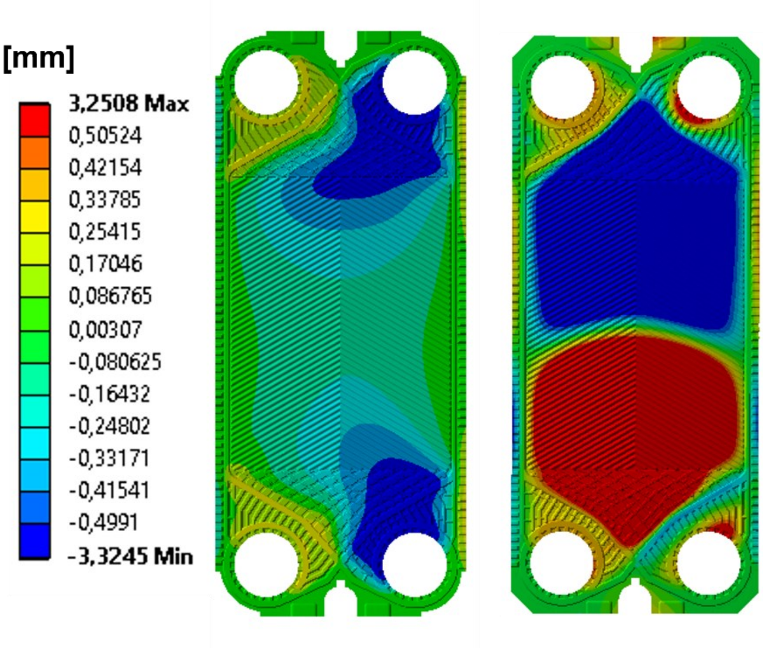

Source: Author (2023).

It is noticeable that the displacement direction experiences a drastic change upon reaching the central region of the thermal exchange channel. This occurs due to the difference in loads between both plate sides (resulting from the countercurrent flow condition) and reverses its direction when moving from the upper to the lower part.

This resulting profile may suggest a change in the elastic deformation behavior of the plate as a whole. In the hydrostatic condition, the plate behaves similarly to a pressure vessel, with deformations occurring in reduced directions. However, in the FSI condition, the increase in deformation modes prevents the profile from following a particular behavior, causing resistance from the gasket channels near the nozzles and preventing deformation in the same direction. That is, the hydrostatic model assumes the deformation profile as an inflation, at the expense of the FSI's torsional behavior.

Figure 61 displays a comparison of the two methods in relation to the preferred analysis paths previously highlighted. Objective observation depicts good agreement in the profiles, with a significant increase in curve magnitude. The distribution galleries remain critical areas of the plate. It is evident that the profile tendency exists within the hydrostatic methodology, but its magnitude is substantially underestimated, inhibiting an accurate modeling of behavior.

Table 14 - Experimental and numeric widening and stretching deviations for the 2bar-2bar load

Monitoring Point	Experimental Data [mm]	Hydrostatic Data [mm]	FSI Data [mm]	Exp. X Static Deviation [%]	Exp. X FSI Deviation [%]	Static x FSI Deviation [%]
St1	-1E-2	-6.35E-03	7.8E-3	36.53	177.98	222.86
St2	1E-2	3.68E-03	-7.2E-4	63.20	107.23	119.62
St3	3E-2	6.40E-03	-3.8E-3	78.67	112.52	158.63
St4	1E-2	-2.03E-03	-7E-5	120.30	100.74	96.34
Wd1	4E-2	1.59E-02	-8.39E-3	60.25	120.96	152.70
Wd2	4E-2	-1.07E-02	-1.2E-2	126.80	129.96	11.78
Wd3	4E-2	-1.05E-02	1.16E-2	126.25	71;02	210.84
Wd4	4E-2	-9.41E-03	1,05E-2	123.53	73.79	211.41
Wd5	5E-2	9.24E-03	-1.8E-2	81.52	135.65	292.86
Wd6	4E-2	1.68E-02	3.65E-3	58.00	90.88	78.25

Source: Author (2023).

Table 14 shows the comparison of the widening (WdX) and stretching (StX) results of the three approaches (experimental, numerical hydrostatic and numerical FSI) for the 2bar-2bar load and the deviations between them. For reference, see Figure 14.

Figure 61 - Separation and stress profiles defined on paths of interest (FSI x Hydrostatic)

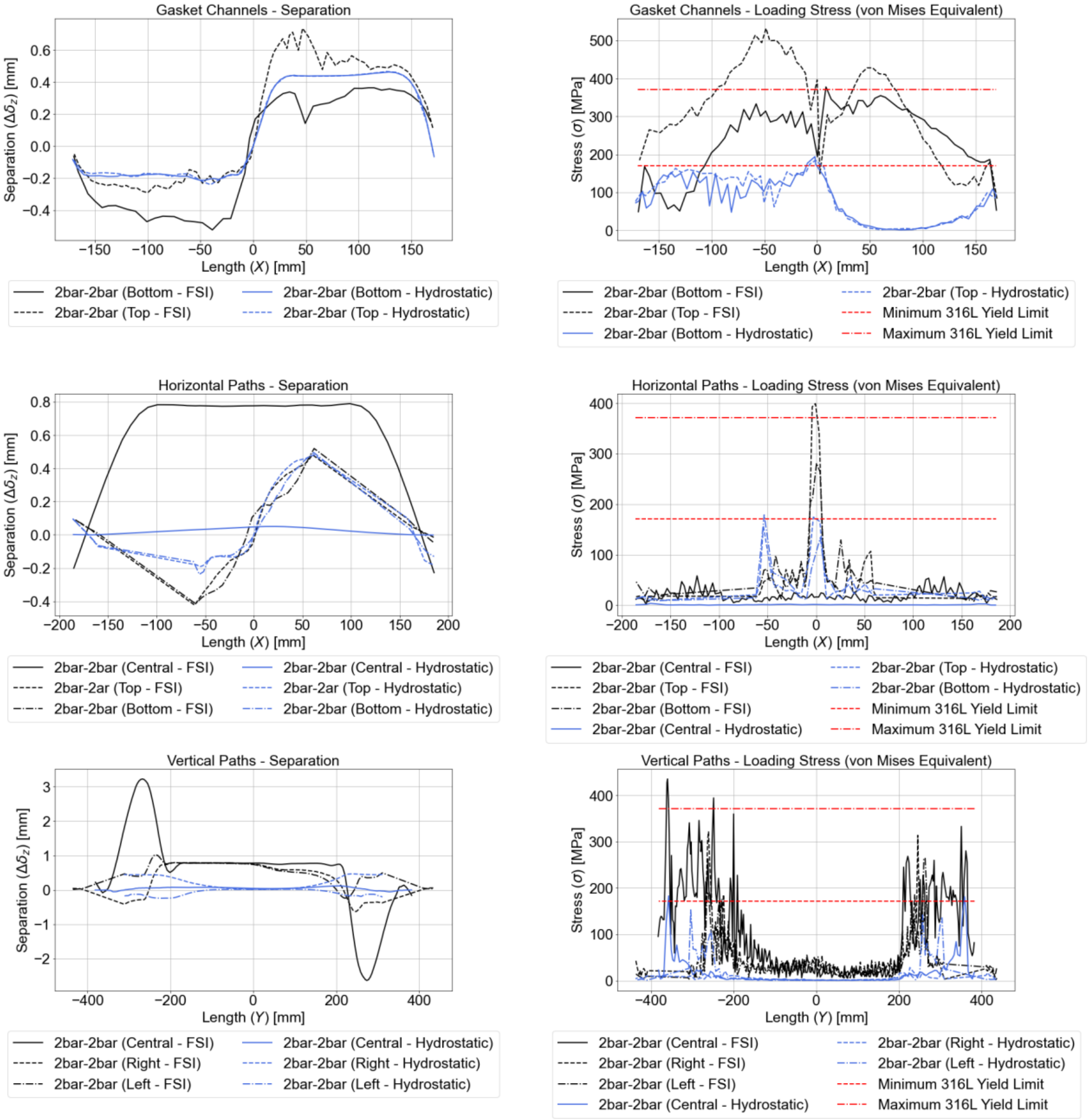

Source: Author (2023). First row: Profiles for top and bottom gasket channels; Second row: Profiles for horizontal paths between inlet and outlet ports and in the center plane; Third row: Profiles for vertical paths between inlet and outlet ports and in the center plane; Left: Separation profiles; Right: von Mises equivalent stress profiles.

4.2.5 Discussions and evaluation of methodologies

Table 15 compiles the duration and memory used in the solution of each numerical analysis presented in this work. These metrics are used to define the "computational cost" of each solution and, together with the previously presented numerical deviations, support the evaluation of the proposed methodologies.

Regarding the CFD analyses, it is possible to notice that, despite the high number of elements, they indicate relatively fast solution times, indicating that results referring to the flow do not present time restrictions in the methodology. Number of elements, number of bodies (branch passes) and input mass flow are parameters that directly influence the duration of the solution (as well as its convergence), while the allocated memory is influenced mainly by the size of the mesh.

The values related to the FEM analyzes indicate proportional dependence of the solution time in relation to the applied load. This happens because the problem presents non-linearities, which leads the software to section the load linearly to avoid divergences. Therefore, the greater the load, the greater the number of sections and the longer the time to reach the final value. Also, asymmetric problems lead to greater complexities of the contact state between the plates, increasing the solution time. The allocated memory is again dependent on the solution mesh.

The FSI problem, by considering both numerical methods, demands greater memory allocation, applies more complex loads and results in less linear displacements, leading to the need for more solution time. It is important to note that no FEM analysis could be performed on a machine with less than 64GB of RAM and the FSI analysis, specifically, had to be developed completely on a cluster (see Table 12). The change in body type was crucial for the expediency of the results, going from an analysis of approximately 25 days (solid body) to an analysis of approximately 4.5 days (surface body).

Table 15 - Comparison of solution time and allocated memory

Geometry of analysis	Average solution time [h:min:s]	Average allocated memory [GB]
CFD Intern	16:06:50	4385.76
CFD Extern	29:04:34	5688.69
CFD Intern 0.5mm	15:55:47	4328.64
CFD Intern 1.0mm	15:32:21	4523.87
CFD Intern 1.5mm	14:50:32	4674.83
Hydrostatic 2bar-2bar	0:55:37	60.572
Hydrostatic 4bar-4bar	3:59:00	61.131
Hydrostatic 6bar-6bar	5:23:00	94.21
Hydrostatic 2bar-4bar	26:18:00	64.643
Hydrostatic 4bar-2bar	22:18:00	78.095
FSI FEM 2bar-2bar	109:26:00	92.517

Source: Author (2023).

In addition to numerical analysis, it is important to consider intermediate tasks when evaluating the performance of the presented methods. Experimental validation and geometric modeling are the most costly and precision-dependent subtasks within their workflow. The undeformed geometry should preferably be obtained from the manufacturer (derived from the CAD from which the stamping molds originate) or by 3D scanning. Abrupt simplifications of the geometry can lead to significant deviations in the results, indicating a critical source of error. Experimental validation, although optional, supports and guides the numerical analyses, giving confidence to the data presented.

The modeling of intermediate geometries (uniform spacing or deformed geometry derived from the FSI structural analysis), the definition of the fluid-structural interfaces, and the simulation setup showed common time costs with a minimum of 24h and a maximum of approximately 120h for the present work. The hydrostatic analysis also shows the need for user intervention to analyze and define the spacing peaks necessary for the application in new fluid volumes, indicating that although it requires less hardware and solution time, it presents more substeps in its development. In contrast, the FSI analysis requires less user interaction but a longer solution time.

Regarding the effectiveness of the methods, the hydrostatic analysis showed a satisfactory range of deviations for the CFD analysis, with good agreement in the behavior of the pressure curves for symmetrical problems. However, caution is recommended when applying such methodologies in asymmetric cases, both for undeformed geometry and for geometries with uniform spacing.. It is expected that the application of non-homogeneous displacement profiles (fruit of the FSI analysis) will bring a more comprehensive modeling.

In the FEM application, the experimental validation proved to be too limited for comparison, making it necessary to develop a new setup to capture more displacement/deformation axes. In the comparison of methods, the hydrostatic analysis could not capture the elastic deformation profile of the plate along its longitudinal axis (flow direction), since it did not take into account the pressure drop. In addition, it was possible to identify the critical load zones, such as the sealing channels and the fluid distribution gallery, mainly in the area where there is no support on either side of the plate in the inlet nozzle. The FSI analysis showed a greater variety of deformation modes of the plates, but due to the limitations of the simplifications used in the FEM, the critical zones could not be evaluated quantitatively.

Regarding the modeling used, it was possible to identify the need to apply plasticity models in the FEM, to improve the elastic support modeling (preferably for a model that effectively applies the gasket geometry within the FEM), and to develop a more rigorous work of mesh optimization. For CFD analysis, it is recommended to use a more robust turbulence model (taking into account the inherent trade-off associated with FSI analysis) and to use non-uniformly deformed geometries.

It can be noted that the hydrostatic analysis, even if simplified, is recommended for preliminary analyses with low flow (and therefore low mechanical load) to understand the flow structures and the stress and strain states of GPHE exchangers, using more accessible hardware and software and requiring less expertise from the user.

The FSI method, on the other hand, is recommended for more rigorous evaluations, which may require more computing power and are performed by more experienced users, but use more rigorous boundary condition modeling than those presented to achieve better results..

5 CONCLUSION

Faced with the problem of elastic deformations in corrugated GPHE plates, caused by fluid-structural interactions, this work has evaluated two numerical approaches to study the phenomenon, taking into account their performance in relation to experimental data and the added cost of each methodology.

Regarding the behavior of the object of study, both the experimental data obtained in hydrostatic and hydrodynamic benches and the numerical data indicated the presence of influential elastic deformations in the behavior of the flow. The experimental data show an asymmetry between internal branches (far from the cover plates) and external branches (close to the cover plates) in terms of their pressure drop and, consequently, the friction factor.

The main characteristics of the flow are the high recirculation at the outlet, the sudden pressure drop between the inlet distribution gallery and the heat exchange channel, and the stagnation zones created by the contact points (relative to the chevron angle of the plate). The CFD analysis of the geometries generated with uniform spacing showed that the opening of the plates, however small it may be considered, has a great influence on the thermo-hydraulic performance, linearly decreasing the pressure value and the friction factor. It was not possible to define a single expression for the friction factor in all three scenarios (experimental data, numerical data of the internal branch and numerical data of the external branch), which indicates that the amount of restrictions and simplifying assumptions influence each branch in a different way and magnitude.

It was possible to conclude that the hydrostatic analysis (with the application of uniform spacing) is an efficient approach to evaluate the flow structures, since it showed a good agreement with the experimental data obtained in a hydrodynamic bench, both for the original geometry and for the geometries to which uniform spacing was applied. As a limitation, the hydrostatic method is not able to model asymmetric flow conditions, which differ significantly from the real behavior.

The structural behavior showed greater divergences in both methods. The cause for this result has several sources: the experimental data provided for comparison include the less dominant deformation modes in the plate, making an efficient validation impossible; the FEM takes into account a group of simplifying assumptions and peripheral modeling to the relatively extensive set of main equations, increasing the deviation of the numerical model with respect to the real phenomenon, such as the elastic support of the gasket and the plasticity model of the material, and the high computational cost added to the modeled body type and to the method solution makes more rigorous mesh analysis and optimization impractical.

Taking this into account, the main structural behaviors of the plates found in this study were the influence of the stress state in the assembly stage on the final result of the FEM; the criticality of the distribution zone (mainly the surrounding sealing channel), which concentrates the stress peaks after loading; the plastification of the contact points and the infeasibility of evaluating the stress concentration zones with the linear-elastic model of the material; the predominance of separation in the deformed state to the detriment of stretching and widening, with differences of up to 10 times in the magnitude of the displacements; the identification of torsional profiles around the plate axes, indicating a non-uniform elastic deformation behavior and the apparent predominance of the internal loading of the pack in the phenomenon.

The hydrostatic methodology, although effective in identifying stress concentration zones and approximating the displacement profiles, showed limitations with respect to the torsional modes related to the fluid pressure drop and underestimated the displacement values. The FSI methodology produced results with more complex behavior, identifying the change of deformation direction in the center of the corrugated plate, but its deviations with respect to the experimental data were much greater than those of the hydrostatic methodology.

In terms of cost, the FSI one-way resulted in high memory allocation and high solution time, indicating that to reach its best capacity, greater investment in hardware and software is required. On the other hand, this method requires less user intervention, which saves time on intermediate tasks. The hydrostatic method, on the other hand, obtains results faster and with less computational cost, but requires greater user involvement throughout the process.

To obtain the results described in this work, high rigor in obtaining CAD models, fidelity in experimental testing, and availability of robust hardware are recommended. For future work, the following modifications and analyses are indicated:

- Application of material plasticity models;
- More robust modeling (preferably direct) of the gasket;
- Mesh optimization for local refining;

- Non-uniform profile application in the fluid domain, or acquisition of the deformed geometry generated by the FSI;
- Application of a more robust turbulence model;
- Analysis of heat transfer in the device;
- Application of thermal stresses on the plate;
- Variation of the initial spacing of the plates in the FEM analysis;
- Plate thickness variation;
- Variation of plate material;
- Plate model variation (size and corrugation pattern);
- Application of the FSI Two-ways methodology (feedback).

REFERENCES

ADOLFSSON, M.; RASHID, S. **Life Cycle Assessment and Life Cycle Cost of Heat Exchangers**: a case for inter terminals sweden ab located in port of gothenburg. 2016. 62 f. Master's dissertation - Industrial Ecology, Chalmers University Of Technology, Gothenburg, 2016.

ALFA LAVAL. **FrontLine**. Available at: https://www.alfalaval.com.br/produtos/transferencia-de-calor/trocadores-de-calor-a-placa/trocadores-de-calor-a-placas-gaxetado/frontline/. Last access: 26 sep. 2022.

ALVES FILHO, A. **Elementos Finitos:** A Base da Tecnologia CAE. São Paulo: Editora Érica, 2000.

American Society of Mechanical Engineers. **ASME Boiler and Pressure Vessel Code. Section II**: Materials. Part D. 2010.

American Society of Mechanical Engineers. **ASME Boiler and Pressure Vessel Code, Section VIII, Division 1:** Rules for Construction of Pressure Vessels, Appendix 2, (2017)

ANDERSON, J. D. **Computational Fluid Dynamics:** The Basics with Applications. New York: Mcgraw-hill, 1995. (McGraw-Hill Series in Mechanical Engineering).

ANSYS. **ANSYS Documentation**. 2023.

BARDINA, J. E.; HUANG, P. G.; COAKLEY, T. J.. **Turbulence Modeling, Validation, Testing, and Development**. Moffett Field: NASA, 1997.

BECKEDORFF, L.; NIEUWENHUIZEN, R.; BOLWERK, T.M.A.J.; MONTEIRO, A.S.; PAIVA, K.V. de; KUERTEN, J.G.M.; GELD, C.W.M. van Der; OLIVEIRA, J.L.G.. Flow statistics in plate and shell heat exchangers measured with PTV. **International Journal Of Heat And Fluid Flow**, [S.L.], v. 79, p. 108461, out. 2019. Elsevier BV. http://dx.doi.org/10.1016/j.ijheatfluidflow.2019.108461.

BUNGARTZ, H.; MEHL, M.; SCHÄFER, M. Fluid Structure Interaction II: modelling, simulation, optimization. Munich: Springer, 2010.

ÇENGEL, Y.; BOLES, M. **Thermodynamics: An Engineering Approach**. 8. ed. S.L: McGraw-Hill Science/Engineering/Math, 2011.

COOK, R. D. **Finite Element Modeling for Stress Analysis.** New York: John Wiley & Sons, Inc., 1995.

DONATI, D. C. X.; SANTIAGO, R. S. de; POSSAMAI, T. S.; OBA, R. FLUID-STRUCTURE ANALYSIS OF PSHE HEAT EXCHANGER PLATES BY NUMERICAL APPROACH. In: INTERNATIONAL CONGRESS OF MECHANICAL ENGINEERING, 26., 2021, Florianópolis. **Proceedings [...] .** Florianópolis: ABCM, 2021.

HAASE, W.; WINDZELL, B.; SELMIN, V. Progress in Computational Flow-Structure Interaction: results of the project unsi, supported by the european union 1998-2000. Berlin: Springer, 2002.

INCROPERA, F. et al. **Fundamentos de Transferência de Calor e Massa.**6. ed. [s.l.]: John Wiley & Sons, 2007.

JIN S.; HRNJAK P., Effect of end plates on heat transfer of plate heat exchanger. International Journal of Heat and Mass Transfer. Urbana, p. 740-748. nov. 2016.

KAKAÇ, S.; LIU, H.; PRAMUANJAROENKIJ, A. **Heat Exchangers**: selection, rating, and thermal design. 4. ed. Boca Raton: Crc Press, 2020.

KHAIL, A. A.; ERISEN, A.. Heat transfer and performance enhancement investigation of novel plate heat exchanger. **Thermal Science And Engineering Progress**, [S.L.], v. 34, p. 101368, set. 2022. Elsevier BV. http://dx.doi.org/10.1016/j.tsep.2022.101368.

LI, K.; WEN, J.; WANG, S.; LI, Y.. Multi-parameter optimization of serrated fins in plate-fin heat exchanger based on fluid-structure interaction. **Applied Thermal Engineering.** [S.L.], p. 385-402. abr. 2020.

LYCHAKOV, V. D.; BALUNOV, B. F.; GUSEW, S.; SHCHEGLOV, A. A.; MATYASH, A. S.; STARUKHINA, K. S.; ZAYTSEV, A. V.. Gasketed plate heat exchangers breathing effect. **Iop Conf. Series: Journal Of Physics**, [S.L.], v. 891, nov. 2017.

MALISKA, C. R. **Transferência de Calor e Mecânica dos Fluidos Computacional:** Fundamentos e Coordenadas Generalizadas. 2. ed. Florianópolis: LTC, 2017.

MARTIN, H., A theoretical approach to predict the performance of chevron-type plate heat exchangers. Chemical Engineering And Processin, Karlsruhe, v. 35, p.301-310, 1996

MARTINS, G.S.M.; SANTIAGO, R.S.; BECKEDORFF, L.E.; POSSAMAI, T.S.; OBA, R.; OLIVEIRA, J.L.G.; OLIVEIRA, A.A.M. de; PAIVA, K.V.. Structural analysis of gasketed plate heat exchangers. **International Journal Of Pressure Vessels And Piping**, [S.L.], v. 197, p. 104634, jun. 2022. Elsevier BV. http://dx.doi.org/10.1016/j.ijpvp.2022.104634.

MOUBACHIR, M.; ZOLÉSIO, J. **Moving Shape Analysis and Control**: applications to fluid structure interactions. Boca Raton: Chapman & Hall, 2006.

MUDHAFAR, M. A.H.. Numerical study of two-phase flow in multi-channels plate heat exchanger. **International Communications In Heat And Mass Transfer**, [S.L.], v. 138, p. 106380, nov. 2022. Elsevier BV. http://dx.doi.org/10.1016/j.icheatmasstransfer.2022.106380.

MULEY A.; MANGLIK, R. M., Enhanced heat transfer characteristics of singlephase flows in a plate heat exchanger with mixed chevron plates, J. Enhanced Heat Transfer, 4(3), 187, 1997.

NASCIMENTO, R. S. do. **ANÁLISE DE COMPORTAMENTO ESTRUTURAL DE PERMUTADORES DE PLACAS.** 2013. 140 f. Dissertação (Mestrado) – Curso de Pós-graduação em Engenharia Mecânica, Universidade Federal do Rio de Janeiro, Rio de Janeiro, 2013

NGUYEN, D. H.; KWEON, B.; KWON, J.; KIM, T.; WONGWISES, S.; AHN, H. S.. Numerical study on novel airfoil corrugated plate heat exchanger: a comparison with commercial type and geometrical parameter analysis. **International Journal Of Heat And Mass Transfer**, [S.L.], v. 195, p. 123119, out. 2022. Elsevier BV. http://dx.doi.org/10.1016/j.ijheatmasstransfer.2022.123119.

NISHIMURA, K. ODAGAWA, Y. HAYASHI, S. **Newly Developed HNBR/ZMA Composite for Heavy Load and Heat Resistance Roll Application**. In: American Chemical Society 152nd National Meeting, ZEON Corporation Research & Development Center , Kawasaki, Japan. 1997.

PAÏDOUSSIS, M. P. Fluid-Structure Interactions: slender structures and axial flow. San Diego: Academic Press, 1998. 1 v.

PATANKAR, S. V. **Numerical Heat Transfer and Fluid Flow.** [s. L]: Taylor & Francis, 1980.

PELLICCIONE, A.S. et al. Failure analysis of a titanium plate heat exchanger – Mechanical fatigue. **Engineering Failure Analysis**, [s.l.], v. 105, p.1172-1188, nov. 2019. Elsevier BV. http://dx.doi.org/10.1016/j.engfailanal.2019.07.059

SCHLICHTING, H.; GERSTEN, K. **Boundary-Layer Theory**. 9. ed. Heidelberg: Springer Berlin, 2017.

SHAH, R.K., FOCKE, W. W.,**Plate Heat Exchangers and Their Design Theory**. Washington D. C., Hemisphere Publishing, 1988.

SHAH, R. K.; SEKULIC, D. P. **Fundamentals of Heat Exchanger Design**. New Jersey: John Wiley & Sons, 2003.

TASCHECK, B.L.; DONATI, D.C.X.; POSSAMAI, T.S.; OBA, R.; BECKEDORFF, L.; MONTEIRO, A.S.; OLIVEIRA, J.L.G.; PAIVA, K.V.. Numerical analysis of hydrodynamic and thermal characteristics of three inside channel configurations of a plate and shell heat exchanger (PSHE). **Chemical Engineering Science**, [S.L.], v. 264, p. 118167, dez. 2022. Elsevier BV. http://dx.doi.org/10.1016/j.ces.2022.118167.

TENNEKES, H.; LUMLEY, J. L.. **A First Course in Turbulence**. Cambridge: The MIT Press, 1972.

VERSTEEG, H. K.; MALALASEKERA, W.. **An Introduction to Computational Fluid Dynamics:** The Finite Volume Method. 2. ed. Essex: Pearson Education Limited, 2007.

WANG, S.; XIAO, J.; WANG, J.; JIAN, G.; WEN, J.; ZHANG, Z.. Configuration optimization of shell-and-tube heat exchangers with helical cover plates using multi-objective genetic algorithm based on fluid-structure interaction. **International Communications In Heat And Mass Transfer**, [S.L.], v. 85, p. 62-69, jul. 2017. Elsevier BV. http://dx.doi.org/10.1016/j.icheatmasstransfer.2017.04.016.

WEN, J.; LI, K.; WANG, C.; ZHANG, X.; WANG, S.. Optimization investigation on configuration parameters of sine wavy fin in plate-fin heat exchanger based on fluid structure interaction analysis. **International Journal Of Heat And Mass Transfer**, [S.L.], v. 131, p. 385-402, mar. 2019. Elsevier BV. http://dx.doi.org/10.1016/j.ijheatmasstransfer.2018.11.023.

APPENDIX A – NUMERICAL METHODS

The aim of utilizing numerical methods for solving problems is to convert the governing differential equations of the observed physical phenomena into computer-readable operations. Linearization tools are utilized in this process, since computers have the capacity to solve complex problems such as irregular geometries, multiphase materials, coupling of different bodies and processes, among others.

A.1 COMPUTATIONAL FLUID DYNAMICS (CFD)

Computational Fluid Dynamics (CFD) comprises of numerical methods for addressing fluid-related issues such as internal and external flow, compressibility, and turbulence. The finite volume method, which linearizes momentum, mass, and energy conservation equations, is the most robust technique. Two equivalent approaches exist for obtaining conservation equations using the finite volume method, as stated by Maliska (2017): Balance of properties in an infinitesimal fluid volume and integration of differential equations in the same volume.

Equations (A.1), (A.2) e (A.3) represent, respectively, the conservations of mass, momentum and energy (BEJAN, 2013 apud MALISKA, 2017, p. 12).

$$\frac{\partial \rho}{\partial t} + \frac{\partial}{\partial x_j}\left(\rho u_j\right) = 0 \tag{A.1}$$

$$\frac{\partial}{\partial t}\left(\rho u_i\right) + \frac{\partial}{\partial x_j}\left(\rho u_j u_i\right) = \frac{\partial P}{\partial x_i} + \frac{\partial}{\partial x_j}\left(\mu \frac{\partial u_i}{\partial x_j}\right) + S^{u_i} \tag{A.2}$$

$$\frac{\partial}{\partial t}\left(\rho T\right) + \frac{\partial}{\partial x_j}\left(\rho u_j T\right) = \frac{\partial}{\partial x_j}\left(\frac{k}{c_P}\frac{\partial T}{\partial x_j}\right) + S^{T} \tag{A.3}$$

In the equations above, the terms presented with indices i and j refer to the Cartesian coordinates x, y, and z using index notation. The variables involved are as follows:

- ρ Fluid density;
- t Time Variable;

- x_i, x_j Space coordinates of the Cartesian system;
- u_i, u_j Velocity vector components $\vec{u} = \left(u_x, u_y, u_z\right) = (u, v, z)$;
- P Surface force (pressure);
- μ Fluid viscosity;
- S^{u_i} Source term for each velocity component;
- T Fluid temperature;
- k Fluid termal condutivity;
- c_P Fluid specific heat (constant pressure);
- S^T Source term related to energy balance.

The simplifying assumptions used in the equations are:

- Incompressible fluid (constant ρ);
- Viscous fluid ($\mu \neq 0$);
- No sources or sinks of linear momentum and energy ($S^{u_i} = S^T = 0$);
- Constant properties (constant c_P, k).

The finite volume method is based on dividing the domain into infinitesimal volumes to balance properties at their boundaries. Mass flow balance in a two-dimensional volume of area $\Delta x \Delta y$ (MALISKA, 2017) is shown in Figure A.1. This flat volume has four boundaries - the west (w), the east (e), the north (n), and the south (s) - representing the mass fluxes in the x and y directions $\rho u_i \Delta x_i|_j$ ($i = x, y$ e $j = w, n, s, e$), respectively. Figure A.2 illustrates the three-dimensional volumes.

Figure A.1 - Illustration of property balance in an infinitesimal volume

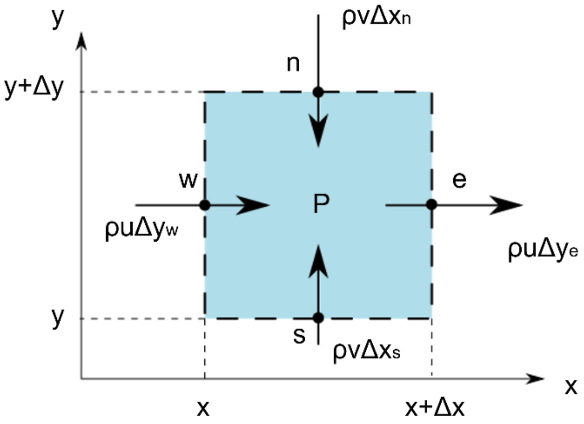

Source: Author (2023).

Once three-dimensional, the infinitesimal volume's borders are defined by a cross-sectional area with a value of $\Delta i \Delta j$, which depends on the evaluated direction and is no longer unitary. Two borders, u and d, representing the Z+ and Z- directions, are added.

The point P, located at the center of the evaluated volume, is the standard representation for the balance of properties. The reference for border directions is always in relation to point P. Volumes are represented in capital letters ($N, S, W, E, U,$ and D), while boundaries are represented in lowercase letters ($n, s, w, e, u,$ and d).

Figure A.2 - Definition of boundaries for three dimensional volumes

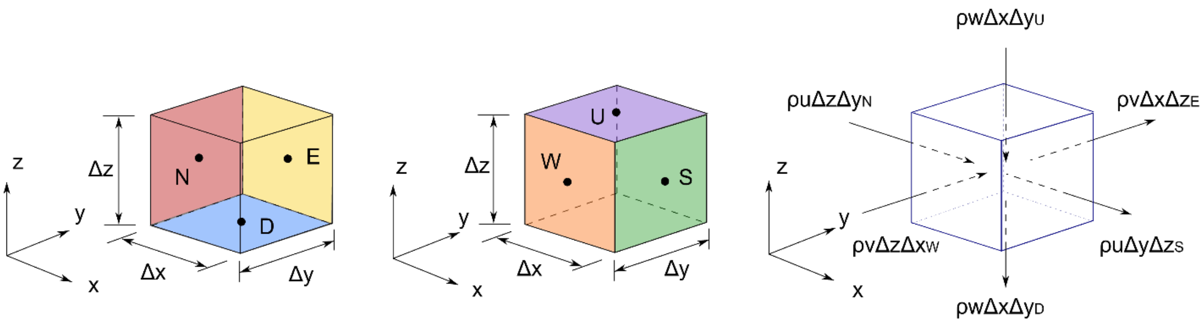

Source: Author (2023).

Figure A.3 illustrates the method in a direct one-way problem. The volume surrounding the point of interest P is bordered by the volumes W and E, and the properties are assessed via the interfaces w and e.

Figure A.3 - Boundary volumes in a uniaxial problem

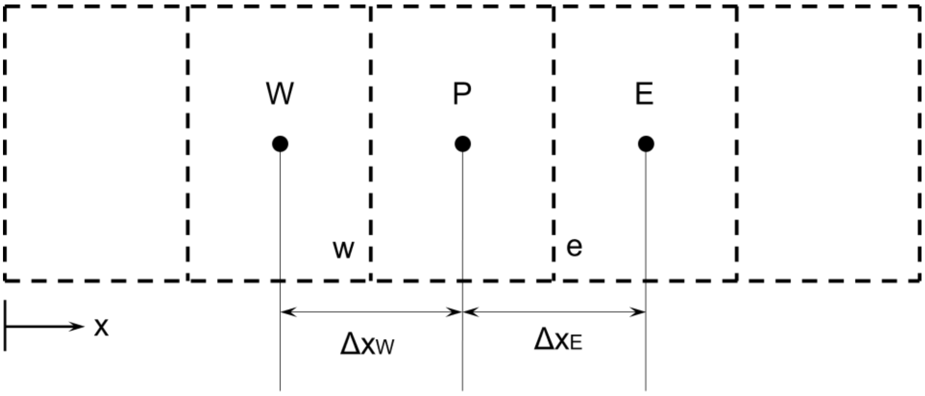

Source: Author (2023).

The conservation equations are linearized using the volume balance and Taylor series, and then solved using methods like Gauss-Seidel and Jacobi. The explicit formulation for the one-dimensional conduction case, based on the domain shown in Figure A.3, is given by Equation (A.4)

$$A_P \phi_P = A_e \phi_E^0 + A_w \phi_W^0 + (A_P^0 - A_e - A_w + S_P \Delta x) \phi_P^0 + S_C \Delta x \tag{A.4}$$

$$A_P = \frac{M_P}{\Delta t}; \qquad A_P^0 = \frac{M_P^0}{\Delta t}$$

$$A_e = \left.\frac{k}{c_P \Delta x}\right|_e; \qquad A_w = \left.\frac{k}{c_P \Delta x}\right|_w$$

$$M_P = \rho_P \Delta x; \qquad M_P^0 = \rho_P^0 \Delta x$$

All subscripts relate the variables to their volumes and interfaces, while superscripts 0 relate to the explicit transient problem. The terms S_P and S_C are source terms, ϕ_i^0 is the property of interest, and A_i are constants derived from the physical properties of the problem. Equations (A.5) and (A.6) demonstrate the central difference interpolation scheme and the conditions for the upwind method, respectively. The latter approach avoids negative term issues but results in smoothing high gradient flow points, making it a suitable method for input advective problems. Constants A_i may cause divergence in linear system solution methods due to their sign.

$$\phi_e = \frac{\phi_E + \phi_P}{2}; \qquad \phi_w = \frac{\phi_W + \phi_P}{2} \tag{A.5}$$

$$\left.\frac{\partial \phi}{\partial x}\right|_e = \frac{\phi_E + \phi_P}{\Delta x_e}; \qquad \left.\frac{\partial \phi}{\partial x}\right|_w = \frac{\phi_P + \phi_W}{\Delta x_w};$$

$$\phi_w = \phi_W; \qquad \phi_e = \phi_P; \qquad u > 0 \tag{A.6}$$

For detailed information and alternative approach methods, it is recommended to check the literature (MALISKA, 2017; VERSTEEG; MALALASEKERA, 2007; PATANKAR, 1980).

A.1.1 Turbulence

Turbulence is the flow regime after the critical Reynolds number, in which the streamlines overlap and the fluid behavior becomes unstable with properties varying in a random and chaotic way (VERSTEEG; MALALASEKERA, 2007).

One method for comprehending the erratic nature of flows is to assess the ϕ property via equation (A.7), wherein $\bar{\phi}$ is the temporal mean of said property, and $\varphi'(t)$ is the fluctuating component of values via the Reynolds decomposition.

$$\phi = \bar{\phi} + \varphi'(t) \tag{A.7}$$

Figure A.4 depicts a turbulent profile exemplifying the time average and fluctuations of property values ϕ. Turbulence can be calculated using various approaches based on factors such as the level of complexity of the physical problem, desired data refinement, and computational power available. The categorization of modeling approaches for turbulent vortex flow is based on the Kolmogorov scales of accuracy (TENNEKES and LUMLEY, 1972; VERSTEEG; MALALASEKERA, 2007). The approaches range from the most detailed - Direct Numerical Simulation (DNS) - to the most generalized - First Order Equations - with Large Eddy Simulation (LES) and Reynolds-Averaged Navier-Stokes (RANS) in between.

Figure A.4 - Representation of a turbulent profile of a property Φ in relation to time

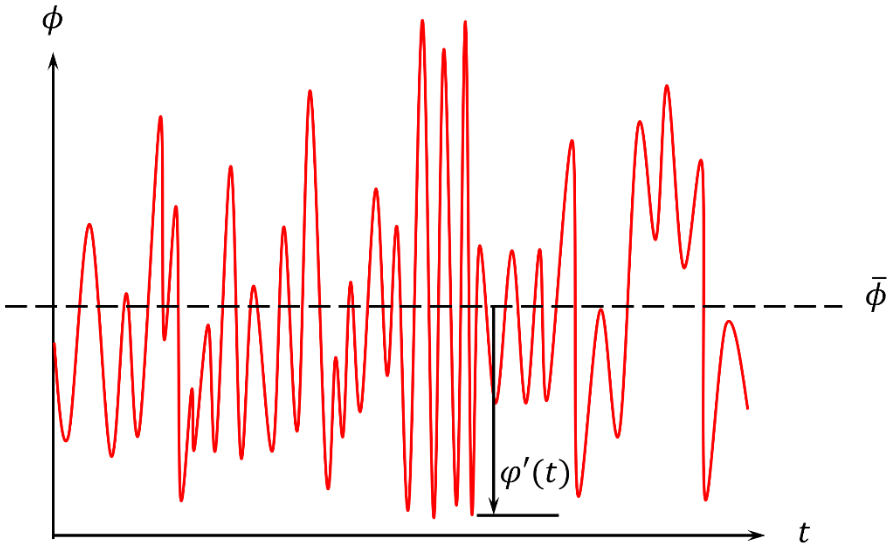

Source: Author (2023).

The $k - \varepsilon$ model is a first-order, two-equation turbulence model primarily utilized for large Reynolds number values. The equation for k (A.8) specifies the transport equation for turbulent kinetic energy, and the equation for ε (A.9) models the rate of dissipation of turbulent kinetic energy (BARDINA; HUANG; CORKLEY, 1997). In the equations provided, S_{ij} represents the mean velocity strain rate tensor, μ_t represents the turbulent viscosity, C_μ is an empirical constant of the model determined through the equilibrium analysis for high Reynolds numbers, and f_μ is the damping function, defined as 1 for the classic $k - \varepsilon$ model.

$$k = \left[2\mu_t\left(S_{ij} - \frac{S_{nn}\delta_{ij}}{3}\right) - \tau_{t_{ij}}\right]\frac{3}{2\rho\delta_{ij}} \tag{A.8}$$

$$\varepsilon = \frac{C_\mu f_\mu \bar{\rho} k^2}{\mu_t} \tag{A.9}$$

One of the key models in fluid dynamics is the wall function, which specifies the mesh refinement for the boundary layer at a fluid-solid interface. As defined by Schlichting and Gersten (2017) in Equation (A.10), the universal wall law is expressed in terms of dimensionless distance from the wall (y^+), friction velocity (u^T), absolute distance from the wall (y), and kinematic viscosity of the fluid (ν). Through this equation, it is possible to interpret y^+ as a local Reynolds number calculated within the boundary layer, which defines the significance relationship between turbulence and flow viscosity.

$$y^+ = \frac{u^T y}{\nu} \tag{A.10}$$

For the $k - \varepsilon$ turbulence model to be applicable, the wall function range of $30 < y^+ < 300$ is required. Beyond $y^+ = 300$, the model fails to resolve the boundary layer accurately, while at $y^+ < 30$, it becomes inapplicable and necessitates a more robust mathematical tool, such as the SST model.

A.2 FINITE ELEMENT METHOD (FEM)

Created in the 1950s by aeronautical engineers to analyze delta-type wings, which were beyond the scope of beam theory, the Finite Element Method (FEM) involves discretizing the analysis domain to calculate the field of a variable, such as stress, displacement, temperature, heat flux, current function, potential velocity function, among others (COOK, 1995).

Such discretization is achieved by dividing the domain into smaller parts, known as "elements", and then describing the behavior of each element. These elements are then reconnected through "nodes", resulting in a system of equilibrium equations. Figure A.5 provides an example of the beam cross-sectional geometry being divided into nodes and elements. The greater number of equations are required when the domain is highly sectioned, which implies that a numerical calculation of the system is necessary for solving complex problems (whether due to geometry, boundary conditions, or loading). However, FEM can be defined as minimizing functions in nodes that constitute a polynomial interpolation within the domain (COOK, 1995).

Figure A.5 - Indication of elements and nodes

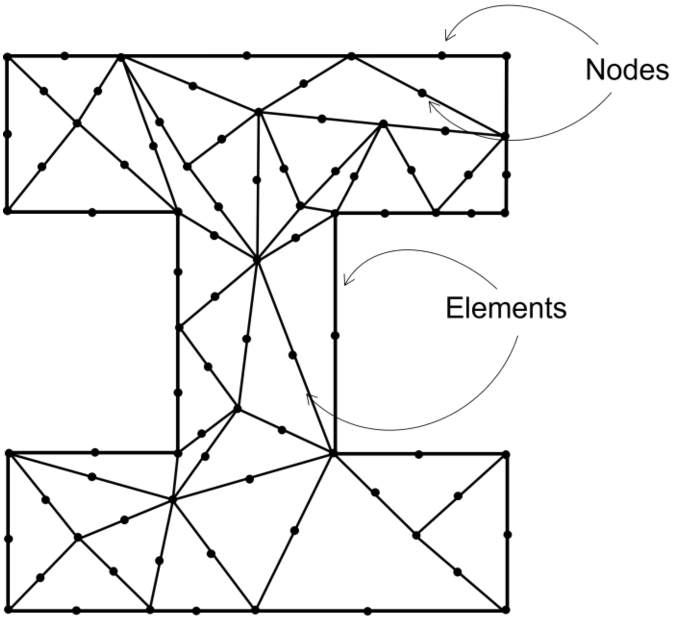

Source: Author (2023).

The FEM classical theory can be algebraically represented in matrix form, as shown in Equation (A.11). Here, $\vec{D}$ represents the unknowns of interest, $\vec{R}$ is the charge vector, and $\underline{\underline{K}}$ is a constant matrix. For the analysis of structural problems, $\underline{\underline{K}}$

represents the stiffness matrix. The equilibrium equations defining these matrices for the investigation of stress or displacement fields follow Generalized Hooke's Law, as shown in Equations (A.12) and (A.13).

$$\underline{\underline{K}}\vec{D} = \vec{R} \qquad \text{(A.11)}$$

$$\varepsilon_i = \frac{\sigma_i}{E} - \frac{\nu}{E}\left(\sigma_j + \sigma_k\right) = \frac{1}{E}\left[\sigma_i - \nu\left(\sigma_j + \sigma_k\right)\right] \qquad \text{(A.12)}$$

$$\gamma_{ij} = \frac{\tau_{ij}}{G}; \gamma_{jk} = \frac{\tau_{jk}}{G}; \gamma_{ik} = \frac{\tau_{ik}}{G} \qquad \text{(A.13)}$$

In the equations above:

- ε_i is the displacement in direction i;
- γ_{ij} is the displacement in the ij plane;
- γ_{jk} is the displacement in the jk plane;
- γ_{ik} is the displacement in the ik plane;
- σ_i is the normal stress to the jk plane;
- σ_j is the normal stress to the ik plane;
- σ_k is the normal stress to the ij plane;
- τ_{ij} is the shear stress in the ij plane;
- τ_{jk} is the shear stress in the jk plane;
- τ_{ik} is the shear stress in the ik plane;
- E is the modulus of elasticity (or Young's modulus) of the material;
- ν is the Poisson coefficient of the material;
- G is the shear modulus of the material.

Despite the strategy of "separating" and then "regrouping" the solution domain, this approach is purely mathematical and not physical. This suggests that, in the context of structural analysis, there are no structural discontinuities that could result in stress concentrations, sliding, or separation of the structural elements. As such, assumptions must be made about the deformation modes of the elements when joined together. In Finite Element Method (FEM), the behavior of elements can vary based on dimensions of the problem, loads, and movement restrictions. Figure A.6 presents a comparison between the different types of elements.

Figure A.6 - Different types of elements inside a primitive geometry

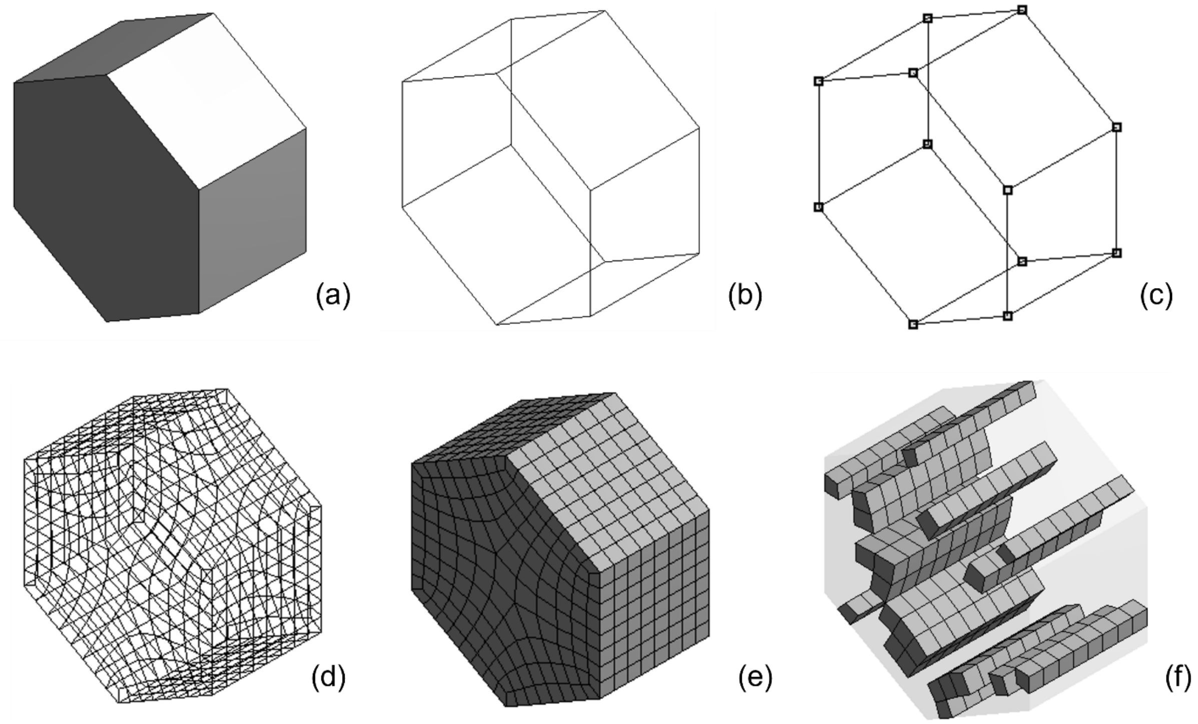

Source: Author (2023).

The prismatic geometry illustrated in Figure A.6-a can be modeled using one-dimensional elements with nodes at their intersections (see Figure A.6-b and Figure A.6-c). However, these results fail to depict the solid's interior behavior, indicating the need for an augmented element count. Figure A.6-d displays a sectioned solid with unidirectional elements of higher density on internal and external surfaces. Figure A.6-e depicts the prism sectioned by planar elements, while Figure A.6-f illustrates the details of internal elements of Figure A.6-e.

The element type choice is associated with boundary conditions as each element type models a specific amount of movement degrees of freedom. Figure A.7 shows a basic bar element with its geometrical structure, modeled degrees of freedom and corresponding stiffness matrix.

Figure A.7 - Bar element

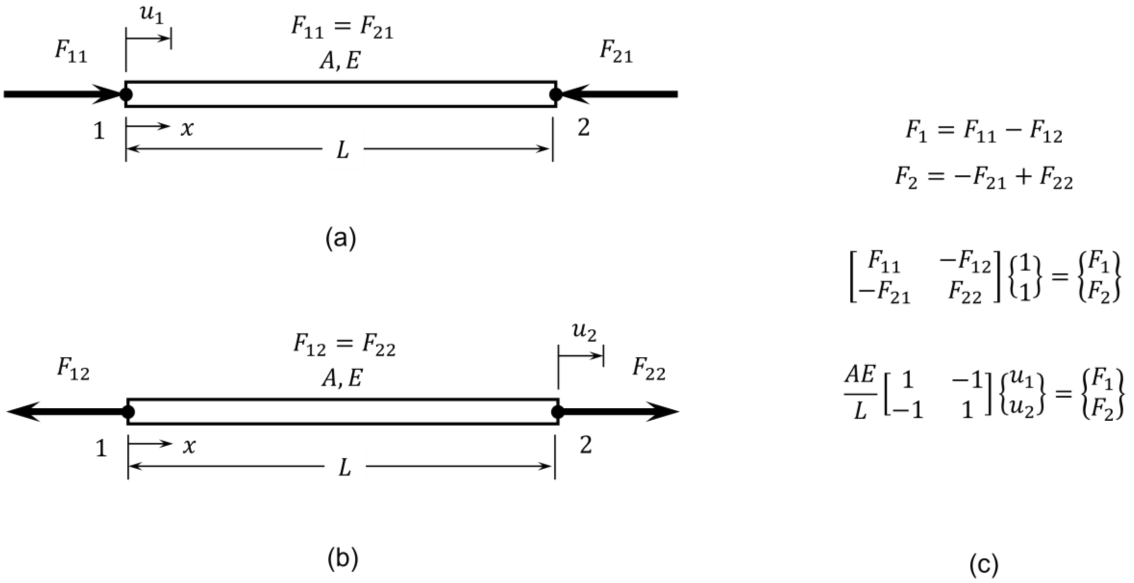

Source: Author (2023). a) a generic bar element under compressive load showing nodal displacement u_1. B) the same bar element under tension presenting nodal displacement u_2. C) the balance of forces that indicates the resulting forces and the equation of the stiffness matrix of the element by the direct method of deduction.

An uniaxial bar element assumes that only axial loads are taken into account, meaning that only tensile and compressive forces are represented by the stiffness matrix. In the given figure, a planar element with cross-sectional area A and Young's modulus E is comprised of two nodes (1 and 2) at either end. At these nodes, compressive (above) and tensile (below) forces corresponding to the displacements u_1 and u_2 are exerted. The element's force is determined by the difference between the forces applied to the nodes, denoted by $F_1 = F_{11} - F_{12}$ and $F_2 = -F_{21} + F_{22}$. The stiffness matrix $\underline{\underline{K}}$ is obtained from the matrix operation based on the fundamental formulation of axial deformation in bars, as depicted in the above figure.

All of the equations shown in Figure A.7 pertain to the direct method of analysis, which is exclusively recommended for problems with simple geometries. For intricate problems, it is advisable to solve the general equation provided in Equation (A.14). This equation consists of the strain-displacement matrix $\underline{\underline{B}}$, the material properties matrix (also known as the constitutive matrix) denoted by $\underline{\underline{E}}$, the stiffness matrix $\underline{\underline{K}}$, and dV, which is a volume increment of V.

$$\underline{\underline{K}} = \int \underline{\underline{B}}^T \underline{\underline{E}}\,\underline{\underline{B}} dV \tag{A.14}$$

Equation (A.14) is defined under the assumption that work is generated by nodal loads applied in order to create nodal displacements and that such work is stored in the element in the form of elastic strain energy.

To find $\underline{\underline{B}}$, it is necessary to define an expression for the axial displacement u at an arbitrary point on the member, as described in Equation (A.15). In it, $\underline{\underline{N}}$ is the shape function matrix and $\vec{d}$ is the vector of the nodal degrees of freedom (DOF) of the element. $\underline{\underline{N}}$ is defined by functions of form N_i that describe how u varies with the coordinate x when one of the DOF is unitary and the other is null, that is, boundary conditions for the Equation (A.15). In this example, $N_1 = \frac{L-x}{L}$ and $N_2 = \frac{x}{L}$.

$$u = \begin{bmatrix} \frac{L-x}{L} & \frac{x}{L} \end{bmatrix} \begin{Bmatrix} u_1 \\ u_2 \end{Bmatrix} = \underline{\underline{N}}\vec{d} \tag{A.15}$$

$$\varepsilon_x = \frac{du}{dx} = \left[\frac{d}{dx}\underline{\underline{N}}\right] \vec{d} = \begin{bmatrix} -\frac{1}{L} & \frac{1}{L} \end{bmatrix} \vec{d} = \underline{\underline{B}}\vec{d} \tag{A.16}$$

In the Equation (A.16), ε_x is the axial deformation, defined by the gradient of the axial displacement. Therefore, $\varepsilon_x = (u_2 - u_1)/L$, $\underline{\underline{E}}$ is the modulus of elasticity of the material in constant form, E, and $dV = Adx$, resulting in Equation (A.17).

$$\underline{\underline{K}} = \int \underline{\underline{B}}^T \underline{\underline{E}}\,\underline{\underline{B}} dV = \int_0^L \begin{Bmatrix} -1/L \\ 1/L \end{Bmatrix} E \begin{bmatrix} -\frac{1}{L} & \frac{1}{L} \end{bmatrix} Adx = \frac{AE}{L} \begin{bmatrix} 1 & -1 \\ -1 & 1 \end{bmatrix} \tag{A.17}$$

This model is limited by load constraints as it only predicts a constant strain state, where linear or high-order strain variations are not accounted for. In such scenarios, it is common to divide the element into smaller portions, gradually adding load as the nodes transition.

The identical process can be utilized for beam elements, where nodes possess two degrees of freedom each - transverse translation and rotation. Figure A.8 displays a planar beam element with respect to its geometric construction, the degrees of freedom it models, and the stiffness matrix that results. Additionally, the equation referenced in Figure A.8 implies the direct deduction method.

Figure A.8 - Beam element

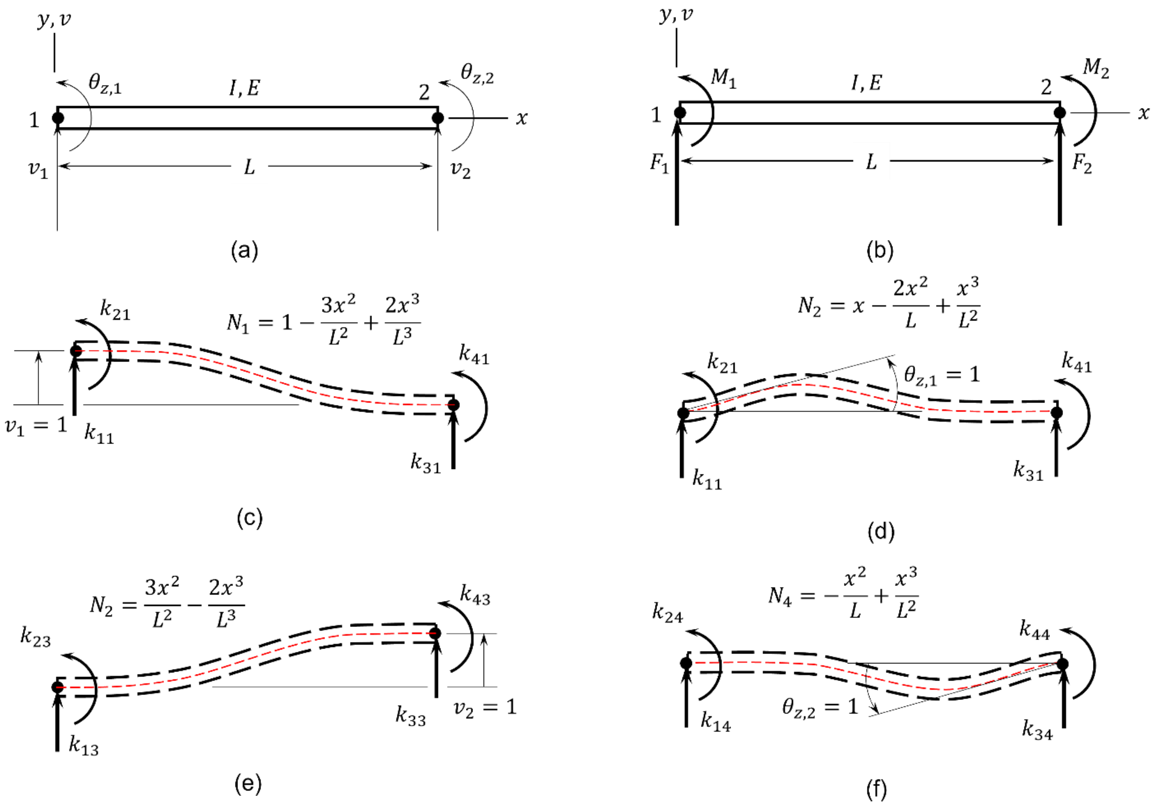

At node 1:

$$v_1 = 1 \qquad 1 = \frac{k_{11}L^3}{3EI} - \frac{k_{21}L^2}{2EI}$$

$$\theta_{z1} = 1 \qquad 0 = -\frac{k_{11}L^2}{2EI} + \frac{k_{21}L}{EI}$$

At node 2:

$$\sum (M_i)\Bigg|_2 = 0 \qquad k_{21} + k_{41} - k_{11}L = 0$$

(g)

At direction Y:

$$\sum (F_i)\Bigg|_y = 0 \qquad k_{11} + k_{31} = 0$$

$$\boldsymbol{k} = \begin{bmatrix} 12\frac{EI}{L^3} & 6\frac{EI}{L^2} & -12\frac{EI}{L^3} & 6\frac{EI}{L^2} \\ 6\frac{EI}{L^2} & 4\frac{EI}{L} & -6\frac{EI}{L^2} & 2\frac{EI}{L} \\ -12\frac{EI}{L^3} & -6\frac{EI}{L^2} & 12\frac{EI}{L^3} & -6\frac{EI}{L^2} \\ 6\frac{EI}{L^2} & 2\frac{EI}{L} & -6\frac{EI}{L^2} & 4\frac{EI}{L} \end{bmatrix}$$

(h)

Source: Author (2023). a) Flat bar element under conditions of translation and rotation of the nodes; B); Forces and moments equivalent to degrees of freedom c) Shape deflected from the centerline and shape function associated with activation of the degree of freedom v_1; d) Shape deflected from the centerline and shape function associated with activation of the degree of freedom θ_{z1}; e) Shape deflected from the centerline and shape function associated with activation of the degree of freedom v_2; f) Shape deflected from the centerline and shape function associated with activation of the degree of freedom θ_{z2}; g) Boundary conditions applied; h) Resultant stiffness matrix.

Unlike bars, where the dependence of axial strain on strain energy is shown, the dependence in beams is relative to the curvature of the element's centerline. Figure A.8 illustrates the curvatures defined by the four degrees of freedom of the indicated element. However, in general, the lateral displacement $v = v(x)$ of a flat beam element is given by the cubic function shown in Equation (A.18) at point x. Equation (A.19) shows $v(x)$ using functions of the form N_i. Equations (A.20) and (A.21) describe the connection between lateral displacement and the strain-displacement matrix and the definition of the strain-displacement matrix for the flat beam element, respectively.

$$v = \beta_1 + \beta_2 x + \beta_3 x^2 + \beta_4 x^3 \tag{A.18}$$

$$v = [N_1 \quad N_2 \quad N_3 \quad N_4]\begin{Bmatrix} v_1 \\ \theta_{z1} \\ v_2 \\ \theta_{z2} \end{Bmatrix} = \underline{\underline{N}}\vec{d} \tag{A.19}$$

$$\frac{d^2v}{dx^2} = \left[\frac{d^2}{dx^2}\underline{\underline{N}}\right]\vec{d} = \underline{\underline{B}}\vec{d} \tag{A.20}$$

$$\underline{\underline{B}} = \left[-\frac{6}{L^2} + \frac{12x}{L^3} \quad -\frac{4}{L} + \frac{6x}{L^2} \quad \frac{6}{L^2} - \frac{12x}{L^3} \quad -\frac{2}{L} + \frac{6x}{L^2}\right] \tag{A.21}$$

Details on limitations and specificities related to the increase in problem dimensions, the application of loads not presented, and the calculation of stress fields for described elements can be found in the literature.

Figure A.9 depicts a planar element undergoing deformation in three scenarios. In Figure A.9-a, the element experiences Δu deformation along the X-axis, whereas in Figure A.9-b, the element undergoes Δv deformation along the Y-axis. In Figure A.9-c, the element undergoes simultaneous deformations, resulting in a change in direction. The diagonal dimensions are relevant to the last two situations. Plane elements experience loads applied in multiple dimensions, resulting in shear deformations.

Figure A.9 - Deformations in plane elements

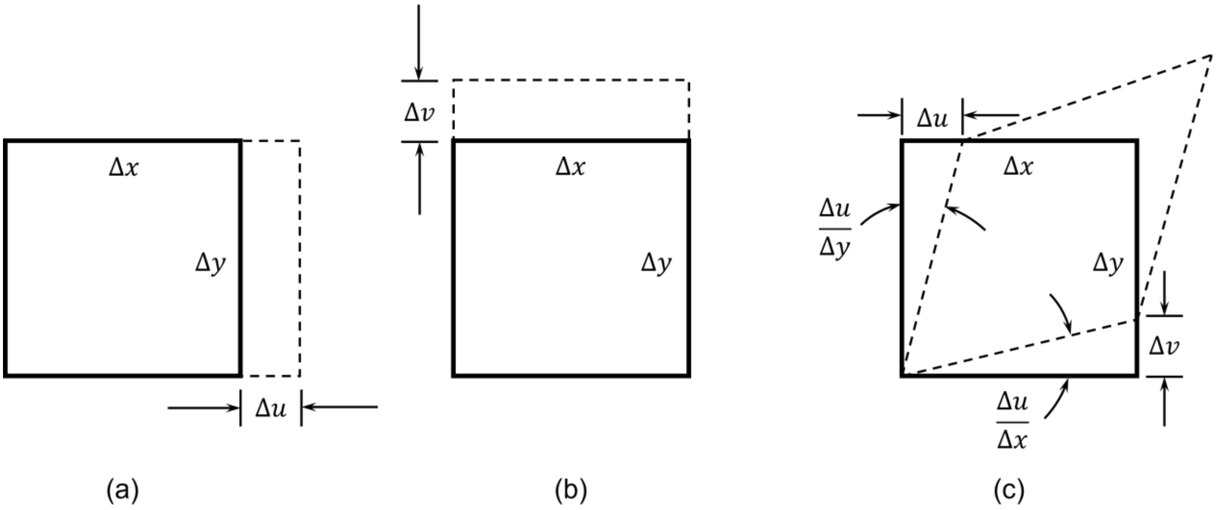

Source: Adapted from Cook (1995).

Equation (A.22) illustrates the stress-strain correlation for a linearly-elastic and isotropic material on a plane. Equation (A.23) presents the aforementioned correlation resolved for the stress vector $\vec{\sigma}$, and its corresponding stiffness matrix. Equation (A.23) and Equation (A.24) are applicable to a stress scenario on the plane, where $\sigma_z = \tau_{yz} = \tau_{zx} = 0$, and the element thickness conforms to the stresses exerted on the XY plane.

$$\begin{Bmatrix} \varepsilon_x \\ \varepsilon_y \\ \gamma_{xy} \end{Bmatrix} = \begin{bmatrix} \frac{1}{E} & -\frac{\nu}{E} & 0 \\ -\frac{\nu}{E} & \frac{1}{E} & 0 \\ 0 & 0 & \frac{1}{G} \end{bmatrix} \begin{Bmatrix} \sigma_x \\ \sigma_y \\ \tau_{xy} \end{Bmatrix} + \begin{Bmatrix} \varepsilon_{x0} \\ \varepsilon_{y0} \\ \gamma_{xy0} \end{Bmatrix} \tag{A.22}$$

$$\vec{\sigma} = \underline{\underline{E}}\vec{\varepsilon} + \overrightarrow{\sigma_0} \tag{A.23}$$

$$\underline{\underline{E}} = \frac{E}{1-\nu^2} \begin{bmatrix} 1 & \nu & 0 \\ \nu & 1 & 0 \\ 0 & 0 & \frac{1-\nu}{2} \end{bmatrix} \tag{A.24}$$

In the case of plane strain conditions, changes in thickness are not allowed, and $\underline{\underline{E}}$ can be obtained using Equation (A.25). Such conditions prohibit alterations in the structure's constitution that may occur during mechanical forming or the application of thermal forces or loads. Therefore, the normal strains are dependent on the Poisson coefficient.

$$\underline{\underline{E}} = \frac{E}{(1+\nu)(1-2\nu)} \begin{bmatrix} (1-\nu) & \nu & 0 \\ \nu & (1-\nu) & 0 \\ 0 & 0 & \left(\frac{1-2\nu}{2}\right) \end{bmatrix} \tag{A.25}$$

In the equations above:

- E is the modulus of elasticity of the material;
- G is the shear modulus of the material;
- ν is the Poisson coefficient;
- ε_i is the normal strain on the i axis;
- ε_{i0} is the initial normal strain on the i axis;
- γ_{ij} is the shear strain in the ij plane;
- γ_{ij0} is the initial shear strain in the ij plane;
- σ_i is the normal stress on the i axis;
- τ_{ij} is the shear stress in the ij plane;
- $\underline{\underline{E}}$ is the matrix of the modulus of elasticity;
- $\vec{\varepsilon}$ is the deformation vector;
- $\overrightarrow{\sigma_0}$ is the initial stress vector, Where $\overrightarrow{\sigma_0} = -E\overrightarrow{\varepsilon_0}$;
- $\overrightarrow{\varepsilon_0}$ is the initial strain vector.

As demonstrated in Figure A.9, plane elements experience multidirectional loads, indicating the correlation between the strain vector and the planes in which the elements are situated. Consequently, the modification of dimensions must feature partial derivatives in its stiffness matrix, as shown in Equation (A.26), which presents the equations (A.27), (A.28), and (A.29) in matrix form.

$$\begin{Bmatrix} \varepsilon_x \\ \varepsilon_y \\ \gamma_{xy} \end{Bmatrix} = \begin{bmatrix} \frac{\partial}{\partial x} & 0 \\ 0 & \frac{\partial}{\partial y} \\ \frac{\partial}{\partial y} & \frac{\partial}{\partial x} \end{bmatrix} \begin{Bmatrix} u \\ v \end{Bmatrix} \tag{A.26}$$

$$\varepsilon_x = \frac{\partial u}{\partial x} \tag{A.27}$$

$$\varepsilon_y = \frac{\partial v}{\partial y} \tag{A.28}$$

$$\gamma_{xy} = \frac{\partial v}{\partial x} + \frac{\partial u}{\partial y} \tag{A.29}$$

Figure A.10, Figure A.11, Figure A.12 and Figure A.13 illustrate four of the main types of plane elements used in FEM. They contain the representation of the element in terms of the position of the nodes and the displacement vectors, the representation of at least one deformation mode of that element and the equations that define the displacements and deformations of the element.

Figure A.10 - Constant Strain Triangle (CST)

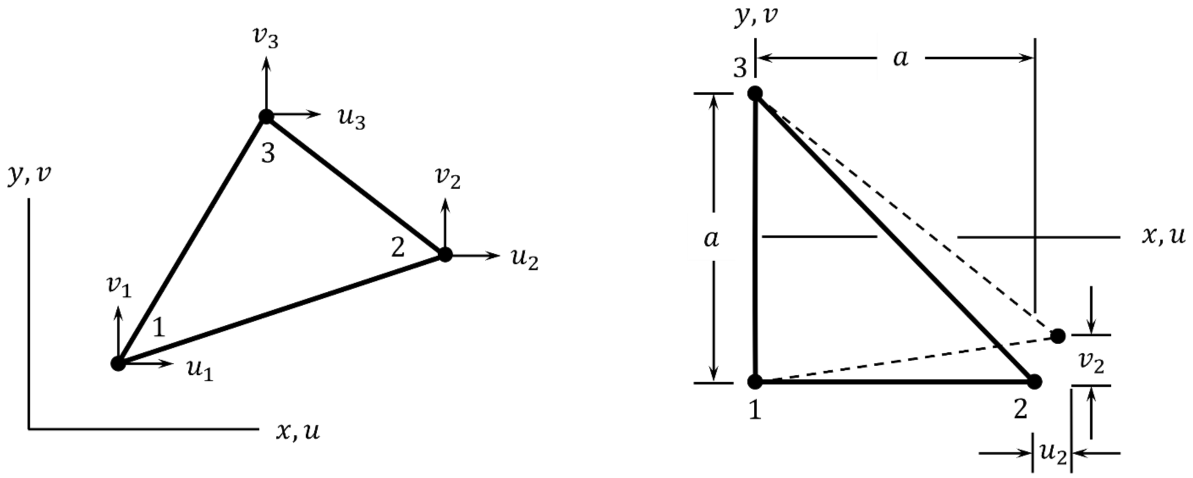

$$u = \beta_1 + \beta_2 x + \beta_3 y$$

$$v = \beta_4 + \beta_5 x + \beta_6 y$$

$$\varepsilon_x = \beta_2 \qquad \varepsilon_y = \beta_6 \qquad \gamma_{xy} = \beta_3 + \beta_5$$

Source: Adapted from Cook (1995).

The Constant Strain Triangle (CST) (Figure A.10) is a triangular element with nodes placed at its vertices. Each node displays deformation in both axes. Its name is derived from the order of the expressions defining the ε_j and γ_{ij} deformations. The Linear Strain Triangle (LST) (Figure A.11), in contrast, has quadratic displacements with linear deformations in element nodes that exist not only at the vertices but also in the middle of the element and edges. Technical abbreviations such as LST must be clearly defined when first used. Such an increase in the order of expressions suggests that the displacement profiles of the entire structure have become better adapted. However, solving the system of equations becomes more costly as the number of coefficients has doubled from 6 to 12.

Figure A.11 - Linear Strain Triangle (LST)

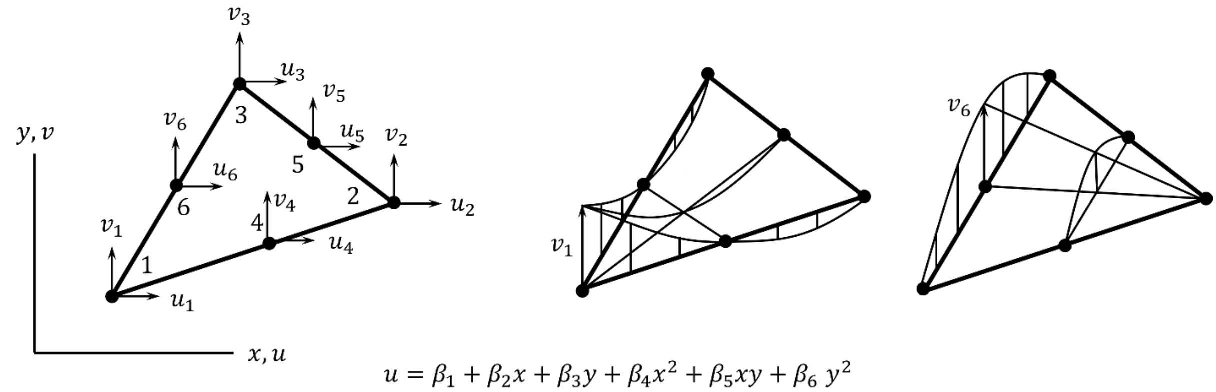

$$u = \beta_1 + \beta_2 x + \beta_3 y + \beta_4 x^2 + \beta_5 xy + \beta_6\ y^2$$

$$v = \beta_7 + \beta_8 x + \beta_9 y + \beta_{10} x^2 + \beta_{11} xy + \beta_{12}\ y^2$$

$$\varepsilon_x = \beta_2 + 2\beta_4 x + \beta_5 y$$

$$\varepsilon_y = \beta_9 + \beta_{11} x + 2\beta_{12} y$$

$$\gamma_{xy} = (\beta_3 + \beta_8) + (\beta_5 + 2\beta_{10})x + (2\beta_6 + \beta_{11})y$$

Source: Adapted from Cook (1995).

In the same way as the CST, the Bilinear Quadrilateral element (Q4) (Figure A.12) only has nodes located at its vertices, but in a now rectangular element. While linear deformations do not reduce the order of deformations due to $\beta_n ij$ terms, the vertex nodes are incapable of modeling the torsion of element edges, a behavior supported by Quadratic Quadrilateral elements (Q8) (Figure A.13).

Figure A.12 - Bilinear Quadrilateral (Q4)

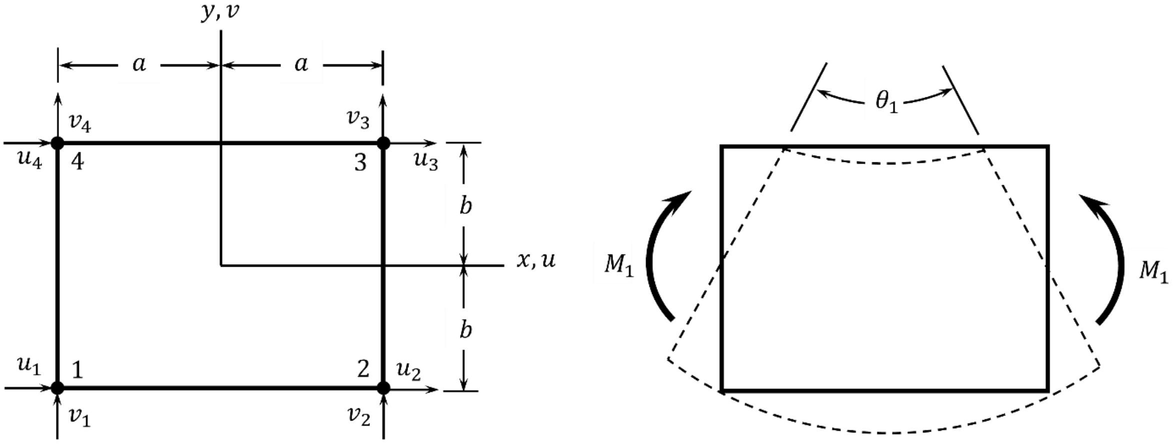

Correct deformation mode of a rectangular block in pure bending

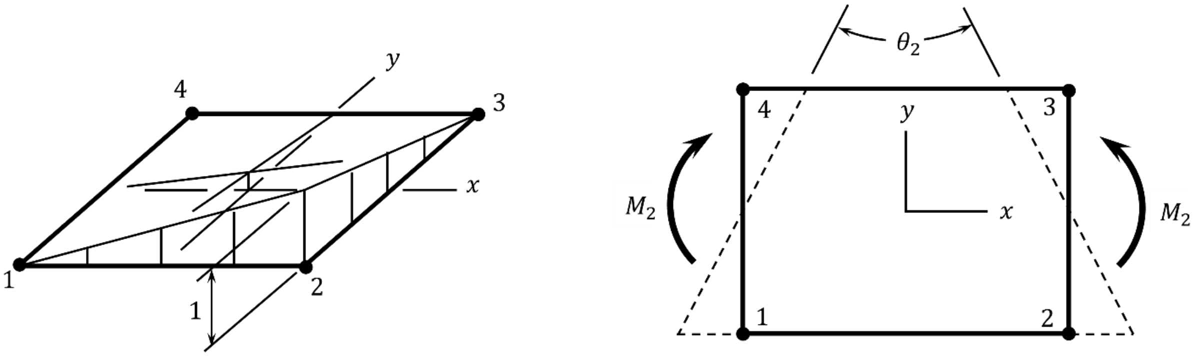

Shape function N_2 of the bilinear quadrilateral

Deformation mode of the bilinear quadrilateral under bending load

$$u = \beta_1 + \beta_2 x + \beta_3 y + \beta_4 xy$$

$$v = \beta_5 + \beta_6 x + \beta_7 y + \beta_8 xy$$

$$\varepsilon_x = \beta_2 + \beta_4 y$$

$$\varepsilon_y = \beta_7 + \beta_8 x$$

$$\gamma_{xy} = (\beta_3 + \beta_6) + \beta_4 x + \beta_8 y$$

Source: Adapted from Cook (1995).

Figure A.13 - Quadratic Quadrilateral (Q8)

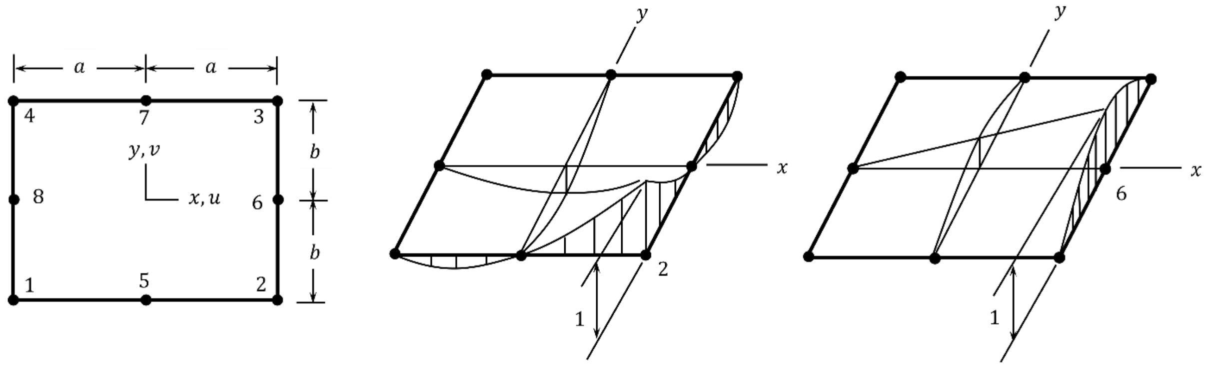

$$u = \beta_1 + \beta_2 x + \beta_3 y + \beta_4 x^2 + \beta_5 xy + \beta_6\, y^2 + \beta_7\, yx^2 + \beta_8\, xy^2$$

$$v = \beta_9 + \beta_{10} x + \beta_{11} y + \beta_{12} x^2 + \beta_{13} xy + \beta_{14}\, y^2 + \beta_{15}\, yx^2 + \beta_{16}\, xy^2$$

$$\varepsilon_x = \beta_2 + 2\beta_4 x + \beta_5 y + 2\beta_7 xy + \beta_8\, y^2$$

$$\varepsilon_y = \beta_{11} + \beta_{13} x + 2\beta_{14} y + \beta_{15}\, x^2 + 2\beta_{16} xy$$

$$\gamma_{xy} = (\beta_3 + \beta_{10}) + (\beta_5 + 2\beta_{12})x + (2\beta_6 + \beta_{13})y + 2(\beta_8 + \beta_{15})xy + \beta_7\, x^2 + \beta_{16}\, y^2$$

Source: Adapted from Cook (1995).

Nuances regarding the application of such elements and the definition of other specific element types can be located in the literature. In this study, the primary elements in the solution meshes are of the LST variety: their triangular shape is more appropriate for adjusting circular geometries or those with pronounced curvature. Furthermore, it is feasible to mitigate the computational cost incurred due to the number of equations required to define the deformation state of the element by balancing the element count in the mesh with the necessity to refine the modeling. In other words, it is plausible to designate particular zones to utilize sturdier elements for capturing the crucial behaviors of the structure.

APPENDIX B – MESH INDEPENDENCE ANALYSIS

The mesh independence analysis was performed for each geometry used in this study under a condition of $\dot{m}_{IN} = 2kg/s$. Table B.1 displays the differentiation of all analyzed geometries.

Table B.1 - Definition of evaluated geometries in relation to mesh independence

Geometry	Domain Type	$\boldsymbol{\beta}$	$\mathbf{2b}$	$\boldsymbol{\Delta\delta}$
Extern	Fluid	60º	5.3 mm	0 mm
Intern	Fluid	60º	5.3 mm	0 mm
Intern	Fluid	60º	5.8 mm	0.5 mm
Intern	Fluid	60º	6.3 mm	1.0 mm
Intern	Fluid	60º	6.8 mm	1.5 mm
Plates	Solid	60º	5.3 mm	0 mm

Source: Author (2023).

The meshes created for analysis were generated using Ansys Meshing software, varying the following mesh characteristics:

- Size Function: Curvature. Examines the curvature on edges and faces and computes element sizes on these entities such that the size does not violate the maximum size or the curvature normal angle;
- Relevance Center: Control the fineness of the mesh for the entire model;
- Maximum Face Size: is the maximum size that the size function will return;
- Transition: Affects the rate at which adjacent elements will grow. Slow produces smooth transitions while Fast produces more abrupt transitions.
- Span Angle Center: Sets the goal for curvature-based refinement;
- Face Sizing: Define sizing that is to be applied at a specified Location.

Since the geometry presents complex surfaces with varying curvatures and areas, the hexahedral method was discarded as an option for mesh generation. All the meshes presented are tetrahedral, including the region of the fluid inlet and outlet pipes, because although these are well behaved geometry sections, it was preferred to avoid method transitions that would culminate in a loss of mesh quality in the transition zones between evaluation regions. Table B.2 summarizes the technical details of the seven meshes chosen for the analysis of the geometries.

Table B.2 - Definitions of analyzed meshes – Fluid Domain

	M1	**M2**	**M3**	**M4**	**M5**	**M6**	**M7**
Size Function	Curvature	Curvature	Curvature	Curvature	Curvature	Curvature	Curvature
Relevance Center	Coarse	Fine	Medium	Coarse	Medium	Medium	Coarse
Max Face Size	2mm	2mm	1mm	1mm	2mm	5mm	2mm
Transition	Slow	Fast	Slow	Slow	Slow	Slow	Slow
Span Angle Center	Fine	Fine	Medium	Coarse	Medium	Medium	Coarse
Face Sizing (In/Out)	None	10mm	10mm	10mm	10mm	10mm	10mm

Source: Author (2023).

Mesh quality is monitored by the Aspect Ratio (AR) metric, which defines the ratio between the major dimensions of the selected mesh element. For elements with a triangular base, such as tetrahedrons, the aspect ratio is calculated as shown in Figure B.1. A line is drawn between one of the vertices of the triangle (K) and extends to the center of the opposite edge ($\overline{IJ}$), while another line is drawn between the two midpoints of the other two edges ($\overline{KJ}$) and ($\overline{KI}$). Typically, such lines are not perpendicular because of some angular distortion in mesh elements.

Figure B.1 - Triangle aspect ratio calculation

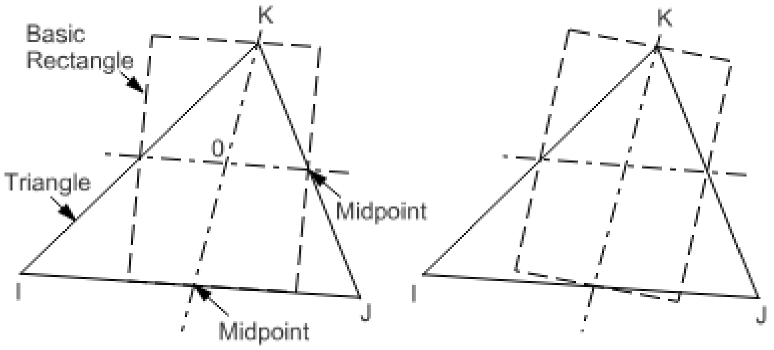

Source: ANSYS (2023).

Next, rectangles are constructed from these guidelines so that their edges contain the midpoints of the edges of the triangular element ($\overline{IJ}/2$, $\overline{KJ}/2$ and $\overline{KI}/2$) and one of its vertices (K, J, and I), oriented by the first straight line drawn for each orientation. Its angular distortion is then defined by the angle of the centerline relative to the vertical. The aspect ratio of the triangle is defined as $AR_{\Delta} = (L_{MS}/l_{MS})^{-1/3}$, where L_{MS} is the length of the longest side of the most distorted rectangle and l_MS is the length of the smallest side of the same rectangle.

Figure B.2 shows the difference between the meshes graphically, displaying details of the geometry to highlight zones of greater importance for studying the quality of the meshes. By cross-referencing the information in Figure B.2 and Table B.2, it can be seen that the factor with the greatest influence on the behavior of the meshes is the transition. In Figure B.2-b, referring to the M2 mesh, there is a sharp difference in refinement between the regions of the entrance port, the distribution gallery and the beginning of the exchange channel, revealing a sectioned behavior. Such a sudden transition is the result of the transition factor being set to Fast, indicating a reduction in the resolution of the function defined for the transition. Mesh M3, immediately below, shows a smooth transition between the analysis regions. It is well known that the more abrupt the transition, the lower the resolution of the data in these regions, resulting in greater error propagation.

The size chosen for the elements also affects their transition, as can be seen in Figure B.2-e. Mesh M5 presents an abrupt transition between the distribution gallery and the beginning of the exchange channel, even though the Transition parameter is set to Slow, due to the maximum size of the elements (2mm). When the mesh reaches the transition zone between the two regions, the generator is forced to reduce the size of the elements according to the reduced size of the surfaces present there. For this reason, the elements of the two regions have considerable differences in size, as can be seen in the figure.

Less refined meshes exhibit poorer adaptation to corrugated geometry, as depicted in Figure B.2-e and Figure B.2-f, portraying meshes M6 and M7, respectively. The Distribution Gallery region's diamond-shaped corrugation has larger zones of low refinement, resulting in the nonuniformity of the solution mesh. Previous structural analyses cited in the literature (MARTINS et al.; 2022) have shown that the Distribution Gallery is a critical area for stress data, specifically in the diagonal region not supported by the gasket. Therefore, refining this area is essential for the current study's related analyses.

Figure B.2 - Details of the meshes generated for independence analysis

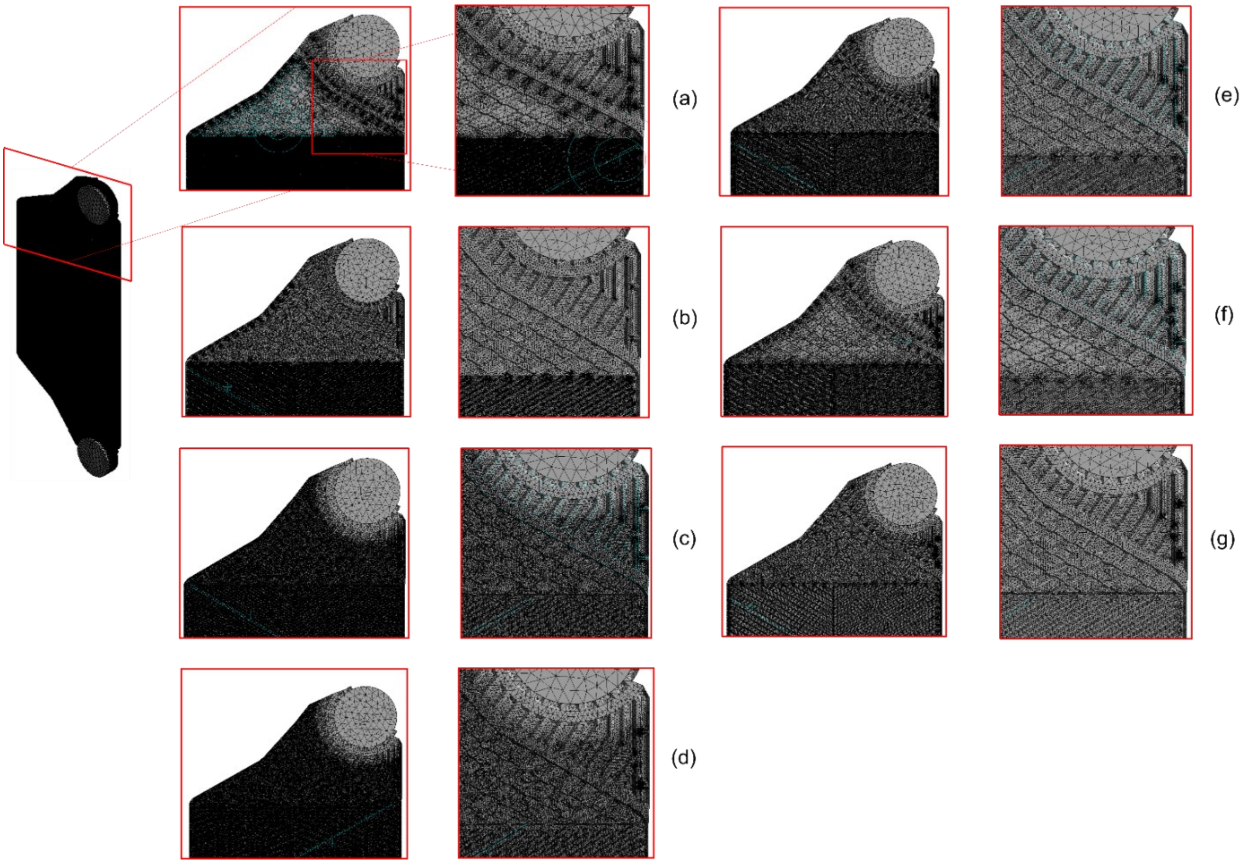

Source: Author (2023). a) M1 mesh; b) M2 mesh; c) M3 mesh; d) M4 mesh; e) M5 mesh; f) M6 mesh; g) M7 mesh.

B.1 FLUID DOMAIN

Table B.3 indicates the results for the meshes defined in Table B.2, monitoring the values of ΔP, y^+ and $\overline{Re}$. For details on the y^+ variable, see Appendix A. Due to the high computational cost, the M1 mesh was analyzed only in the initial geometry.

It can be observed that all of the selected meshes fall within the acceptable y^+ range for the $k-\varepsilon$ model, which is $30 \leq y^+ \leq 300$. As a result, the turbulence model choice is acceptable in all instances. The aspect ratio values (AR_{Δ}), which are the geometric quality metric considered for monitoring, fall within the acceptable range of $1.8 < AR_{\Delta} < 2.2$ for the analyses developed in this study.

Figure B.3 illustrates the relationship between the monitoring variables and the number of elements. The results reveal a decrease of around 13% in ΔP values from M7 to M1 (with an increase of 1.70x10^7 elements) for the internal branch geometry with a separation of 0mm. Therefore, it is evident that intermediate meshes, like the M3 and M4 meshes, can be utilized for analysis without affecting the outcomes. For the external branch geometry, as well as the internal branches with separations of 0.5mm, 1.0mm, and 1.5mm, the drop (from M7 to M2) reaches 12.4%, 3.4%, 6.1%, and 7.7%, respectively.

The $\overline{Re}$ values corroborate the choice of intermediate meshes, since, for the most extreme case – internal branch geometry with 0mm of separation – the deviation between meshes M1 and M7 reaches 101% in this variable.

Although no trend curve reaches an optimal value, indicating that there is still room for mesh refinement in the indicated domain, meshes from M2 became very time consuming (24h for mesh M2 and 48h for mesh M1) in order to reduce the error of the results, making their use infeasible. The use of the M1 mesh in the FSI method was also not possible as it exceeded the available memory in the machine, since this method incorporates both meshes (FEM and CFD) for interface matching. For these reasons, the M3 mesh was selected for the CFD analysis of the fluid domain geometries.

Table B.3 - Mesh independence analysis results for fluid domain geometries

	M1	**M2**	**M3**	**M4**	**M5**	**M6**	**M7**
Extern							
P_{IN} [Pa]	-	80506.5	76804.8	76645.1	88232.3	88628.9	70536.7
ΔP [bar]	-	0.807	0.770	0.768	0.884	0.888	0.707
Re_{med}	-	9.14E+03	8.67E+03	8.63E+03	8.60E+03	8.54E+03	7.94E+03
y^{+}_{med}		30.6105	44.5188	44.7349	52.3045	51.8371	61.5007
N Elem.	-	1.28E+07	9.69E+06	9.48E+06	4.23E+06	4.05E+06	1.92E+06
AR_{Δ}	-	2.0741	1.9320	1.9342	2.0450	2.0549	2.1863
Intern (δ_Z = 0mm)							
P_{IN} [Pa]	2.44E+05	3.15E+05	2.98E+05	2.97E+05	3.41E+05	3.41E+05	2.75E+05
ΔP [bar]	2.44	3.15	2.98	2.97	3.41	3.42	2.76
Re_{med}	1.09E+04	1.76E+04	2.43E+04	2.45E+04	2.47E+04	2.51E+04	2.20E+04
y^{+}_{med}	76.5	88.0	82.3	83.1	105.0	104.0	114.0
N Elem.	1.80E+07	6.57E+06	4.96E+06	4.86E+06	2.20E+06	2.07E+06	9.60E+05
AR_{Δ}	1.8771	2.0657	1.9300	1.9322	2.0293	2.0440	2.1757
Intern (δ_Z = 0.5mm)							
P_{IN} [Pa]	-	146715.00	138198.00	138111.00	157381.00	1.59E+05	141214.00
ΔP [bar]	-	1.47	1.39	1.39	1.58	1.60	1.42
Re_{med}	-	16317.14	15908.39	15855.65	15587.37	15515.61	14783.57
y^{+}_{med}	-	47.51	67.47	67.97	83.24	82.12	101.47
N Elem.	-	6.63E+06	5.39E+06	5.27E+06	2.40E+06	2.31E+06	1.05E+06
AR_{Δ}	-	2.0633	1.9028	1.8998	1.9798	1.9803	2.0976
Intern (δ_Z = 1.0mm)							
P_{IN} [Pa]	-	98380.8	87200.40	87224.70	87202.10	9.85E+04	92744.50
ΔP [bar]	-	0.99	0.87	0.87	0.87	0.99	0.93
Re_{med}	-	14596.05	14653.47	14619.40	14653.47	14490.45	14047.73
y^{+}_{med}	-	39.84	56.32	56.70	72.30	71.47	89.41
N Elem.	-	6.81E+06	6.30E+06	6.17E+06	2.76E+06	2.63E+06	1.24E+06
AR_{Δ}	-	2.0205	1.8664	1.8670	1.9033	1.9116	1.9552
Intern (δ_Z = 1.5mm)							
P_{IN} [Pa]	-	64989.70	54336.90	54442.50	61935.70	6.12E+04	59972.10
ΔP [bar]	-	0.65	0.55	0.55	0.62	0.62	0.60
Re_{med}	-	13242.07	13452.06	13427.09	13373.03	13295.52	13136.08
y^{+}_{med}	-	33.83	47.53	47.83	63.32	62.81	80.31
N Elem.	-	7.35E+06	6.93E+06	6.79E+06	2.99E+06	2.85E+06	1.36E+06
AR_{Δ}	-	2.0566	1.8803	1.8847	1.9380	1.9389	2.0181

Source: Author (2023).

Figure B.3 - Mesh independence plots for fluid domain geometries

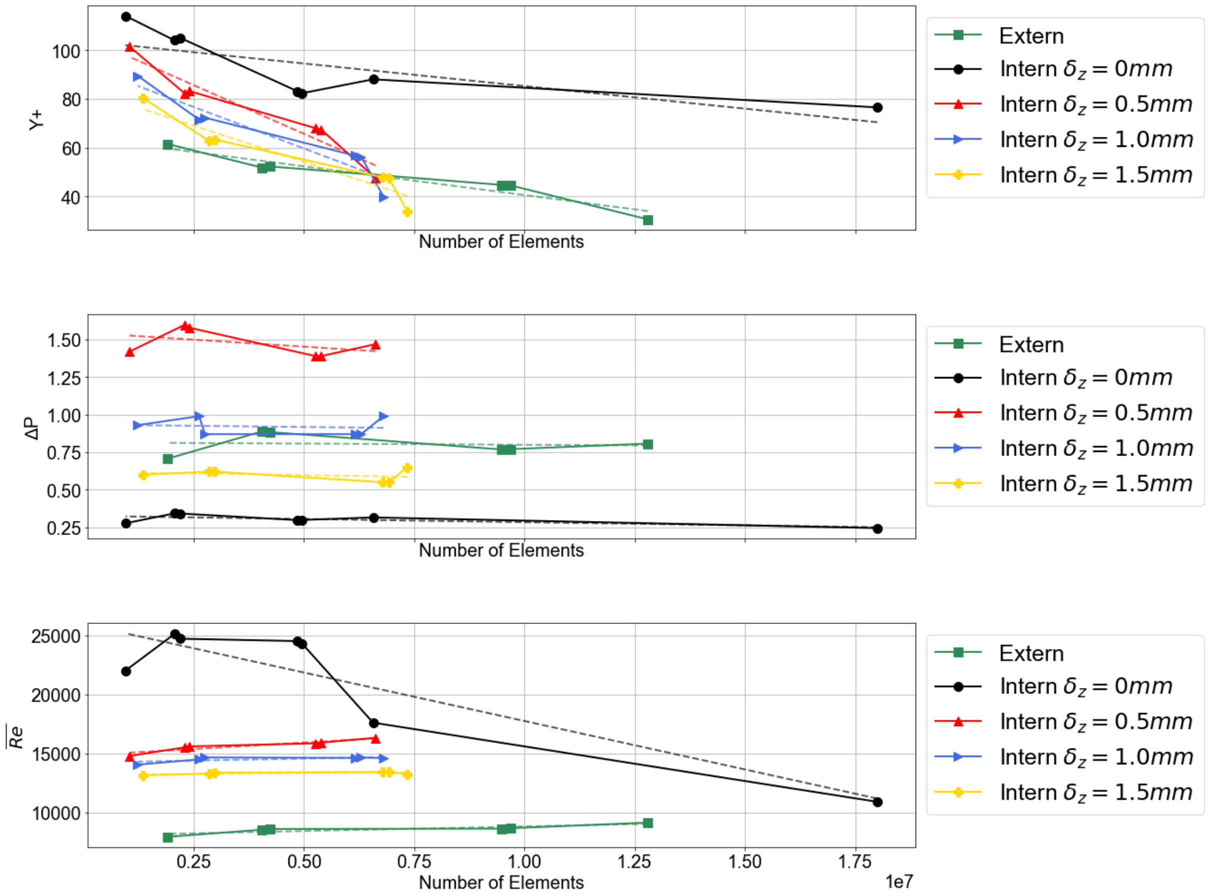

Source: Author (2023). The dashed lines represent the linear trend of each curve.

B.2 SOLID DOMAIN

Taking into account the discussion about mesh behavior due to available construction parameters, two meshes were proposed for the solid domain: MS1 and MS2, shown in Table B.4. No local mesh refinement was defined for the solid domains. Also in this table it is possible to find an extra parameter, called Body Type, which indicates whether the geometry was defined as solid or surface in the analysis. The surface hypothesis is reasonable due to the low thickness of the plates, which can be added to the analysis in the form of a virtual thickness, that is, it is not considered in the geometry, but its value is added in the solution of the governing equations. This alternative is used to reduce the size of the solution mesh, since the mesh not only refines the domain on the surface, but also along the normal axis, which characterizes the thickness direction, increasing, in this work, up to 4 times the amount of elements when the surface is considered a solid. Also, elements are changed from three-dimensional elements to flat elements when applying the Surface Body Type.

Table B.4 - Definitions of the analyzed meshes: Solid Domain

	MS1	**MS2**	**MS3**
Size Function	Adaptive	Adaptive	Adaptive
Relevance Center	Medium	Medium	Medium
Element Size	10mm	5mm	1mm
Transition	Slow	Slow	Slow
Span Angle Center	Medium	Medium	Medium
Body Type	Solid	Solid	Surface

Source: Author (2023).

The loading condition used for mesh analysis was 2bar-2bar. Table B.5 shows the main results for the previously indicated meshes. Based on these results, hydrostatic analyses were performed using the MS2 mesh. Due to the high computational cost required for the solution of the FSI analysis, the MS3 mesh was chosen for this application, as it is smaller and presents performance with acceptable deviations.

Table B.5 - Main results for solid domain geometries in seven different mesh configurations.

	MS1	**MS2**	**MS3**
σ_{MAX} [MPa]	413.62	410.25	450.23
$\delta_{Z,MAX}$ [mm]	0.50524	0.51298	0.72463
N Elem.	1673397	1963892	1599020
AR_{Δ}	4.5818	3.8762	1.159

Source: Author (2023).